Title
Multiscale Defect Formation and Transport in Materials in Extreme Environments

Permalink
https://escholarship.org/uc/item/7nd7n47c

Author
Seif, Dariush

Publication Date
2013

Peer reviewed|Thesis/dissertation

University of California

Los Angeles

Multiscale Defect Formation and Transport in Materials in Extreme Environments

A dissertation submitted in partial satisfaction

of the requirements for the degree

Doctor of Philosophy in Mechanical Engineering

by

Dariush Seif

2013

ABSTRACT OF THE DISSERTATION

Multiscale Defect Formation and Transport in Materials in Extreme Environments

by

Dariush Seif

Doctor of Philosophy in Mechanical Engineering

University of California, Los Angeles, 2013

Professor Nasr M. Ghoniem, Chair

The lifetime and properties of materials operating under extreme conditions are determined by complex interactions stemming from the formation of internal defects at the atomic length and time scales. The research conducted in this dissertation is focused on the study of atomic defect formation and transport under such conditions, and the development of atomically-based tools with enhanced resolution and predictive capabilities. Our attention is placed on two such far-from-equilibrium conditions with important real world implications: materials irradiated in nuclear environments and materials deforming under shock loading.

In the former, prolonged exposure to irradiation by energetic neutrons or ions, resulting in atomic collision cascades, leads to the formation, transport and aggregation of vacancies and self-interstitial atoms (SIAs) into clusters. This leads to an evolution of the microstructure and thus also the material properties, making the problem truly multiscale in both time and space. In addition, energy barriers for the thermally activated processes that govern this evolution are inhomogeneous, varying spatially due to non-uniform internal stress and temperature fields. Because of these complexities, and the many scales involved, typical efforts to model such phenomena face severe coarse-graining, often neglecting spatial heterogeneities altogether and using mean-field approaches.

In this dissertation, we develop computational models of point defect formation and transport in spatially heterogeneous stress and temperature fields. To accomplish this, first an atomistically-based description of point defects is developed using a combination of molecular statics calculations and continuum elasticity theory. This enables an accurate representation of point defect strain fields and their interaction energies in various strain fields. The continuum representation has been found to be accurate to within several percent of the atomistic calculations and was successfully tested against highly accurate first principles calculations in a published study.

Using the described point defect representation, we have performed calculations of the dislocation bias factor for irradiated metals, using a spatially-resolved rate theory solution we developed based on the finite element method. The flexibility of the model is fully exploited, leading to calculations with heightened resolution; accounting for the spatially-dependent, energetically favorable SIA orientations, one-dimensional diffusion mechanisms near the dislocation core, and full anisotropic elasticity. Our results for iron have shown that the effects of preferred SIA orientations should not be ignored near the dislocation core. Implementing minimum energy SIA configurations in iron decreases repulsive interactions and increases absorption, ultimately leading to much larger bias factors. On the other hand, we also find the use of anisotropic elasticity in the calculations to decrease bias factors by 45% compared to those obtained using the isotropic formulation. An anisotropic implementation of the dislocation strain fields, however, gives larger interaction energy gradients, leading to increased drift diffusion and larger bias (12% and 6% increase in Fe and Cu, respectively). One-dimensional migration also plays a significant role in decreasing the bias, but its effect is greatly diminished when anisotropy and SIA orientations are accounted for.

Following the rapid transient stage of helium-vacancy cluster (bubble) nucleation under irradiation, the bubble growth phase proceeds over macroscopic timescales. Due to the complex nature of the problem, prediction of the time-dependent bubble size distribution in the helium-vacancy phase space has remained elusive. In this dissertation we approach the problem in two ways, both accounting for full material spatial resolution. In the first, we use a previously developed reduced set of rate equations to track the average bubble size through time, in a two-dimensional specimen under the typical stress and temperature gradients seen in plasma-facing components in fusion environments. With temperature gradients long known to have several orders of magnitude greater effect on bubble diffusion than associated stress gradients, our results conclusively revealed the important role of stress gradients on the near-surface average bubble size profile due to point defect diffusion processes.

Extending this spatially-dependent rate theory approach to capture the full bubble size distribution surface, we have developed a novel approach based on the theory of nonlinear stochastic differential equations. Here, we provide a framework to describe the full helium bubble size distribution as a function of time and space, in irradiated metals under stress and temperature gradients. Our findings show the important role of stochastic atomic fluctuations on the dispersion of the distribution around the mean. We find for smaller average bubbles sizes (early in the simulation), the spread of the distribution is large and stable. As bubbles begin to grow larger, the stochastic fluctuations have a reduced effect and the distribution begins to shrink, corresponding to a more uniformly sized bubble population. Recommendations are also made regarding how to advance the simulations in the future by including phenomena such as bubble coalescence.

To characterize the response of metals to shock loading, extensive molecular dynamics (MD) simulations have been performed. In light of recent experimental results obtained by laser-induced shock-loading on single-crystal nanopillars, MD simulations were performed on both nanofilm and nanopillar structures, the difference being the geometry and imposed boundary conditions in the directions transverse to the propagation direction of the shock wave. The dynamic response of the structures to shock loading was analyzed over a wide spectrum of impact stresses. State variables (stress, velocity, temperature, etc.) were computed as functions of time and position along the specimen. The deformation mechanisms observed in nanopillars was found to differ significantly from those found in the nanofilms and bulk samples. Specifically, in nanofilms, we found the presence of periodic boundary conditions require much larger impact stresses to induce plasticity ($>$ 35 GPa) compared to nanopillars, where free surfaces play an important role. In nanopillars, comparison to the experiments explained the observed surface activation at lower than expected stresses ($\sim$ 1 GPa), due to dislocation nucleation and termination at the free surfaces. Additional simulations of spallation were also performed. Results showed the formation of voids occurrs at the intersections of stacking faults at the spall plane. The growth and coalescence of these voids leads to the full spallation of the material. In these cases the [100] oriented crystals showed increased resilience to spallation compared to the [111] crystals. The results of this work have contributed to a greater understanding of the deformation mechanisms at work in metal nanostructures exposed to ultra-high strain rate loading conditions.

The dissertation of Dariush Seif is approved.

William Klug

Christopher Lynch

Jenn-Ming Yang

Nasr M. Ghoniem, Committee Chair

University of California, Los Angeles

2013

To my dear wife, Jamie M. Seif

Contents

List of Figures

List of Tables

ACKNOWLEDGMENTS

I would first like to acknowledge each individual whose name appears in the works referenced in the bibliography of this dissertation. Without the great work of my contemporaries and of those who came before me, the advances of my research would certainly not have been made possible. Also my sincere thanks to the United States Department of Energy Nuclear Energy University Programs for granting me a very generous fellowship, allowing for freedoms that not every doctoral student gets to enjoy.

To Professor Shahram Sharafat I extend my warmest gratitude for seeing potential in me as a student and for encouraging me to pursue that which seemed out of reach to me. For making this opportunity possible for me, to you I am truly indebted.

To the lifelong friends I have met and had the privilege to work with in our group, its hard to put in words what your friendships have meant to me. To Drs. Giacomo Po and Tamer Crosby, I will now be at a severe disadvantage not having your useful advice a few steps away. It was a joy to work alongside you and travel the globe with you both.

To my parents, Sadraddin and Shannon, you have taught me the true meaning of love and generosity over many years. None of this would have been possible without your love for each other and your love for me.

To my sisters, Leilah and Shireen, my dear Willa, my other family, the Diaz's, my brothers, Zachery, Kabir, John, Robert; I thank you for all of your love and support. To my Aunt Kathleen who showed me the meaning of true hospitality while I worked for two summers in the bay area, I am sincerely grateful.

To my wife, Jamie, I am very grateful that God brought us together. I look forward to all of our adventures together and our little ones to come. Thank you for your patience and understanding when things got heavy and for your continued support. I love you.

Lastly, I would like to thank my advisor, Professor Nasr M. Ghoniem. Under your tutelage I have learned much about being an effective scientist, but possibly even more about integrity and respect. I consider it an honor and a privilege to have had your guidance available to me during these years. I look forward to fruitful collaborations in the future.

Vita

2010-2013	Nuclear Energy University Programs Fellowship United States Department of Energy
2007-2010	Master of Science, Mechanical Engineering University of California, Los Angeles
2004-2007	Bachelor of Science, Mechanical Engineering University of California, Los Angeles

Publications

Seif, D., Ghoniem, N.M. (2013): *Effect of Anisotropy, SIA Orientation, and One-Dimensional Migration Mechanisms on Dislocation Bias Calculations in Metals*. Journal of Nuclear Materials, url: `http://dx.doi.org/10.1016/j.jnucmat.2013.02.083`).

Seif, D., Ghoniem, N.M. (2012): *Dislocation Bias Calculations in Metals Using a Combined Finite Element Rate-Theory Approach*, Effects of Radiation on Nuclear Materials, STP 1547, T. Yamamoto, Guest Editor, pp. 1−12, doi:10.1520/STP103987, url: `http://www.astm.org/DIGITAL_LIBRARY/STP/PAGES/STP103987.htm`.

Youssef, G., Crum, R., Prikhodko, S.V., **Seif, D.**, Po, G., Ghoniem, N.M., Kodambaka, S., Gupta, V. (2012): *The Influence of Laser-Induced Nanosecond Rise-Time Stress Waves on the Microstructure and Surface Chemical Activity of Single Crystal Cu Nanopillars*, Journal of Applied Physics, url: http://jap.aip.org/resource/1/japiau/v113/i8/p084309_s1.

Seif, D., Ghoniem, N.M. (2012): *A Review of the Rate Theory of Defect Clustering in Irradiated Materials*, OECD/Nuclear Energy Agency Volume on Multiscale Materials Modeling, (in press), Edited by V. Tikare.

Chen, Z., Kioussis, N., Ghoniem, N.M., **Seif, D.** (2010): *Strain-field effects on the formation and migration energies of self interstitials in alpha-Fe from first principles*, Physical Review B 81, 094102, url: http://prb.aps.org/abstract/PRB/v81/i9/e094102

Chapter 1

Introduction

1.1 Materials under High Energy Particle Irradiation

1.1.1 Physics of Material Defects

The generation of point-defects in materials stems from two primary types of neutron interactions with bulk materials. These are known as elastic and inelastic interactions and are caused by fundamentally different interactions, leading to the production of different types of defects within materials. Elastic interactions occur when incoming neutrons transfer their kinetic energy to a host lattice atom. If the energy transferred by the neutron in this collision is greater than the displacement threshold energy (E_{th}) of the lattice atom, then the atom will be ejected from its lattice site. This initial ejected atom is called the primary knock-on atom (PKA). This process leads to the production of a vacancy and a self interstitial atom (SIA) within the host lattice. Upon ejection from it's lattice site, if the PKA still carries greater kinetic energy than E_{th}, it will lead to the ejection of a secondary knock-on atom, and so on. This successive chain of elastic collisions and scattering is referred to as cascade damage and has been studied extensively both experimentally and computationally. The physics of the generated defects has also been a topic of numerous studies within the field of radiation damage for some time. It is well known that both vacancies and SIA's agglomerate into clusters of different sizes. Vacancies combine to form three dimensional (3-D) voids in the vicinity of the primary damage site while SIA's typically combine to form 2-D glissile or sessile dislocation loops on the periphery. Studies have shown that glissile loops are highly mobile and perform 1-D random motion in their slip direction. The production of Frenkel-pairs and resulting clusters populate the microstructural atmosphere are known to lead to hardening, swelling and creep phenomena in irradiated metals. Inelastic interactions occur under high-energy irradiation conditions leading to (n, α) transmutation reactions within the host lattice. These interactions lead to the production of significant quantities of solute atoms within the bulk, namely helium and hydrogen. Helium is highly insoluble in metals and therefore highly mobile inside matrix materials. The rapid migration and subsequent capture of helium interstitials to system sinks such as vacancy voids produces stable, pressurized helium-vacancy clusters. The formation of these clusters further enhances radiation-induced swelling and leads to reduced ductility by mitigating dislocation mechanisms in plasticity.

1.1.2 Effects on Mechanical Properties

The aforementioned defects cause drastic deterioration of the mechanical properties of fusion reactor materials. Over the past few decades countless experimental studies have been performed monitoring the effects of these nanodefects on macroscopic mechanical properties. Figure 1.1 shows a transmission electron micrograph of a 300 series stainless steel specimen irradiated to 10 dpa at 500°C [1]. The radiation damage environment is a complex network of various intrinsic and foreign defects with processes spanning time scales on the order of atomic vibrations to reactor lifetimes and length scales accounting for atomic size point defects all the way to grain boundary

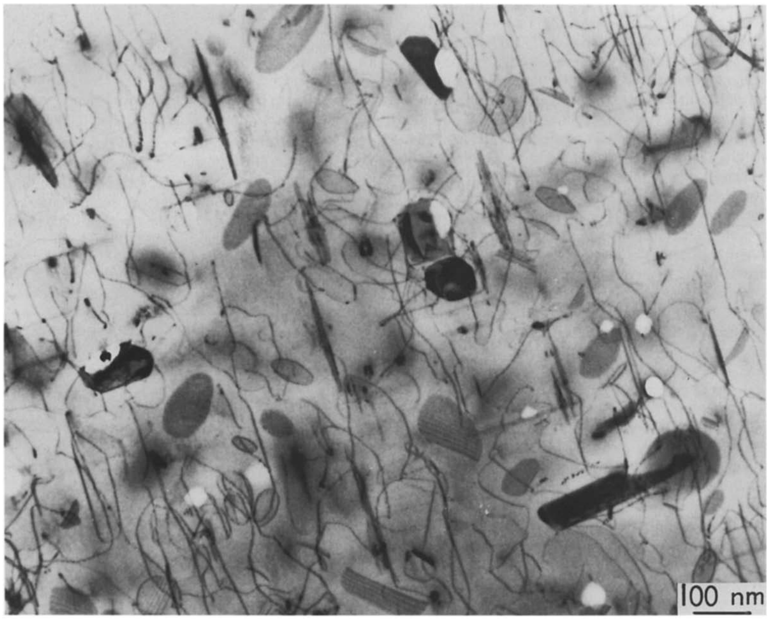

Figure 1.1: Transmission electron micrograph of a 300 series stainless steel specimen irradiated to 10 dpa at 500°C [1]

dynamics and beyond. In figure 1.1 we see represented, many of the extended defects that account for property changes in the material upon irradiation. Dislocation lines are seen as the tangled dark lines, weaving throughout space. The shaded elliptical images represent planar dislocation loops formed by the aggregation of SIAs. The light images are vacancy clusters (voids) in the material and the very dark images are foreign precipitates.

It has been well established that the deformation behavior of metals irradiated at temperatures below the recovery stage V (T $<$ 0.3-0.4 T_m where T_m is the melting temperature) exhibit a significant amount hardening [2]. The increased strength however is accompanied by a sudden yield drop and a great loss in ductility as evidenced in figure 1.2. This phenomena is known as low temperature embrittlement and is a leading concern in nuclear materials research. Various theoretical models

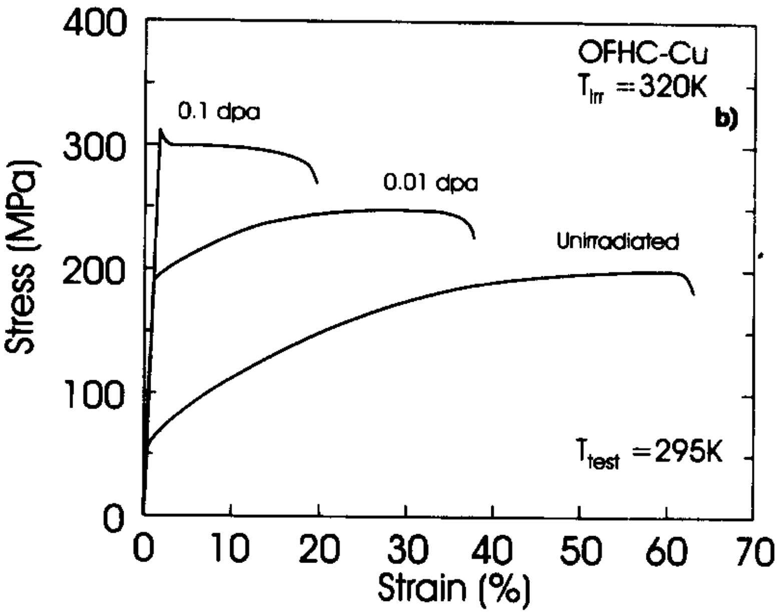

Figure 1.2: Polycrystalline Cu irradiated with fission neutrons at 320K [2]

have been constructed to explain this phenomena but the most commonly accepted is the cascade-induced source hardening model of Singh and Co-workers [2]. This model argues that dislocation production and motion is inhibited by the blockage of Frank-Read sources by decorations of small SIA clusters produced by intracascade clustering. Depending on the distribution of loops in the vicinity of these sources, a much higher upper yield stress can be expected to unlock them and initiate plastic flow in the material. The presence of helium leads to increased embrittlement especially at higher irradiation temperatures due to bubble formations at grain boundaries. Swelling in irradiated materials is another cause for concern and occurs as a consequence of the segregation of the self-interstitial and vacancy populations. For most metals this occurs in the temperature range of 0.3 T_m <T< 0.55T_m. While SIAs generated by neutron bombardment preferentially migrate to dislocations and grain boundaries, vacancies agglomerate into voids causing swelling in the material. Figure

1.3 is a photograph of a highly irradiated stainless steel specimen showing extensive swelling [1]. Through experimental studies it has been shown that martensitic ferritic steels exhibit swelling at $\sim 0.1\%$/dpa, while austenitics typically show $\sim 1\%$/dpa.

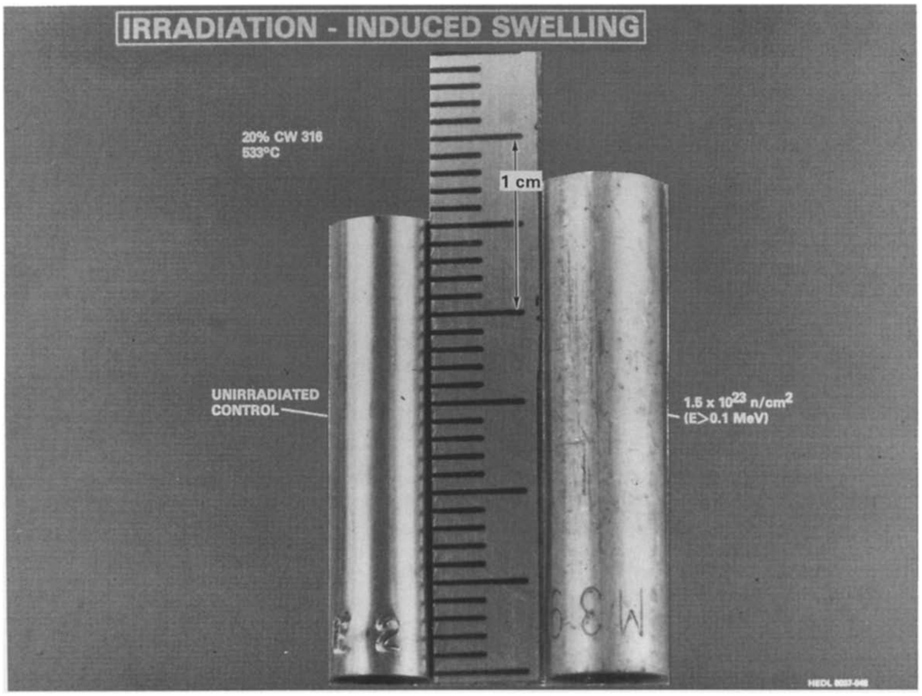

Figure 1.3: 316 stainless steel rods before and after irradiation at 533°C at a fluence of 1.5×10^{23} n/m^2 [1]

1.1.3 Energetics of Material Defects

The formation energy of a defect is typically defined as the difference in the total energy (at zero temperature) of the system containing the defect and that of a system of the same number of atoms in their lowest energy configurations. These energies are commonly used to determine equilibrium concentrations of defects. As an example, the formation energy of a carbon impurity atom in an iron crystal containing N

atoms, can be calculated as

$$E_C^f = E(N, 1) - N\mu_{Fe} - \mu_C. \tag{1.1}$$

Here, $E(N+1)$ is the energy of the system containing the defect and μ_α represents the chemical potential of element α. The chemical potential for iron and carbon are equal to the energy per atom in a perfect bcc iron and graphite lattice, respectively. These calculations are best performed using first-principles techniques. The migration energy (E^m) of a defect represents the activation energy of diffusion within the crystal lattice. Lattice vibrations may result in an atomic jump to a neighboring site only if the diffusing defect is carrying kinetic energy equal to or greater than the migration energy. Accurate calculations of migration energies may be obtained using minimum energy pathway (MEP) search methods such as the nudged elastic band (NEB) method and the dimer method. These methods allow relaxations of the lattice around the defect as the defect treks the reaction coordinate to the final state. The point of maximum energy along the path represents the saddle point and the migration energy can be calculated as the difference in energy between the saddle point configuration and the initial state. The aggregation of point-defects following collision cascades leads to the formation of defect clusters in materials. The stability of radiation-induced defect clusters against dissociation is governed by the binding energy (E^B). The binding energy is defined as the energy required to dissociate a bound system into its constituent parts. These energies of can be calculated in terms of formation energies under the assumption that the products of dissociation are infinitely separated. For a dissociative reaction of type $C \rightarrow A + B$, the binding energy can be calculated as

$$E_C^B = E_A^f + E_B^f - E_C^f. \tag{1.2}$$

The energy required for the emission of a point-defect from a cluster is then taken as the binding energy plus the migration energy of the point-defect. Tables 1.1 and 1.2 give relevant energy barriers and defect-configurations in bcc iron and tungsten, and fcc copper and nickel, respectively. These values are obtained from various sources where first principles calculations and molecular statics with empirical potentials calculations were used. Additionally, the studies of Fu and Willaime [6] and Caturla et al [7] provide extensive first principles studies of SIA and He energetics in Fe.

Process	Fe	W
Vacancy Form.	*2.12* [8], *2.15* [9]	*3.11* [10], *3.16* [11]
Vacancy Mig.	*0.67* [6], *0.64* [9], 0.87 [12]	*1.66* [10], *1.78* [9], 1.8 [13]
Divacancy Form.	3.18 [14]	6.70 [15]
Divacancy Mig.	*0.62* [6]	1.95 [16]
Interstitial Type	[110]-split	[111]-split
Interstitial Form.	*3.86* [17], *3.93* [9]	*9.82* [10], *9.548* [9]
Interstitial Mig.	*0.34* [6], 0.30 [18], 0.167 [12]	*0.013* [9]
SIA Cluster Mig.	$0.059+0.067/n^{1.3}$ [19][1]	-
He Interstitial Type	Tetrahedral	Tetrahedral
He Interstitial Form.	*4.40* [7], *3.37* [20]	6.16 [10], *6.19* [11]
He Interstitial Mig.	*0.06* [7]	*0.07* [11]
He Substitutional Form.	*4.23* [7], *4.08* [20]	4.70 [10], *4.77* [11]
He Substitutional Bind.	*2.3* [7]	*4.57* [10], *4.58* [11]
HeV_2 Mig.	*1.08* [8]	-

Table 1.1: Relevant energy barriers (in eV) for radiation-induced defect processes in BCC Fe and W. Values in italic represent results of first principles studies.

Process	Cu	Ni
Vacancy Form.	1.28 [21], 1.3 [13]	1.62 [22], 1.60 [23], 1.60 [24]
Vacancy Mig.	0.72 [13]	1.30 [23], 1.29 [24]
Divacancy Form.	2.0 [25]	3.02 [22]
Divacancy Mig.	0.55 [12]	*0.59* [26]
Interstitial Type	[100]-split	[100]-split
Interstitial Form.	2.73 [27]	4.91 [24], 4.93 [27]
Interstitial Mig.	0.078 [28], 0.13 [12]	0.16 [27]
He Interstitial Form.	1.97 [29]	4.06 [30]
He Interstitial Mig.	0.5 [31], 0.63 [32]	0.66 [32], 0.81 [33]
He Substitutional Form.	*2.58* [34]	3.13 [22], *3.23* [34]

Table 1.2: Relevant energy barriers (in eV) for radiation-induced defect processes in FCC Cu and Ni. Values in italic represent results of first principles studies.

1.2 Materials Deforming under Ultra-High Strain Rates

The mechanisms of deformation of materials under ultra-high strain rates, arising from exposure to explosive impacts, differs greatly from that due to standard mechanical testing. Under such conditions, materials have been found to exhibit unique behavior including enhanced mechanical strength [35]. Above certain threshold impact stresses, the shock front, characterized by an abrupt change in material density, propagates as a dual elastic and plastic front. When faced with internal and external material interfaces (free surfaces, grain boundaries, etc.), interactions of reflected waves can lead to the formation of voids and spallation in the material. Due to the stochastic nature of defect nucleation, and the very short timescales involved, molecular dynamics simulations offer great insight into the atomic processes involved in shock deformation. Modern large-scale atomistic simulations of metals under shock loading began with the MD simulations of Holian and Lombdahl [36]. Their studies in single crystal nanostructures with periodic boundary conditions (nanofilms) revealed the homogeneous nucleation of partial dislocations at the shock front, relieving compressive stresses and accommodating the increased density at the shock front. In recent years, this work has been extended to even larger systems in both perfect single and polycrystals and those with pre-existing defects such as dislocations and voids [37, 38, 39, 40, 35, 41, 42]. While these results remain useful for studies of bulk metals, it remains unclear to what extent these results are applicable to nanostructures of finite size. In a recent paper, we reported on the fabrication and laser-induced shock-loading of 100-oriented, single-crystal copper nanopillars, with pillar axes aligned with the wave propagation (compression) direction [5]. An apparatus and related test procedures were developed for the compression of these nanopillars at pressures and strain rates greater than 1 GPa and 10^7 s^{-1}respectively, using nanosecond pulse laser-generated stress waves. Results showed evidence of surface activation due to surface step creation by dislocation-driven processes. In the past MD simulations in bulk samples, however, impact stresses on the order of 35 GPa were required to nucleate and propagate dislocations; much greater than the stresses produced in the laser experiments.

In this thesis, we work to examine the mechanisms of deformation in nanopillars two different types of copper nanostructures via non-equilibrium MD simulations. Expanding on past simulations, we describe and show the mechanisms of high strain-rate plasticity in nanofilms and compare them with those found in finite-sized nanopillars,

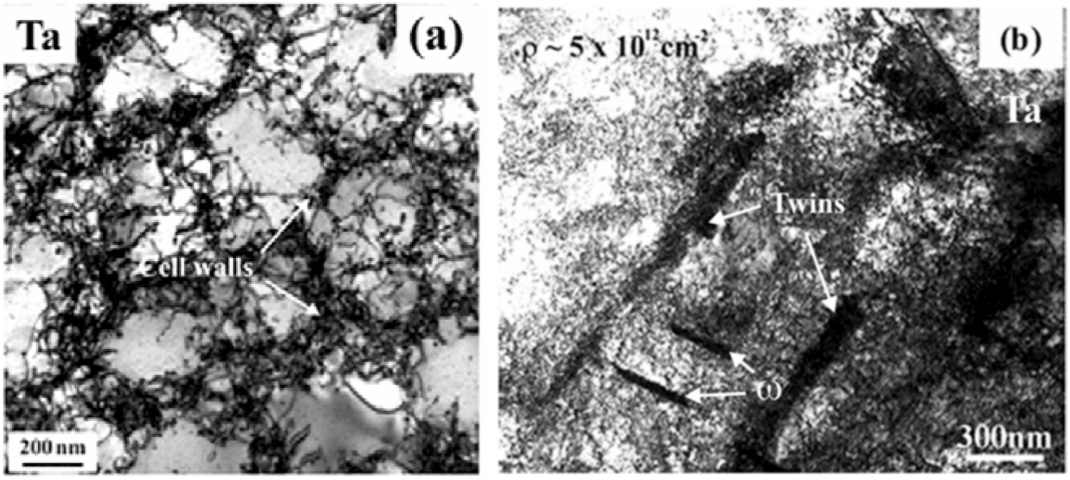

Figure 1.4: Bright field TEM images of shocked pure tantalum demonstrating (a) the formation of cellular dislocation structures and (b) a dense and evenly distributed dislocation structure co-existing with twins and ω phase domains in pure Ta shocked at 45 GPa [3].

with sizes approaching those synthesized experimentally. The imposed loading conditions are designed to reveal the structure of propagating shock waves and their release at the free surface. A detailed examination of the effects of anisotropy and impact magnitude on the observed plasticity is given. Also, a binning analysis is performed to track stress, temperature and velocity profiles in the shocked samples.

Chapter 2

Elastic Representation of Radiation-Induced Point Defect Fields in Metals

Internal structural components which operate in nuclear fusion environments are subject to significant damage doses stemming from the onslaught of 14 MeV neutrons produced in the D-T cycle. The internal production of point-defects such as self-interstitial atoms (SIA) and vacancies from elastic interactions, and helium from (n,α)-reactions lead to severe material degradation over time, including swelling [1] and low-temperature embrittlement [2]. The prediction of damage evolution and component lifetime is highly dependent upon accurate models of point-defect production and interactions within the material. The development of truly predictive long-timescale simulation techniques has been quite scarce in recent history due to the trade-offs between computational efficiency and rigorous physical treatments. While an accurate physical model of damage accumulation and evolution requires a comprehensive understanding of point-defect energetics and interactions, there has been an absence in many studies [43, 44, 45] of the consideration of local strain environment effects on defect migration properties and stability. The study of defect diffusion in strain fields has been a topic of interest for some time now. Koehler calculated changes in migration barriers of vacancies to be altered by as much as 10% in the vicinity of dislocations and interstitial clusters [46]. Dederichs and Schroeder showed that anisotropic defect diffusion is the result of saddle point anisotropies in strained crystal lattices [47].

The goal here is to combine atomistic simulation with elasticity theory to implement the method of force multipoles to represent defects, and use continuum elasticity calculations to quantify interactions between these defects and with various strain fields. Emphasis will be placed on the importance of including higher-order terms in the multipolar expansion. These interactions can be made available to future KMC simulations to account for strain-biased diffusion, and give a physically-based description of the accumulation and evolution of damage in irradiated metals. The chapter is organized as follows. In section 2.1 the elastic Green's tensor function for infinite isotropic media is derived. In section 2.2 we derive the force multipole representation of point defect representation in continuous media. In section 2.3 we describe in detail our hybrid method for calculating multipolar values. Several cases are presented in section 2.4 where the method is applied to radiation-induced defects in α-iron, and the results are compared with molecular statics calculations. Multipolar values and the full formation volume tensor for these defects are also presented.

2.1 Elastic Green's Function

Green's tensor functions describe the elastic displacement response of a linear elastic solid to an applied point force. In the field of defect mechanics, they have become invaluable as a predictive tool for many problems of interest. Green's function solutions vary between situations, due to their dependence on both the material's structure and also the prescribed boundary conditions. For the current research it is necessary to derive the Green's function for infinite space with the assumption of isotropy (since bcc Fe has relatively low anisotropy).

First it is necessary to define the Green's function $G_{ij}(\mathbf{r})$ as the i^{th} Cartesian displacement component at a field point $\mathbf{r}$, due to a point force f located at the origin acting in the j^{th} direction. Following continuum elasticity theory, the condition for equilibrium can be expressed as

$$C_{ijkl}u_{k,lj} + f_i = 0, \tag{2.1}$$

where C is the elastic constants tensor and the summation convention of repeated indices is implied. Taking the point force in the m-direction, it can be rewritten in terms of the Dirac delta function $\delta(\mathbf{r})$ as

$$f_i = \delta_{im}\delta(\mathbf{r}). \tag{2.2}$$

Following the method of solving the equilibrium equation via the Fourier transform method, the Fourier space Green's function is expressed as

$$\tilde{G}_{km}(\mathbf{k}) = \int_V G_{km}(\mathbf{r})e^{-i\mathbf{k}\cdot\mathbf{r}}dV. \tag{2.3}$$

The Fourier space Equilibrium condition can then be written as

$$C_{ijkl}k_l k_j \tilde{G}_{km}(\mathbf{k}) = -\delta_{im}. \tag{2.4}$$

Assuming an isotropic material, the elastic constants tensor may be expressed in terms of the two Lamé's constants, λ and μ, as

$$C_{ijkl} = \mu(\delta_{ik}\delta_{jl} + \delta_{il}\delta_{jk}) + \lambda\delta_{ij}\delta_{kl}. \tag{2.5}$$

Substitution of 2.5 into 2.4, and applying algebraic simplifications yields

$$(\lambda + \mu)k_i k_m \tilde{G}_{mj}(\mathbf{k}) + \mu k^2 \tilde{G}_{ij}(\mathbf{k}) = \delta_{ij}. \tag{2.6}$$

In k-space the Green's function can be found by multiplying 2.6 by k_i and summing over i, which gives

$$k_m \tilde{G}_{mj}(\mathbf{k}) = \frac{k_j}{(\lambda + 2\mu)k^2}. \tag{2.7}$$

By direct substitution of 2.7 into 2.6, the k-space Green's function can be solved for as

$$\tilde{G}_{ij}(\mathbf{k}) = \frac{1}{\mu k^2}\left[\delta_{ij} - \frac{\lambda + \mu}{\lambda + 2\mu}\frac{k_i k_j}{k^2}\right]. \tag{2.8}$$

Finally applying the inverse Fourier transform to 2.8, the Cartesian space Green's function is found to be

$$G_{ij}(\mathbf{r}) = \frac{1}{8\pi\mu(\lambda + 2\mu)}\left[(\lambda + 3\mu)\frac{\delta_{ij}}{r} + (\lambda + \mu)\frac{x_i x_j}{r^3}\right] \tag{2.9}$$

This explicit form of the Green's function allows for the solution of many problems in linear elasticity. In terms of the Green's function, the displacement vector can be written as

$$u_k(\mathbf{x}) = \int_{\mathrm{V}} G_{km}(\mathbf{x} - \mathbf{x}')\mathbf{f_m}(\mathbf{x}')\mathbf{dV}. \tag{2.10}$$

2.2 Force Multipole Representation of Defects

2.2.1 Point Defect Displacement Fields

The insertion of a point-defect into a perfect crystalline lattice results in a displacement field around the defect on surrounding atoms. This displacement field is typically modeled using one of several approaches. Eshelby developed a very simple and elegant way to approach the problem within the confines of elasticity theory [48]. He treated the point-defect as a center of dilatation, modeled as a spherical inclusion within an elastic isotropic medium, whose strength may be determined from experiment. This model is only suited, however, to describe defects of high symmetry acting in materials with negligible anisotropy. Another method, proposed by Kanzaki, involves representing the defect as an array of forces located on neighboring atomic sites [49]. Generally called the method of 'Kanzaki forces', this method has been successfully implemented in the past, for example, to give the atomic displacements around vacancies in Cu and Al [50]. However, this approach suffers from a few inherent limitations. Among them, the formulation requires the spatial extent of these forces to be as restricted as possible, typically to first nearest neighbor atoms. For this reason, the elastic response of the material must be modeled with complex 'lattice' Green's functions that have no closed form expression to account for the displacements inherent in a defected crystalline lattice [51]. In addition, each point-force will introduce a singularity, and additional effort will be required to mitigate divergence in the computations.

For application to general radiation-induced defects, we have found the method of force-multipoles to be most beneficial. In this method, the defect is represented as a multipolar expansion of forces acting at the center of the defect. For derivation of the method, we follow the work of Siems [52] and Teodosiu [53]. As in the Kanzaki approach, the addition of a point-defect in a perfect crystal can be alternatively represented as a configuration of point- forces acting on all affected, neighboring atoms. If we consider a defect at the origin surrounded by N atoms (ν) with separation vectors $\boldsymbol{l}^{\nu}$ from the defect, the displacement field caused by the defect can expressed as

$$u_m(\boldsymbol{x}) = \sum_{\nu=1}^{N} G_{ms}(\boldsymbol{x} - \boldsymbol{l}^\nu) F_s^\nu, \tag{2.11}$$

where $\boldsymbol{G}(\boldsymbol{x})$ is the elastic Green's tensor function of the material and $\boldsymbol{F}^\nu$ are the point- forces acting on initial lattice atom locations $\boldsymbol{l}^\nu$. We note here that repeated indices imply summation. Expanding $\boldsymbol{G}(\boldsymbol{x} - \boldsymbol{l}^\nu)$ in a Taylor's series about $\boldsymbol{x}$ gives

$$G_{ms}(\boldsymbol{x} - \boldsymbol{l}^\nu) = G_{ms}(\boldsymbol{x}) + G_{ms,n}(\boldsymbol{x}) l_n^\nu + \frac{1}{2!} G_{ms,nq}(\boldsymbol{x}) l_n^\nu l_q^\nu + ... \tag{2.12}$$

Plugging this Green's function expansion back into (2.11), the displacement field can be rewritten as

$$\begin{aligned} u_m(\boldsymbol{x}) &= \sum_{k=0}^{\infty} \frac{1}{k!} G_{ms,q_1...q_k}(\boldsymbol{x}) P^{(k)}_{q_1...q_k s} \\ &= G_{ms}(\boldsymbol{x}) P_s^{(0)} + G_{ms,n}(\boldsymbol{x}) P_{ns}^{(1)} + G_{ms,nq}(\boldsymbol{x}) P_{nqs}^{(2)} + ... \end{aligned} \tag{2.13}$$

where

$$P^{(k)}_{q_1...q_k s} = \sum_{\nu=1}^{N} l_{q_1}^\nu ... l_{q_k}^\nu F_s^\nu \tag{2.14}$$

are called the multipole moments of k^{th}-order. It is important to note that the $k = 0$ moment represents a sum of the applied force vectors over all atoms, which equals zero for equilibrium conditions to be satisfied. The $k = 1$, 2 and 3 moments are called the dipole, quadrupole, and octopole moments.

The displacement equation (2.13) states that the elastic response of a defected material requires knowledge of the Green's function of the material and the values of the multipole moments of the defect. We point out that this differs greatly from the Kanzaki approach in that all forces and higher-order moments occur at the center of the defect, and not on lattice sites. To lowest order, the defect can be represented by the dipole tensor as is usually the case for defects of high symmetry (vacancies, interstitials, etc).

2.2.2 Point Defect Interaction Energies

The lifetime and fate of point-defects operating in radiation damaged environments are governed by the many elastic interactions they may have with any number of other defects within the host material. These interactions affect the stability and migration tendencies of defects and have been a topic of great concern within the nuclear materials community for some time. In the force-multipole approach, the interaction energy of a defect in an existing elastic displacement field can be described as a sum over all surrounding atoms of the force applied to the atom multiplied by the induced displacement, or

$$E_{int} = -\sum_{\nu=1}^{N} \boldsymbol{F}^{\nu} \cdot \boldsymbol{u}(\boldsymbol{x} + \boldsymbol{l}^{\nu}). \tag{2.15}$$

By expanding $\boldsymbol{u}(\boldsymbol{x} + \boldsymbol{l}^{\nu})$ in a Taylor's series about $\mathbf{x}$ and plugging it back into (2.15), we can express this energy in terms of the multipolar moments as

$$\begin{aligned} E_{int} &= \sum_{n=1}^{\infty} \frac{1}{n!} u_{m,q_1 \dots q_n}(\boldsymbol{x}) P^{(n)}_{q_1 \dots q_n m} \\ &= -\left\{ P^{(1)}_{im} u_{m,i}(\boldsymbol{x}) + \frac{1}{2!} P^{(2)}_{ijm} u_{m,ij}(\boldsymbol{x}) + \frac{1}{3!} P^{(3)}_{ijkm} u_{m,ijk}(\boldsymbol{x}) + \dots \right\}. \end{aligned} \tag{2.16}$$

Thus, for a defect represented by multipolar tensors $\mathbf{P}^{(k)}$ operating in any displacement field $\boldsymbol{u}(\mathbf{x})$, the mutual interaction energy can be directly calculated by equation (2.16). While the force multipole method has lent itself to several studies of defect interactions in the past [54, 55], there has been no implementation of higher-order multipolar moments beyond the dipole tensor, to our knowledge. In addition, it has been previously discussed that centrosymmetric defects (vacancy, substitutional, etc.) will have vanishing octopole tensors, and the dipole tensor is sufficient to model these defects [56]. Our results show for nearly all defects, the higher-order terms including the octopole moment are necessary to describe the lattice displacements seen in atomistic calculations. We also note the exclusion of higher-order moments causes the effects of strain gradients to be neglected when interaction energies are computed. This assumption becomes particularly worrisome when defect separation is small. Under homogeneous strain conditions, however, and in the limit of large defect-defect separation, the interaction term can be computed solely in terms of the dipole moment as

$$E_{int} = -P_{ij}^{(1)} \varepsilon_{ij}. \tag{2.17}$$

In the case of defect interactions in spatially varying strain fields (dislocations, grain boundaries, other point- defects, etc.), a higher degree of accuracy can be obtained with the inclusion of higher-order moments.

The formation volume tensor of a defect is a quantity that describes of the interaction between the free energy of the defect and an externally applied stress. It represents the tensorial volume change of the system upon formation of the defect at its equilibrium position and contains contributions due to both crystal relaxation and the additional added atomic volume [57]. The formal definition is given as $V_{ij}^f = -\frac{\partial \tilde{G}^f}{\partial \sigma_{ij}}$, where $\tilde{G}^f$ is the Gibb's free energy at equilibrium and σ is the external stress. In terms of the formation volume tensor, the total change in energy of the system under an applied stress field σ, can be expressed as the equilibrium defect formation energy minus the work done by σ, or

$$E(\sigma) = E^f(0) - \sigma_{ij}V_{ij}^f. \tag{2.18}$$

Here, $E(\sigma)$ represents the formation energy of the defect in the applied strain field. The work done by the stress on defect formation represents an additional interaction energy beyond $E^f(0)$, and can also be expressed according to equation (2.17) as

$$\sigma_{ij}V_{ij}^f = P_{ij}^{(1)}\varepsilon_{ij}. \tag{2.19}$$

Plugging in the elastic constitutive equations, we can obtain a closed-form solution for the formation volume tensor in terms of the dipole tensor and elastic constants, as

$$V_{ij}^f = \frac{P_{ij}^{(1)}c_{11} - (trP^{(1)} - 2P_{ij}^{(1)})c_{12}}{3\kappa(c_{11} - c_{12})}\delta_{ij} + \frac{1}{2c_{44}}P_{ij}^{(1)}(1 - \delta_{ij}), \tag{2.20}$$

where the material is defined by elastic constants c_{11}, c_{12}, c_{44}, and the bulk modulus $\kappa = \frac{1}{3}(c_{11}+2c_{12})$. The trace of the formation volume tensor is known as the relaxation volume of a defect (V^r), and gives the change in volume of the system upon defect formation. It is a property solely determined by the defect strength and material properties. By inspection, the trace of (2.20) simplifies to

$$V^r = \frac{trP^{(1)}}{3\kappa}. \tag{2.21}$$

2.3 Solution Methodology

We have recently developed a hybrid method to compute the values for the multipolar moments of lattice defects using molecular statics (MS) calculations and continuum elasticity theory. To illustrate the method and its outcomes, we focus on radiation-induced defects in the bcc α-iron lattice. These defects include self-interstitial atoms (SIA), SIA clusters, helium point- defects, and helium-vacancy clusters. Our method first requires an atomistic simulation of the defect in the host lattice to acquire the displacement field around the defect. For our molecular statics calculations we have chosen interatomic potentials well suited for simulation of these types of defects. For Fe-Fe, Fe-He, and He-He interactions we have chosen the well known Ackland [58], Juslin-Nordlund [59], and Lennard-Jones [60] interatomic potentials, respectively. In our atomistic calculations the defect was introduced in the center of the simulation box and a static conjugate gradient relaxation (0 K) was performed to allow relaxation of the atoms. The lattice parameter used was 2.866 $\mathring{A}$. The supercell was a cube with an edge length of 18 lattice parameters (52 Angstroms) and periodic boundary conditions were applied on all sides. This cell size was found to be sufficient to contain the lattice distortions produced, with the total number of host Fe atoms being 11664. After performing the MS calculations, the next step is to use the atomic displacement information to obtain a multipolar representation of the defect. Taking another look at equation (2.13), we can alternatively view this equation as a matrix-vector multiplication of the form

$$\{u\} = [G]\{P\} \tag{2.22}$$

In this light, $\{u\}$ is a $3N$ by 1 column vector containing N triplet sets of the MS displacement vector components of N chosen neighboring atoms. A particular benefit of this approach is that N may be chosen quite freely and the extent of fitted neighbors need not be restricted, in contrast to the Kanzaki approach. For $N > \frac{N^{(k)}}{3}$, where $N(k)$ equals the total number of multipolar values chosen to be solved for (e.g. $N^{(1)} =$

9), the system of equations will be over determined. The column vector $\{P\}$ represents the values of the chosen multipolar moments used to describe the defect and has size $N(k)$ by 1. The matrix $[G]$ represents the corresponding elastic Green's function derivatives evaluated at the desired field point. This matrix has size $3N$ by $N(k)$. We have found that the use of the isotropic elastic Green's function provides adequate response of the material as compared to our MS calculations. This response function is well known and provides a tractable closed-form solution simplifying the necessary calculations. It can be expressed as

$$G_{ms}(\boldsymbol{r}) = \frac{1}{8\pi\mu(\lambda+2\mu)}\left[(\lambda+3\mu)\frac{\delta_{ms}}{r} + (\lambda+\mu)\frac{x_m x_s}{r^3}\right] \tag{2.23}$$

where the Lamé's constants λ and μ define the material, and $r = \sqrt{x_k x_k}$. The (k) multipole value also implies the order of derivative of the Green's function necessary for the calculations. For example, inclusion of the octopole tensor requires $G_{ms,pqr}(\boldsymbol{r})$ from equation (2.23). We also note these derivatives decay as $O(\boldsymbol{r}^{-(k+1)})$. With the values of $\{u\}$ and $[G]$ known from MS calculations and elasticity theory, respectively, equation (2.22) can be posed as a least squares optimization problem which can then be solved to obtain the multipole moment values $\{P\}$. This step has a significant benefit since displacements beyond the first few shells may also be used to extract information about the defect.

2.4 Applications

The focus of our research has been primarily on radiation induced defects in the bcc α-iron lattice. In this section we will highlight some representative results obtained for a small selection of defects that have been modeled with our approach.

2.4.1 Fe SIA $< 110 >$ dumbbell

Self interstitial atoms (SIA) are generated in significant quantities in fission, and to a larger extent, fusion reactors. They are produced in the wake of displacement cascades caused by incoming fluxes of high energy neutrons. Studies of the energetics and mechanisms of migration for these point-defects have been a topic of interest for many years. Single SIAs in α-iron take the form of a split dumbbell configuration. In the past, experimental studies [61], as well as ab-initio calculations [62, 63], have concluded the ground state configuration to be the $< 110 >$ dumbbell. In our MS calculations, we have found the formation energy to be 3.35 eV, which is in agreement with values reported previously by [64], but lower than those predicted by DFT [17]. Implementing our hybrid method for multipolar representation of this defect, we have calculated the multipolar moments up to the octopole tensor ($\mathbf{P}^{(3)}$). Calculated values for the dipole tensor are given in table 2.1. In figure 2.1 we have plotted the displacements versus distance from the defect center. The plots on the left and right show the radial and Cartesian components, of the displacements, respectively. The circles in these plots are those obtained from MS calculations, while the points represent the calculated displacements using the continuum elasticity (CE) multipolar representation via equation (2.13). We see very good agreement in the displacements predicted by the multipolar representation. First, it is important to note the complexity of the lattice response to this defect. In the first shell alone we see the very large expansion of the four atoms lying on the (110) plane with a contraction of the remaining four atoms. This immediately suggests any attempt to model this defect as an inclusion or center of dilatation would be in vain. In fact, we have found that without the use of the octopole moment, the dipole tensor alone cannot replicate these anisotropies. The largest contribution to elastic energy is contained within the

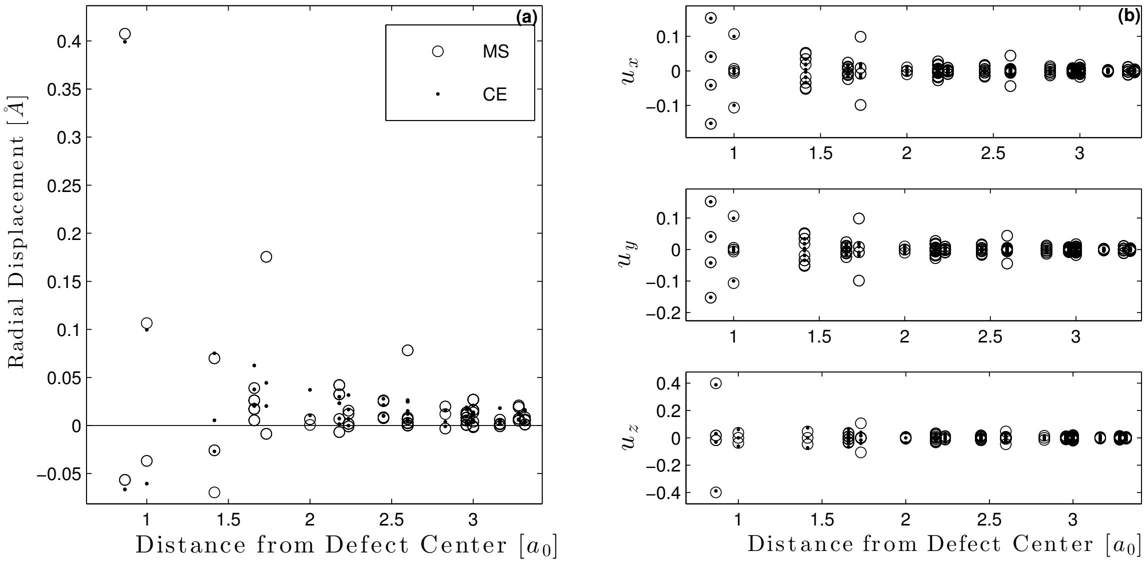

Figure 2.1: Displacement vs. radial distance plots for [110] Fe SIA: (a) Radial, (b) Cartesian components.

first few shells around the defect, and we see very good agreement in this vicinity. Values for relaxation volume and the formation volume tensors are given in table 2.2. We find the relaxation volume for this defect to be 1.48 Ω_{Fe}, which is in agreement with [55]. To obtain an overall quantity to compare the accuracy of the multipolar representation of the defect compared to the MS calculations, we have chosen to compare the predicted formation energies of both representations. To do this, we apply the multipole displacements to a perfect bcc Fe lattice and hold these new positions fixed, evaluating the system energy with the aforementioned interatomic potentials. This allows direct comparison of the formation energies between the two methods. We find the multipolar representation to give a formation energy of 4.02 eV giving a percent difference of roughly 20% with the MS value. This over-prediction stems from the inherent inability of continuum elasticity to account for all of the intricate atomic interactions that occur within the discrete atomic lattice. We also note this

	$P_{11}^{(1)}$	$P_{22}^{(1)}$	$P_{33}^{(1)}$	$P_{12}^{(1)}$	$P_{23}^{(1)}$	$P_{13}^{(1)}$
Fe [110] Dumbbell	20.02	20.02	18.22	-9.107	0.00	0.00
Vacancy	-1.23	-1.23	-1.23	0.00	0.00	0.00
Tetrahedral He	5.77	5.58	5.77	0.00	0.00	0.00
Octahedral He	5.37	5.37	8.73	0.00	0.00	0.00
Substitutional He	3.51	3.51	3.51	0.00	0.00	0.00
$He_{12}V_4$ Cluster	63.62	70.6168	71.5132	0.6115/-0.0134*	0.00	0.00

Table 2.1: Computed dipole tensor values (in eV) for selected defects in α-Fe. * $P_{12}^{(1)}/P_{21}^{(1)}$ given for $He_{12}V_4$ cluster.

percent difference lies within the variations of several Fe interatomic potentials [65].

We have also recently studied the effect of deformation on the formation energy of SIAs in α-iron [17]. Ab-initio calculations were made for various strain loadings of volumetric and uniaxial type, and results were compared to MS calculations and the method described here. In the volumetric strain studies we found very good agreement in the energetic trends. The linear behavior of energetic favorability of defect formation under lattice expansion was predicted by the continuum approach and verified by the MS and ab-initio calculations. Under uniaxial strain in particular we found nearly identical prediction of the formation energy in the MS and multipolar calculations.

2.4.2 Helium Point Defects and Clusters

Extrinsic radiation induced defects are well known to contribute to the mechanisms of damage accumulation and evolution in irradiated materials. Substantial quantities of helium atoms are generated within the α-iron lattice by (n,α) transmutation reactions.

	V^r	V^f_{11}	V^f_{22}	V^f_{33}	V^f_{12}	V^f_{23}	V^f_{13}
Fe [110] Dumbbell	1.48	0.579	0.579	0.322	-0.5525	0.00	0.00
Vacancy	-0.0938	-0.0313	-0.0313	-0.0313	0.00	0.00	0.00
Tetrahedral He	0.435	0.1543	0.1543	0.1263	0.00	0.00	0.00
Octahedral He	0.495	0.0055	0.0055	0.4837	0.00	0.00	0.00
Substitutional He	0.2672	0.0891	0.0891	0.0891	0.00	0.00	0.00
$He_{12}V_4$ Cluster	5.32	1.0474	2.0724	2.1965	0.0178	0.00	0.00

Table 2.2: Computed relaxation volumes and formation volume tensor values for selected defects in α-Fe. Values given in atomic volume units ($\Omega_{Fe} = 11.79\AA^3$).

Helium is highly insoluble in iron and thus interstitials rapidly migrate with an energy barrier less than 20% than that of Fe interstitials [7]. We have undergone calculations of the multipolar moments for helium in tetrahedral, octahedral, and substitutional configurations. The results for these calculations are found in table 2.1. Figure 2.2 (a) shows the radial displacement versus distance for the octahedral interstitial. We see excellent agreement in the first four atomic shells, with an over-prediction in the slightly anisotropic fifth shell, but good decay agreement in the shells that follow. Similar results are found for the tetrahedral configuration. In both cases, we found it necessary to implement the quadrupole and octopole moments in order to get good matching for the displacements in the shells near the defect core. Comparing the formation energies between MS and the multipole representation, we found the percent difference to be only 0.89% between the continuum value (4.49 eV) and the MS value (4.45 eV) for the octahedral interstitial. The relaxation volume of the octahedral helium is also found to be 12% larger than that of the tetrahedral, which shows our multipolar representation predicts the tetrahedral position is energetically

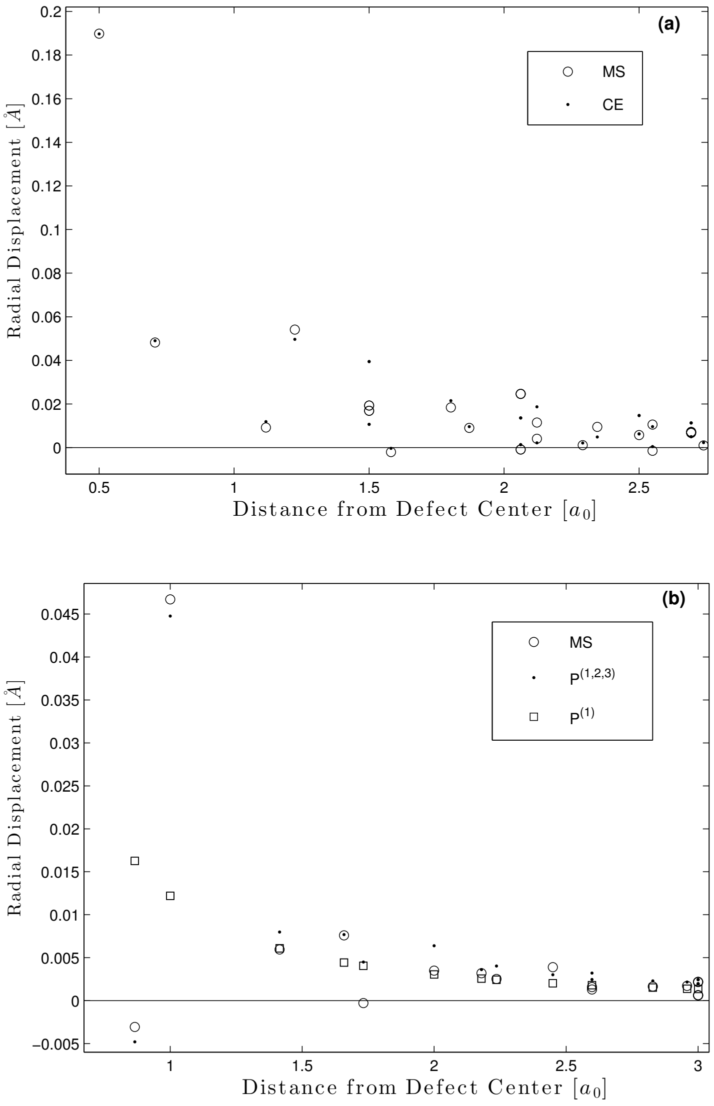

Figure 2.2: Radial displacement vs. distance plots for helium point-defects in α-Fe: (a) Octahedral interstitial, (b) Substitutional.

more favorable than the octahedral, consistent with DFT calculations [66].

In figure 2.2(b), we see the displacement field generated by the substitutional helium is somewhat more complex. Here we have plotted the MS displacements along with both the multipolar predictions using up to the octopole moment (points) and using only the dipole moment (squares). This plot illustrates the inability of the $1/r$ decay of the dipole moment to capture the lattice response seen in the atomistics. In fact, closer inspection revealed the increased accuracy from the squares to the points can be attributed to the octopole moment alone, with negligible contribution of the quadrupole moment. In our MS calculations we find a 0.307 pm radial contraction of the 8 nearest neighbors, contrasted by a 4.67 pm expansion of the 6 second nearest neighbors. This behavior is typically not well suited for classical linear elasticity and we find the use of the octopole tensor as a means to suitably account for the discontinuity. Our calculations give a percent difference of 33% and 2.3% in the radial displacements of the first two shells, respectively, and we find the octopole tensor to assume only six non-zero components. We note the large percent difference in the first shell is due to the very small contraction, and does not influence the resulting defect energy to the extent of the second shell.

The rapid diffusion of helium interstitials within the host lattice is halted as they meet their fate at system sinks such as dislocations, grain boundaries, and vacancy voids. Helium has long been known to stabilize voids against their otherwise collapse by vacancy emission, and lead to swelling in the material. The stability and migration energetics of helium-vacancy clusters (He_nV_m) have been studied in the past using atomistic simulations [67, 7]. We have also found the hybrid multipole method to accurately reproduce the displacement fields of He_nV_m clusters seen in MS calculations. These defects carry additional complexity due to the asymmetry of both the defect itself, and the lattice surrounding the core. These asymmetries lead to significant anisotropies in the displacement response. We describe here the results of our calculations for a $He_{12}V_4$ cluster. The defect was created by adding 12 atoms into 4 vacancies in a quasi-random fashion. Dynamics were then run at 100 K for

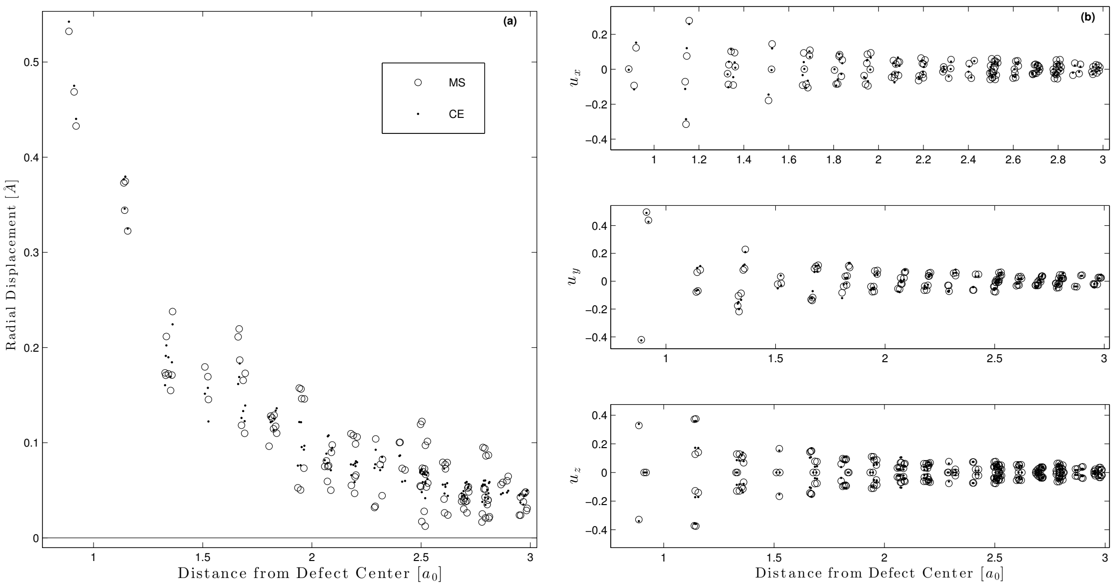

Figure 2.3: Displacement vs. radial distance plots for $He_{12}V_4$ cluster: (a) Radial, (b) Cartesian components.

1 ns allowing the cluster reach a more energetically favorable configuration. Lastly the defect and lattice were allowed to relax at 0 K. In the elastic representation, the defect was modeled using the dipole, quadrupole, and octopole moments. Figure 2.3 shows the highly anisotropic displacement field resulting from the MS calculations and the multipolar fit. The center of the defect was taken to be the mass center of the helium atoms within the cluster in the final configuration, which explains the minor radial variations in the shell distances in the plots. We note the very close agreement in the atomic displacements within the first several shells of the defect center, and general agreement in the decay characteristics beyond that. We see the isotropic elasticity solutions provide accurate response when higher-order moments are included. A comparison of defect formation energies of both methods revealed only a 1.65% underprediction of the multipolar representation compared to the MS value (35.94 eV). We note the asymmetry of the dipole tensor for this defect as seen in table 1.

It is found that $P_{12}^{(1)} \neq P_{21}^{(1)}$ which suggests the defect is not without moment. The relaxation volume is calculated to be 5.32 Ω_{Fe}, which shows a significant addition to the system volume.

2.4.3 Elastic Interactions of Defects

With the multipolar values known for various defects, equation (2.16) may be implemented to calculate interaction energy fields between defects. Plotted in figure 2.4 are the interaction energy contours of (a) an octahedral helium interstitial and (b) an Fe [110] SIA atom, with a $He_{12}V_4$ cluster residing at the center. The helium interstitial interaction energy contours show attraction between the defects at all positions on the (100) plane. This elastic attraction which leads to cluster growth is well known to exist between interstitial helium atoms and HeV clusters, and is confirmed by our elasticity calculations. The SIA on the other hand shows four distinct regions around the cluster. Two regions that indicate a repulsive interaction, and two that show attraction. For a sufficiently strong repulsive interaction near the cluster, one of two phenomena will occur. The SIA will either rotate its orientation to a more energetically favorable configuration, or migrate to one of the attractive regions. Its choice will obviously depend on the energy barriers involved in those processes. In these plots we note that not all positions will be available to the point-defects due to the presence of the host lattice, however we find the trends and energy scales very useful.

We have also conducted calculations between point-defects and an edge dislocation in α-Fe. Using the edge dislocation model given in [68] for an infinite isotropic elastic solid, we have calculated interaction energy contours for multipolar defects. Plotted in figure 2.5 are the interaction energy contours of (a) an octahedral helium interstitial

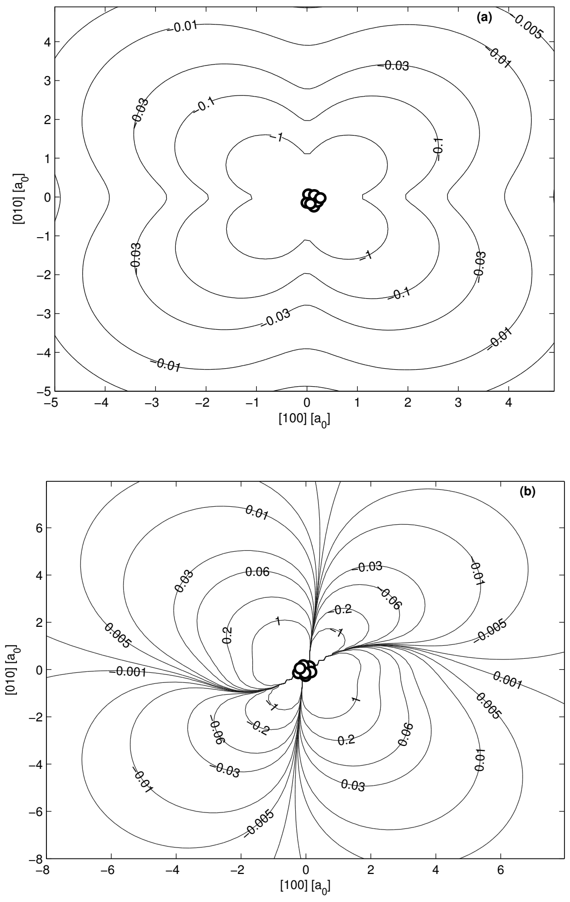

Figure 2.4: Iso-interaction energy contours (in eV) of (a) He octahedral (b) [110] Fe SIA dumbbell, with $He_{12}V_4$ cluster at the origin in α-Fe.

and (b) an Fe [110] SIA atom, with an $a_0/2[111]\{110\}$ edge dislocation. In both plots we see the tendency for the interstitials to be drawn to the dislocation core while on the tensile side of the dislocation (repulsion is seen on the compressive side). We also see some higher-order effects due to the octopole tensor in the contours of both cases within roughly 2 a_0 of the dislocation. These effects fade with distance as the dipole tensor term in equation (2.16) dominates the interaction. The strength and extent of interaction of the Fe interstitial with the dislocation is found to be roughly 2.5 times

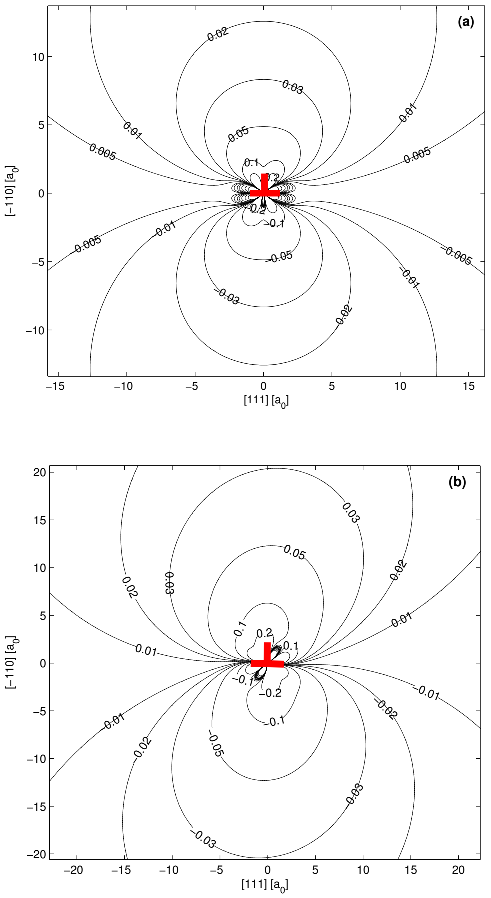

Figure 2.5: Iso-interaction energy contours (in eV) of (a) He octahedral (b) [110] Fe SIA dumbbell, with an $a_0/2[111]110$ edge dislocation in α-Fe.

greater than that of the helium interstitial. These interaction energy plots carry information about possible changes to the stability and migration characteristics of defects in the vicinity of dislocations. For example, defect formation is encouraged on the tensile side of the dislocation, and the preferred migration pathway is towards the dislocation core. The opposite is true on the compressive side. In addition, the stability of point-defect clusters against dissociation will be either endorsed or mitigated, depending upon the defect strength and its position relative to the core.

2.5 Conclusions

In this study, a hybrid method was developed coupling the results of molecular statics calculations with classical isotropic elasticity theory to extract a continuum representation of various defects through the use of elastic force-multipoles. These calculations have provided a means to account for the changes in defect energetics due to local strain environment effects. For the force-multipole representation of defects, we have emphasized the use of higher-order multipole tensors to accurately represent the MS-predicted lattice response of many defects. These include interstitial and substitutional defects, which are typically only modeled with dipole moment. In these cases we found specific importance of the octopole moment ($P^{(3)}$), in enhancing the complexity of the lattice response to match the MS calculations, and overcome the dipole moment's predicted $1/r$ decay near the defect core. This is illustrated in detail for the case of substitutional He. While in most cases atomistic calculations of defect displacements show anisotropies and discrete lattice phenomena, we find the isotropic elastic Green's function to provide very accurate material response, provided higher-order moments describing the defect are implemented.

The additional contribution to the formation energy of a defect in a strained lattice was found to have two equal interpretations according to equations 2.18 and 2.19. Using these interpretations we have presented a closed-form solution for the formation volume tensor in terms of the defect's dipole moment and material constants. Relaxation volumes and formation volume tensors are calculated and presented for selected radiation-induced defects in α-Fe. We have also performed calculations of the interaction energies between multipolar defects, and with an edge dislocation in iron. Our solutions have quantified the spatial extent of interactions as well as directional dependence on migration characteristics. One limitation of the method presented here is the inability to account for internal reorganization of defect clusters to more favorable configurations in strain fields. This can be solved by calculation of the multipole moments of defects in various orientations, and using the appropriate configuration based on which gives the lowest energy for the current spatial position. The tendency for defects to be attracted to the dislocation core while on the tensile side of the dislocation (and repelled on the compressive side) is confirmed by our calculations, and the strength is quantified. The method we describe and its outcomes will allow for more accurate models of defect diffusion and interaction within the radiation damage environment, where long- and short-range elastic interactions govern the accumulation and evolution of defects in the material.

Chapter 3

Effect of Anisotropic Point Defect Diffusion on Swelling in Irradiated Metals: The Dislocation Bias

Swelling in metals exposed to neutron irradiation has long been known to be enhanced by the preferential absorption of interstitials rather than vacancies, by dislocations. While the absorption of interstitials will lead to dislocation climb and creep processes, excess vacancies aggregate to form voids over time, leading to excessive swelling in nuclear materials. A common measure of this preference for interstitials is called the dislocation bias factor and is computed from the ratio of the capture efficiency of interstitials to that of vacancies, by dislocations.

In this chapter, we begin by developing a combined finite-element method (FEM) rate-theory (RT) approach to calculate dislocation bias factors in four model bcc (iron, tungsten) and fcc materials (copper, nickel) using isotropic elasticity theory. The flux of point-defects to the dislocation core in the model results from the drift term in the diffusion equation. This drift term is a function of the spatially-dependent interaction energy between the point-defect and the dislocation which we developed in the previous chapter. One major advantage of this model is the ability to resolve the complex and spatially-dependent diffusion pathways of point defects near the dislocation core.

It has also been long established that bias factors calculated through analytical and numerical means have been known to be approximately an order of magnitude larger than those expected by empirical swelling data. While this discrepancy has been justified by some in the past, it has remained an issue of debate among many. A major issue that has not been explored, however, is the effect of the numerous assumptions and approximations in previous studies. To move deeper into the problem, we explore the effect of three major assumptions of past studies. First, we extend our model to include anisotropic elasticity in the strain field calculations of both the point-defects and dislocations in our calculations. This relieves the assumption that self-interstitial atoms (SIAs) are centers of dilatation in isotropic media. Secondly, since SIAs have energetically-preferred orientations in dislocation stress fields, we use a spatially dependent elastic dipole tensor that accounts for these preferred orientations. Lastly, since SIAs are known to undergo fast one-dimensional (1-D) migration in the Burgers direction in the vicinity of dislocations, we specify a fraction of SIAs to migrate one-dimensionally using a modified SIA diffusion tensor. These additional attributes are implemented into our model to calculate dislocation bias factors in body-centered cubic iron and face-centered cubic copper.

3.1 Introduction and Brief History of the Problem

The internal production of radiation-induced point defects such as self-interstitial atoms (SIAs) and vacancies leads to severe material degradation over time, including swelling, enhanced creep and low-temperature embrittlement. Void swelling [69], in particular is greatly enhanced by the preferential absorption of interstitials rather than vacancies by dislocations. While the absorption of interstitials leads to dislocation climb, excess vacancies form voids over time, becoming sites for gas bubbles and further enhancing swelling in the material. A common measure of this preference for interstitials is called the dislocation bias factor and is computed from the ratio of capture efficiencies of dislocations to interstitials and vacancies. These parameters are of utmost importance, specifically in radiation damage rate-theory (RT) codes simulating void swelling and radiation-creep.

Numerical and analytical calculations for the dislocation bias have been developed by many authors in the past. Ham [70] gave an exact solution to the steady-state diffusion equation near screw and edge dislocations with point-defects modeled as centers of dilatation. Results using Ham's solution for several materials are given in a recent paper by Wolfer [71]. Wolfer and Ashkin [72] developed a perturbation method to extend Ham's work to include the modulus interaction and externally applied strains. While these studies and others have shed some light on the physics of point-defect diffusion in dislocation stress fields, there has for some time been a large discrepancy between predicted swelling rates from bias calculations and those observed experimentally. Specifically, theoretically obtained bias factors have been estimated to be approximately an order of magnitude larger than those expected empirically. The production bias model [73] was used to explain the discrepancy by arguing that SIAs form clusters at higher rates than vacancies, leading to excess vacancy production, and therefore requiring a much larger bias to achieve experimental swelling rates. This argument, however, is only valid under the assumption that the SIA clusters remain sessile, which is not in agreement with numerous molecular dynamics (MD) studies showing the rapid 1-D migration of SIA clusters. Wolfer [71] has accepted the theoretical values, noting that after intra-cascade recombination the available migrating defects are only 10-20% of the displacements produced, requiring a larger bias.

At the present time there is no consensus regarding the discrepancy in bias values. We note however, that before any conclusions can be drawn, every avenue must be explored and the most accurate models must be developed. The past studies have been accompanied by models that are less than rigorous, leaving the validity of the obtained values in question. In the past, SIAs have been modeled as centers of dilatation migrating in three dimensions (3-D) interacting with straight dislocations in isotropic media. These are rather problematic assumptions, especially in iron and copper, for several reasons:

1. SIAs cannot be considered centers of dilatation, as they have both size and shape characteristics.
2. The energetically preferred orientations of SIAs must also be accounted for as they will govern migration pathways near dislocations.
3. The assumption of isotropy in the dislocation displacement field cannot be assumed valid, especially in iron and copper with anisotropy ratios of 2.36 and 3.21, respectively.
4. In iron, and to a lesser extent, copper, SIAs are known to undergo 1-D motion along the Burgers direction in dislocation stress fields.

In this study, we examine the effects of each of the issues raised above. A method is developed to calculate the dislocation bias in iron and copper using a finite-element method (FEM) technique, solving Fick's first law in both time and two-dimensional (2-D) space. Using an atomistically derived continuum representation of point defects, a more rigorous formulation of the interaction energies is used to describe the anisotropic diffusion in the vicinity of a straight edge dislocation. SIAs and vacancies are represented by the elastic dipole tensor, which is computed using anisotropic elasticity theory. The method accounts for the orientation and reorientation of SIAs in the dislocation stress field. The elastic field of the dislocation is also computed using anisotropic elasticity theory. Lastly, the effect of 1-D migration is implemented and examined.

3.2 Point Defect Diffusion in Strain Fields

In the vicinity of a defect with an associated strain field, the flux of a diffusing species α is given by Fick's first law as

$$\vec{j}_\alpha = -\vec{\nabla}(D_\alpha C_\alpha) - \beta D_\alpha C_\alpha \vec{\nabla} E_{int} \tag{3.1}$$

where D_α and C_α are the diffusion coefficient and concentration of species α, respectively, $\beta = (kT)^{-1}$, where k and T take their usual meanings, and E_{int} is the elastic interaction energy of the point defect with the strain field. The first term on the right-hand side of the equation represents the diffusive flux term driven by gradients in the concentration, while the second term, called the 'drift' term gives an additional component driven by the gradient in the elastic interaction. By applying the continuity equation to (3.1), we obtain the rate equation for the concentration as

$$\frac{\partial C_\alpha}{\partial t} + \vec{\nabla} \cdot \vec{j}_\alpha = P - L, \tag{3.2}$$

where P represents production terms for defect α (Frenkel-pair production rate) and L represents loss terms (recombination, absorption at sinks, etc). In RT studies utilizing the mean-field assumption, rate equations for each of the species are constructed and solved simultaneously to calculate the time evolution of the defect concentrations. The term 'mean-field' refers to an effective homogeneous medium where extended defects take on a continuous rather than discrete distribution. In the absence of production and loss terms, and taking the diffusion coefficient to be constant, (3.2) can be expressed as

$$\frac{\partial C_\alpha}{\partial t} = D_\alpha \nabla^2 C_\alpha + \beta D_\alpha \vec{\nabla} \cdot \left[C_\alpha \vec{\nabla} E_{int} \right]. \tag{3.3}$$

Upon solving the diffusion equation with the above expressions, the capture efficiencies of interstitials and vacancies by the dislocation can be calculated. This is accomplished by a line integration of the inner product of flux (obtained from (3.1)) and the unit normal along the capture radius. The capture radius defines the approximate distance from the core at which the drift force due to the interaction energy matches the thermal motion of the defect. Using a lattice-based description of point-defect diffusion, Dederichs and Schroeder [74] showed that anisotropy in the saddle-point configuration is an effect that will alter the migration energy, and consequently the diffusion coefficient of a migrating point-defect. In a study by Skinner and Woo [75], these effects were taken into account and were found to have a small impact on their calculations of dislocation sink strengths. Here, we bypass this issue altogether by implementing effective capture radii for each species. The capture radius of the species defines the zone around the dislocation core in which we can assume all defects of that species are absorbed by the dislocation. It is within this region that the saddle-point anisotropies will have a non-negligible effect, and outside of which we can work under the assumption that the diffusion coefficient for migrating species does not vary in space. The capture radius, $\bar{R}_\alpha$, of a species is defined such that the expression,

$$\| \beta \nabla E_{int} \|_{r=\bar{R}_\alpha} = \frac{1}{b}, \tag{3.4}$$

is satisfied [76], where b is the Burgers vector magnitude. It is important to note that the capture radius is a function of temperature, material properties and the defect's dipole tensor, which we will define in the following subsection. For a species α, the capture efficiency, Z, can then be expressed as

$$Z_\alpha = \frac{\oint_{\bar{R}_\alpha} (\vec{j_\alpha^\perp} \cdot \widehat{n_c}) ds}{\oint_{\bar{R}_\alpha} (\vec{j_\alpha^0} \cdot \widehat{n_c}) ds}, \tag{3.5}$$

where $\widehat{n_c}$ is the unit normal along the circle defined by the capture radius and ds is the corresponding infinitesimal line segment. Here, the numerator represents the line integration in the presence of the dislocation stress field and the denominator without the stress field ($E_{int} = 0$). Essentially, the capture efficiency is a measure of the effect of the drift term in the diffusion equation. Finally, the dislocation bias factor, B, can be defined as

$$B = \frac{Z_i - Z_v}{Z_v}. \tag{3.6}$$

3.3 Solution Methodology

In our simulations we use a 2-D finite element approach to calculate capture efficiencies and bias factors in iron and copper. In all cases, a straight edge dislocation was introduced in the center of a cylinder of radius $R = (\pi\rho_\perp)^{-\frac{1}{2}}$, where $\rho_\perp$ is the dislocation density, taken as 10^8 cm^{-2} in most calculations. The dislocations were type $a_0/2 < 110 > \{111\}$ for fcc and $a_0/2 < 111 > \{110\}$ for bcc metals. For both cases, the x axis was the Burgers direction ([110],[111]) and the y axes were [-111] and [-110], for fcc and bcc, respectively. A core radius ($r_c = a_0/2$) was defined around the dislocation core, where the concentrations for both species were maintained at zero. Next, calculations of the capture radii for both species were undertaken and implemented in the simulation domain. Average concentrations were specified on the outer boundary, $r = R$, obtained through a separate mean-field RT calculation. To accomplish this, we used an approach that simulates radiation damage conditions through coupled rate equations for the SIA and vacancy concentration rates. For interstitial and vacancy concentration rates, the equations were taken as

$$\frac{\partial \bar{C}_i}{\partial t} = P - \eta \bar{C}_i \bar{C}_v - Z_i D_i \bar{C}_i \rho_\perp \tag{3.7}$$

and

$$\frac{\partial \bar{C}_v}{\partial t} = P - \eta \bar{C}_i \bar{C}_v - Z_v D_v \bar{C}_v \rho_\perp, \tag{3.8}$$

respectively. Here, P is the Frenkel-pair production rate and to account for clustering is taken as 15% of the damage dose rate (3×10^{-4} dpa/s), η is the interstitial-vacancy recombination rate, and Z is the capture efficiency. While the ultimate goal is to calculate these capture efficiencies to obtain the bias factor, we initially assumed an expected value (1.20 (iron) and 1.30 (copper) for Z_i, and 1.0 for Z_v for both materials) to give initial self-consistent solutions. Equations (3.7) and (3.8) were then simultaneously solved to obtain the steady-state concentrations in the irradiated configuration. These concentrations were then specified on the boundary at R in our subsequent calculations of the bias factor. Specifying initial concentrations within the domain that transition linearly from $C = \bar{C}$ at $r = R$ to $C = 0$ at $r = r_c$, equations (3.1) and (3.3) for both species were solved simultaneously until steady-state was reached. The line integrals in (3.5) were then performed along the capture radii and the capture efficiencies were computed.

3.3.1 Elastic Representation of Point Defects and their Interactions

The interaction energy term in (3.3) represents the elastic interaction between the diffusing species and a single edge dislocation. To calculate this interaction, we use the multipole method developed in the previous chapter, which is calculated from results of molecular statics calculations using interatomic potentials [77]. To first order, the k^{th} component of the continuum displacement field due to a point defect can be calculated in terms of the Green's tensor function, $G(\vec{r})$, and the defect's dipole tensor, $P^{(1)}$, as

$$u_k(\vec{r}) = -G_{kj,i}(\vec{r})P^{(1)}_{ij}, \tag{3.9}$$

where repeated indices imply summation. In the case of isotropic elasticity, the Green's function in an infinite medium takes the form of (2.23), presented in the previous chapter. In a general anisotropic medium, the expression does not have a closed form expression and requires quadrature integration. Using a Fourier transform method, the Green's function can be expressed as

$$G_{ij}(\vec{r}) = \frac{1}{8\pi^2 r}\oint_{c_k} \frac{N_{ij}(\vec{k})}{D(\vec{k})} d\phi \tag{3.10}$$

where $N_{ij}(\vec{k})$ and $D(\vec{k})$ are the adjoint matrix and determinant of K_{ij}, where $K_{ij} = C_{ikjl}k_l k_k$ and C_{ikjl} is the stiffness tensor, ϕ is an angle on the plane perpendicular to $\vec{r}$, and the integration is taken over the unit circle, c_k, where $|\vec{k}| = 1$ on the plane. A detailed description for obtaining the derivative of the Green's function can be found in [78]. Implementing the Green's function derivative and displacements from molecular statics calculations, we constructed a linear least squares solution from (3.9) to solve for the components of the dipole tensor. The interatomic potentials used in the molecular statics calculations were those of Ackland et al. [79] and Mishin et al. [80], for iron and copper, respectively. Table 3.1 shows computed values of the relaxation volumes, V^r and dipole tensor obtained from our molecular statics calculations using both isotropic and anisotropic elasticity theory.

In the strain field of an edge dislocation, the elastic interaction energy of a point-defect can be expressed as

	Defect	E^m [eV]	$\bar{R}_{cap}$	Symm.	V^r	$P_{11}^{(1)}$	$P_{22}^{(1)}$	$P_{33}^{(1)}$	$P_{12}^{(1)}$
Fe	[110] SIA	0.34 [6]	3.02	Iso.	1.46	18.25	18.25	18.43	7.54
				Anis.	0.91	10.461	10.461	13.342	7.15
	Vacancy	0.67 [6]	1.01	Iso.	-0.11	-1.40	-1.40	-1.40	0
				Anis.	-0.33	-4.093	-4.093	-4.093	0
Cu	[100] SIA	0.079 [81]	3.04	Iso.	0.79	10.822	6.747	6.747	0
				Anis.	1.052	13.861	9.325	9.325	0
	Vacancy	0.72 [82]	0.75	Iso.	-0.133	-1.33	-1.33	-1.33	0
				Anis.	-0.202	-2.076	-2.076	-2.076	0

Table 3.1: Properties of interstitials and vacancies used in the computations. Relaxation volumes are given in atomic volumes, capture radii in lattice parameters and dipole tensor components are in eV. In each case, $P_{23}^{(1)} = P_{13}^{(1)} = 0$.

$$E_{int}(\vec{r}) = -P_{ij}^{(1)} u_{j,i}^{\perp}(\vec{r}). \tag{3.11}$$

where $u_{j,i}^{\perp}(\vec{r})$ is the displacement gradient tensor of the dislocation. This expression for the interaction energy has in the past been accompanied by a modulus interaction term which accounts for the effect of the strain field on the dipole tensor itself [83]. In the study of dislocation bias factors by Wolfer [71] it was found that the added effect is only important very near the dislocation core. We neglect the modulus interaction here due to its inherently small effect, especially with our use of capture radii. For an infinite isotropic continuum, we obtained the displacement gradient tensor of an infinitely long edge dislocation by taking spatial derivatives of the displacement fields given by Hirth and Lothe [68] as

$$u_1(\vec{r}) = \frac{b}{2\pi}\left[\tan^{-1}\frac{x_2}{x_1} + \frac{x_1 x_2}{2(1-\nu)(x_1^2+x_2^2)}\right] \tag{3.12}$$

$$u_2(\vec{r}) = -\frac{b}{2\pi}\left[\frac{1-2\nu}{4(1-\nu)}\ln(x_1^2+x_2^2) + \frac{x_1^2-x_2^2}{4(1-\nu)(x_1^2+x_2^2)}\right], \tag{3.13}$$

where ν represents the Poisson's ratio of the material.

3.4 Results via the Isotropic Approach

Table 3.2 shows computed values of the relaxation volumes and dipole tensor obtained from our molecular statics calculations.

		E^m[eV]	$\bar{R}_{cap}[a]$	V^r	$P_{11}^{(1)}$	$P_{22}^{(1)}$	$P_{33}^{(1)}$	$P_{23}^{(1)}$	$P_{13}^{(1)}$	$P_{12}^{(1)}$
Cu	I	0.079 [81]	3.04	0.81	10.71	10.71	6.40	0.914	-0.914	3.40
	V	0.72 [82]	0.75	-0.13	-1.33	-1.33	-1.33	0	0	0
Ni	I	0.16 [84]	2.60	1.18	15.73	15.73	12.23	1.75	-1.75	1.75
	V	1.30 [24]	0.82	-0.10	-1.24	-1.24	-1.24	0	0	0
Fe	I	0.34 [6]	3.02	1.46	18.25	18.25	18.43	0	0	-7.54
	V	0.67 [6]	1.01	-0.11	-1.40	-1.40	-1.40	0	0	0
W	I	0.05 [85]	5.01	1.01	31.20	31.20	31.20	-16.14	16.14	-16.14
	V	1.78 [86]	1.10	-0.11	-3.41	-3.41	-3.41	0	0	0

Table 3.2: Calculated properties of self-interstitials (I) and vacancies (V) used in the computations. Relaxation volumes are given in atomic volumes and dipole tensor components are given in eV.

Using the values for the dipole tensor of defects we can compute the interaction energies with the dislocation according to (3.11). In Fig. 3.1 we have plotted the computed interaction energies of interstitials versus polar angle around the dislocation.

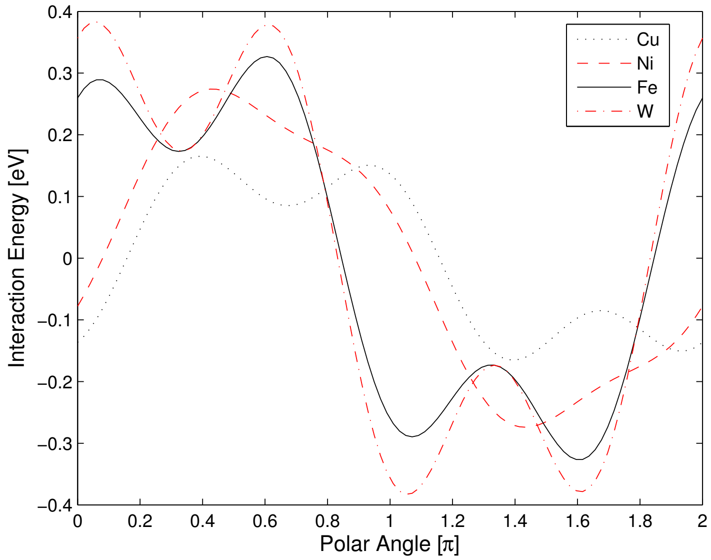

Figure 3.1: (Color online) Interstitial interaction energy versus polar angle around the dislocation core evaluated at the calculated capture radii.

In all cases we see the expected general sinusoidal behavior, oscillating from repulsion on the compressive side of the dislocation to attraction on tensile side. However, what we also see here that is not seen in past studies [70, 71] is the pronounced shape effect of the interstitials, leading to significant deviations from the traditional sinusoidal behavior, due to off-diagonal terms in the dipole tensor. We note again that this behavior cannot be reproduced with interaction energies that rely solely on the relaxation volume and bulk modulus. This shape effect will lead to deviations in the diffusion pathways and provide different results compared to simpler models. In Fig. 3.2 we see capture efficiencies plotted versus temperature in the temperature range of 0.30 to 0.75 T_m for the fcc (a) and bcc (b) materials.

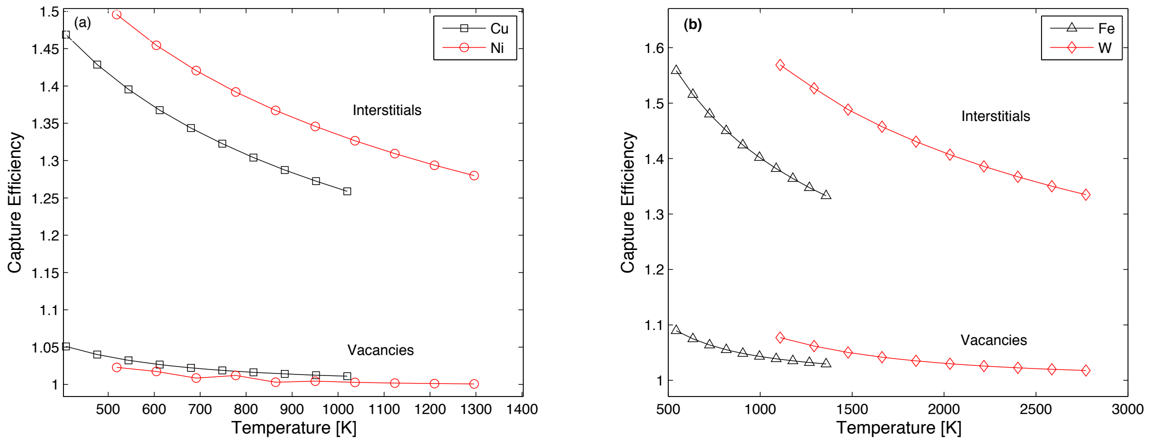

Figure 3.2: (Color online) Capture efficiencies versus temperature using a range of 0.30-0.75 T_m for (a) fcc copper and nickel, and (b) bcc iron and tungsten. Results are obtained using a dislocation density of 10^8 cm^{-2} and damage rate (K) of 3×10^{-4} dpa/s.

The upper two curves represent values of Z_i while the lower two curves represent Z_v. The observed decrease in capture efficiency with increase in temperature can be attributed to the increased mobility of the defects. At lower temperatures the drift term in (3.1) will have a more pronounced effect on the diffusion pathways leading to a greater flux of defects to the dislocation core. At higher temperatures, the effect of the drift term is lessened by the increased mobility, allowing a larger percentage of defects to be captured due to thermal effects. Essentially, at higher temperatures, the ratio of fluxes that define the capture efficiency in (3.5) is much less due to the suppression of the drift term made possible by the increased mobilities. In all of the materials studied, we find a much greater effect of temperature on interstitial capture efficiencies than on those of vacancies. We see a roughly 14% percent decrease in Z_i and a 3-6% decrease in Z_v across the temperature range. This is due to the much weaker interaction of the vacancy with the dislocation stress field coupled with much larger migration energies.

Table 3.3 gives the bias factors for all four materials evaluated at half the melting temperatures with a damage rate of 3 $\times 10^{-4}$ dpa/s and dislocation density of 10^8 cm^{-2}.

	Defect	$\bar{C}$ [m^{-3}]	$J^{\perp}$ [m^{2}s^{-1}]	J^0 [m^{2}s^{-1}]	Z	B
Cu	Interstitial	6.411×10^{16}	1.34×10^{-18}	1.00×10^{-18}	1.344	0.314
	Vacancy	5.366×10^{22}	1.03×10^{-18}	1.01×10^{-18}	1.022	
Ni	Interstitial	1.162×10^{16}	9.73×10^{-20}	7.11×10^{-20}	1.367	0.363
	Vacancy	7.707×10^{23}	9.01×10^{-20}	8.98×10^{-20}	1.003	
Fe	Interstitial	9.211×10^{18}	6.17×10^{-18}	4.33×10^{-18}	1.424	0.358
	Vacancy	7.426×10^{21}	2.65×10^{-18}	2.53×10^{-18}	1.048	
W	Interstitial	3.304×10^{16}	2.08×10^{-18}	1.46×10^{-18}	1.431	0.382
	Vacancy	2.051×10^{22}	1.45×10^{-18}	1.41×10^{-18}	1.035	

Table 3.3: Sample results at half the melting point with a dislocation density of 10^8 cm^{-2} and damage rate (K) of 3×10^{-4} dpa/s. $J^{\perp}$ and J^0 represent the evaluation of integral in the numerator and denominator of (3.5), respectively.

A direct comparison of the calculated bias factors with previous works reveals very good agreement for the fcc materials. For copper, our calculated value of 0.314 is very close to the value of 0.291 obtained by Wolfer [71] using Ham's solution. It also compares well to the value of ∼0.3 obtained by Skinner and Woo [75] (at 500 K). We also see good agreement in the case of nickel where we calculate a bias of 0.363 compared to the values of 0.344 [71] and 0.30-0.40 from [87].

For the bcc materials, however, we see a very large discrepancy with our calculations and those in the study of Wolfer. In iron, for example, we obtain a bias of 0.358 which is nearly 2.5 times greater than Wolfer's value of 0.144. Similarly, for tungsten we obtain a bias of 0.382 compared to 0.178. Comparing to the values of Skinner and Woo [75], however, we see much better agreement in the case of iron. At 500 K they obtain a Z_i and Z_v of approximately 1.35 and 0.9 which gives a bias of $\sim$0.5 (according to our definition of bias in (3.6)). Extrapolating to 0.5 T_m ($\sim$905 K) we see a value of $\sim$0.4, which is much closer to our calculated value. One issue that may explain the discrepancy with Wolfer's values are the relaxation volumes used in the size interaction. From our dipole tensor values we calculate relaxation volumes ($V^r = \mathrm{tr} P^{(1)}/3\kappa$) in iron of 1.46 and -0.11 atomic volumes, for interstitials and vacancies, respectively. We note these values agree very well with other recent works using molecular statics calculations [88]. The values used in Wolfer's study to develop the defect size interaction were much different (0.91 and -0.32). The 40% smaller interstitial relaxation volume would lead to a much weaker interaction with the dislocation. Additionally, the 300% larger vacancy relaxation volume would lead to a much larger flux of vacancies into the core. The combined effect would serve to both drastically decrease Z_i and increase Z_v, leading to a much smaller bias, as seen in those results.

Fig. 3.3 is a plot of bias factor versus dislocation density ($\rho_\perp$) for copper. The values are obtained at half the melting point of copper (680 K) and with a damage rate of 3×10^{-4} dpa/s.

The dislocation densities here represent a range of cylinder radii ranging from $2200a$ to $70a$. In the range of 10^8 and 10^10 we see a 56% increase in the bias which agrees well with the values obtained in [75], where a 45% increase is observed over the same range. When $\rho_\perp$ becomes large, the concentration gradients also become large leading to higher concentrations closer to the core, which allows an increased

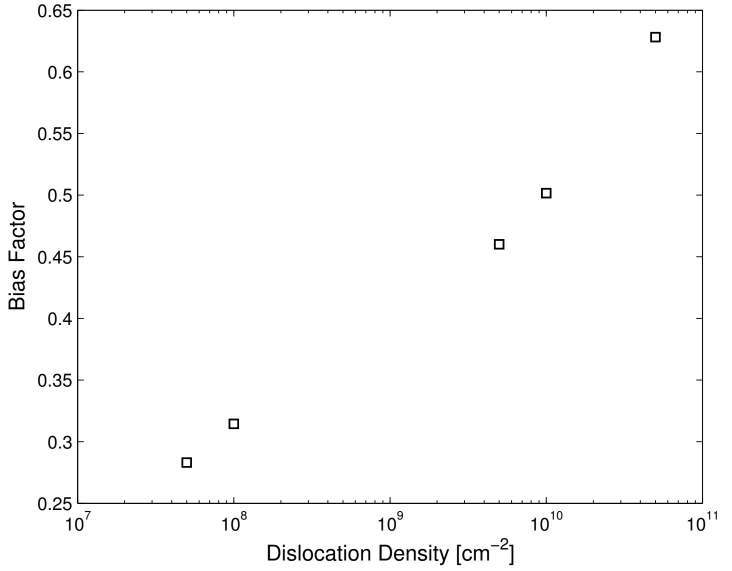

Figure 3.3: Dislocation Bias Factor versus Dislocation Density for copper. Results are obtained for a temperature of 0.5 T_m and damage rate (K) of 3×10^{-4} dpa/s.

effect of drift on the flux.

Also investigated in this study was the dependence of the bias factors on damage rate (K). In our studies we find a negligible effect of damage rate on the computed values. While the damage rate has a large impact on the calculated $\bar{C}_\alpha$'s, the effect of the $\bar{C}_\alpha$'s on the flux due to drift is negligible.

3.5 The Enhanced Resolution Approach

Expanding our model to include full anisotropy, preferred SIA orientations and one-dimensional migration mechanisms has provided increased insight into the problem of larger than expected bias factors. In a general anisotropic material, calculation of the displacement gradient tensor at a field point $\vec{r}'$ due to a dislocation requires numerical integration of the Green's function derivative along the dislocation line. From [78], the equation is given as

$$u_{i,j}(\vec{r}) = C_{klmn} b_m \varepsilon_{njh} \oint_L G_{ik,l}(\vec{r} - \vec{r}') dl_h(\vec{r}'), \tag{3.14}$$

where ε_{jnh} is the permutation tensor. To apply (3.14) to our 2-D simulation domain, we ran an optimization scheme to obtain both the minimum required length of line to avoid end effects and the minimum number of integration points along the line. Using a general isotropic stiffness tensor, we found accuracy within a few tenths of a percent of the isotropic dislocation gradient solution when a dislocation line length of $50|\vec{r}|$ is used with 120 integration points along the line, where $|\vec{r}|$ is the distance from the field point to the center of the dislocation line. In our bias calculations using the anisotropic field, the 2-D simulation domain is taken as the plane that bisects the dislocation line.

3.5.1 Orientation of SIAs in Dislocation Stress Fields

The orientations of migrating SIAs are accounted for through the choice of dipole tensors used. The formation energy of an SIA in a dislocation's strain field can be taken as the equilibrium formation energy plus the interaction energy with the dislocation. Therefore, depending on where an SIA is located in reference to the dislocation, some SIA orientations will be more energetically preferred than others. The three-dimensionally migrating SIAs have six possible <110> orientations. When we refer to 3-D SIAs, we refer to SIAs undergoing the translation-rotation mechanism with migration energy 0.34 eV [6]. In Figure 3.4 we have plotted the computed interaction energies of these orientations (in iron) versus polar angle around the dislocation at a radius of 4.3b from the core.

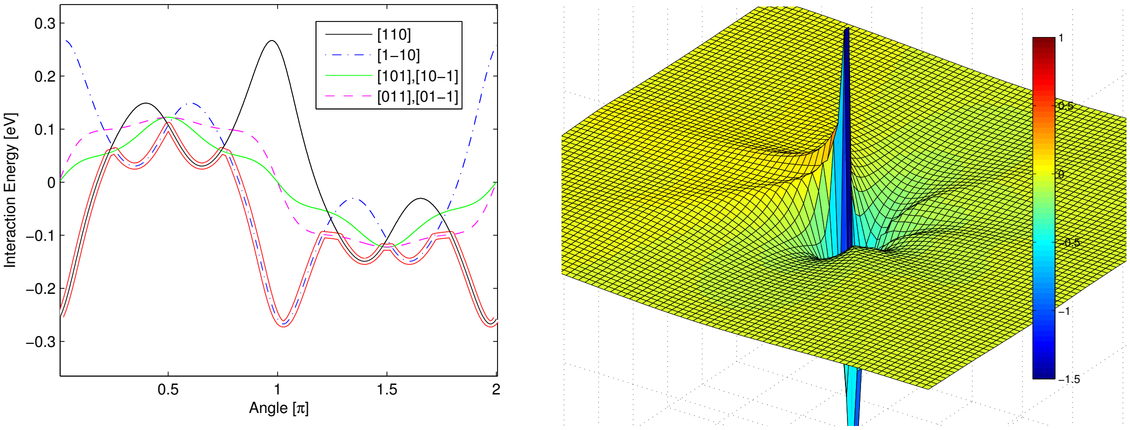

Figure 3.4: Interaction energy vs. polar angle around the dislocation core (left) and minimum energy configuration (MEC) interaction energy surface (in eV), for an SIA in iron (right). The MEC interaction energy line (in red) outlines the configurations that give minimum interaction energies.

The figure was generated using the anisotropic dipole tensors and anisotropic dislocation field. We note that the compressive regime of the dislocation ranges from $[0,\pi]$, while the tensile regime ranges from $[\pi,2\pi]$. From the figure we clearly see each orientation has its own specific behavior around the core. In particular the [110] and [1-10] orientations give vastly different behavior, especially in the regions where the field transitions from tension to compression, or vice versa, are made. Thus, we cannot simply prescribe a single dipole tensor to all SIAs, as has been done in the past, but must choose the most energetically favorable configurations depending on their locations. To do this, we use a scheme to extract the dipole configuration that gives the lowest interaction energy, and thus the lowest formation energy for all space. For the remainder of the article we will refer to calculations using this method as the *minimum energy configuration* (MEC) calculations. In Figure 3.4, the MEC interaction energy curve outlines the curves with minimum energy in red.

3.5.2 One-Dimensional Migration of SIAs in Dislocation Stress Fields in Iron

The effect of the 1-D migration of SIAs is a phenomenon not addressed in bias calculations of the past. In iron, this type of SIA may take one of the four possible <111> crowdion orientations and migrate one-dimensionally along its axis. The migration energy for such an event is taken as 0.024 eV, following a study by Osetsky and co-workers [89]. Using first principles calculations, a previous study found the equilibrium formation energy of the $< 111 >$ SIA to be 0.70 eV larger than that of the $< 110 >$ SIA. In the vicinity of an edge dislocation, however, this formation energy is biased by the interaction, and SIAs have been found to take the crowdion configuration and migrate one-dimensionally [90]. In our simulations of iron, the total outer boundary SIA concentration, $\bar{C}_i$, is divided amongst the 3-D SIAs and the 1-D SIAs, based on the parameter, f_{1D}; the fraction of all SIAs migrating in one-dimension. In these calculations we once again implement the MEC method, choosing the $< 111 >$ configuration that gives the lowest formation energy based on its position. The 1-D diffusion is obtained by implementing the diffusion tensor, D_{ij} into the calculations. In matrix form, (3.1) can be expressed as

$$\begin{Bmatrix} j_1 \\ j_2 \end{Bmatrix} = - \begin{bmatrix} D_{11} & 0 \\ 0 & D_{22} \end{bmatrix} \begin{Bmatrix} C_{,1} \\ C_{,2} \end{Bmatrix} - \beta C \begin{bmatrix} D_{11} & 0 \\ 0 & D_{22} \end{bmatrix} \begin{Bmatrix} E_{,1} \\ E_{,2} \end{Bmatrix} \tag{3.15}$$

where we have taken the coupling coefficients, $D_{12} = D_{21} = 0$. We then estimate D_{11} and D_{22} for each of the four configurations as the projection of the orientation (migration direction) onto the x and y directions of our simulation domain, or $D_{ij} = D_0 d_j \delta_{ij}$, where d is the local orientation and D_0 is the equilibrium diffusion coefficient. For example, rotating the [111] crowdion to the local (simulation) frame of reference, its orientation is [100], and thus it has $D_{11} = D_0$ and $D_{22} = 0$. Thus it migrates one-dimensionally along the Burgers direction. Table 3.4 shows the global and local orientations of the four $< 111 >$ crowdion configurations, their local diffusion tensor components and their calculated dipole tensor components, used in our calculations.

$\vec{d}_{Global}$	$\vec{d}_{Local}$	D_{11}	D_{22}	$P^{(1)}_{i=j}$	$P^{(1)}_{23}$	$P^{(1)}_{13}$	$P^{(1)}_{12}$
[111]	[1 0 0]	D_0	0	10.495	5.496	5.496	5.496
$[\bar{1}11]$	$[\sqrt{\frac{2}{15}}\ \frac{2}{\sqrt{5}}\ \frac{1}{\sqrt{15}}]$	$\sqrt{\frac{2}{15}}D_0$	$\frac{2}{\sqrt{5}}D_0$	10.495	5.496	-5.496	-5.496
$[\bar{1}\bar{1}1]$	$[-\sqrt{\frac{2}{15}}\ \frac{2}{\sqrt{5}}\ -\frac{1}{\sqrt{15}}]$	$-\sqrt{\frac{2}{15}}D_0$	$\frac{2}{\sqrt{5}}D_0$	10.495	-5.496	-5.496	5.496
$[1\bar{1}1]$	$[\frac{1}{3}\ 0\ \frac{\sqrt{8}}{3}]$	$\frac{1}{3}D_0$	0	10.495	-5.496	5.496	-5.496

Table 3.4: Global and local SIA orientations, diffusion coefficients and dipole tensor values (in eV) for the one-dimensionally migrating SIAs in iron. D_0 represents the equilibrium 1-D diffusion coefficient. Computed relaxation volumes (in atomic volumes) for each type are $V^r = 0.839$.

3.5.3 Results & Discussion

In Figure 3.5 we have plotted computed bias factors in iron and copper versus temperature for four scenarios. The temperatures range from 0.4 to 0.7 times the melting point of each. Three of the scenarios use a single dipole tensor in all space ([110] in iron, [100] in copper), while the fourth uses the MEC. In the figure, 'Iso. $P^{(1)}$' and 'Anis. $P^{(1)}$' refer to calculations using the dipole tensors calculated from equation (3.9) using isotropic and anisotropic Green's function derivatives, respectively. 'Iso. $\perp$' and 'Anis. $\perp$' refer to calculations using the dislocation fields obtained from isotropic and anisotropic elasticity theory, respectively.

In the case of copper we see a progressive increase in bias factors through the

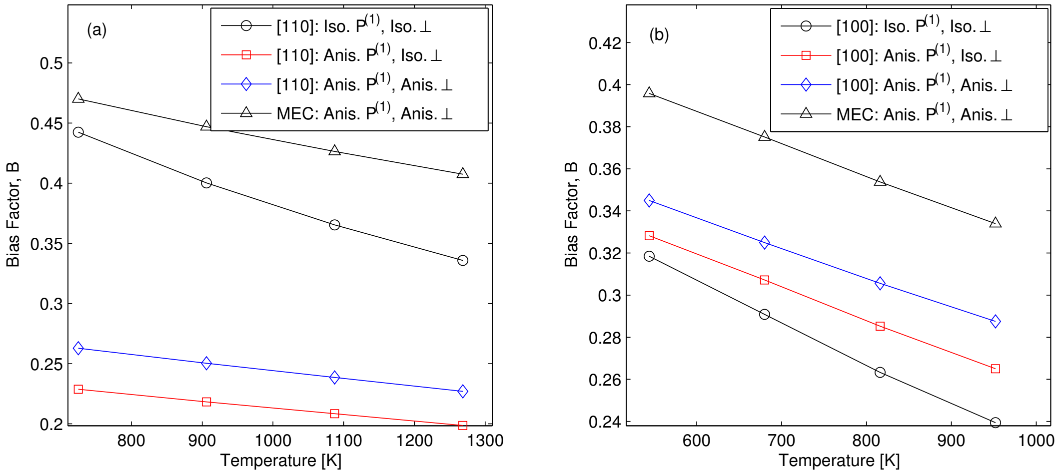

Figure 3.5: Bias factor vs. temperature in iron, (a), and copper, (b). The effects of material symmetry (Iso, Anis) in the defect dipole tensors ($P^{(1)}$) and dislocation fields (⊥) are plotted.

four scenarios. Using fully isotropic calculations we obtain a bias exactly equal to the value obtained by Wolfer [71] at 0.5T$_m$, 0.291. By implementing the anisotropic dipole tensor, this value slightly increases to roughly 0.31. This was to be expected, according to Table 3.1, where an increase in the dipole values is observed in the anisotropic case. Next, implementing the anisotropic dislocation fields from (3.14), the bias increases to 0.33. When the effect of SIA orientation is taken into account (MEC), the largest increase in the bias is observed, to ∼0.38.

In iron, the behavior is altogether different from that of copper. In the isotropic dislocation field, when the [110] isotropic dipole tensor is substituted with the anisotropic tensor, the bias decreases by 45% from 0.40 to 0.22. This is a result of the decrease in dipole strength of the SIA accompanied by an increase in strength of the vacancy. Thus the absorption of SIAs by the dislocation is decreased while the absorption of vacancies is increased, leading to a lower bias. Using the anisotropic dislocation field, we find a 12% increase in the bias factor. Just as in the copper calculations, we see the largest increase in the bias when we account for the SIA orientations (MEC method), giving a value of 0.45 at 0.5T$_m$.

In both materials we see an increase in the bias when the anisotropic dislocation field is used. This is due to a stronger interaction of the SIA with the dislocation in the anisotropic field. To further examine this, in Figure 3.6 we have plotted the components of the interaction energy gradient for a [110] SIA in iron, plotted in a circle of radius $3b$ around the dislocation core. Both the isotropic and anisotropic dislocation field interactions are plotted. The $\nabla Eint_x$ plot represents the interaction energy gradient in the dislocation's Burgers direction, while the $\nabla Eint_y$ plot represents the gradient in the direction perpendicular to $\vec{b}$ (along the extra plane). We see in both components that the gradients in the anisotropic case are generally larger than in the isotropic case, leading to a stronger drift velocity in the calculations. This is more pronounced for the y-component, especially in the regions of [0.8π, 1.2π] and [1.8π,

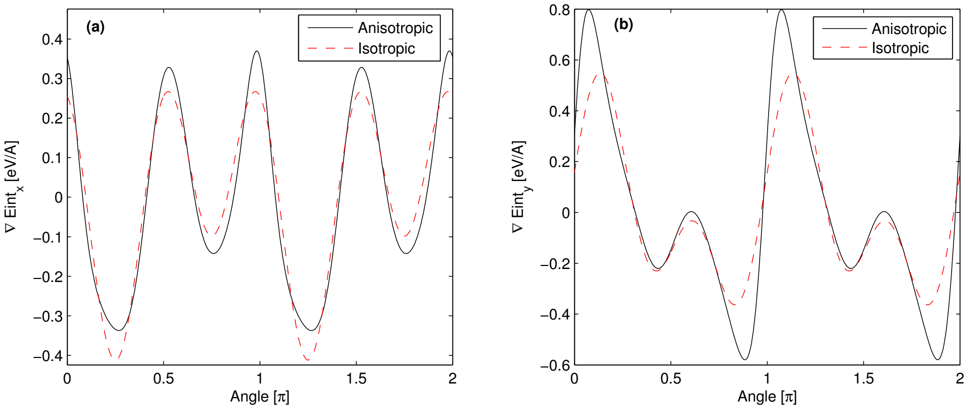

Figure 3.6: X-component (a) and Y-component (b) of the interaction energy gradient vs. polar angle around the dislocation, computed along a circle of radius of $3b$ for a [110] SIA in iron.

0.2π], where a 33% stronger gradient is observed at the peaks.

In Figure 3.7 we have plotted bias factor versus temperature for varying percentages of 1-D migrating SIAs in iron. In the fully anisotropic case at $0.5T_m$ we find a 46% drop in the bias as the SIAs go from fully 3-D to fully 1-D. In the isotropic case the effect of 1-D is more drastic, as the bias drops to the empirically expected range of several percent at roughly 50% 1-D.

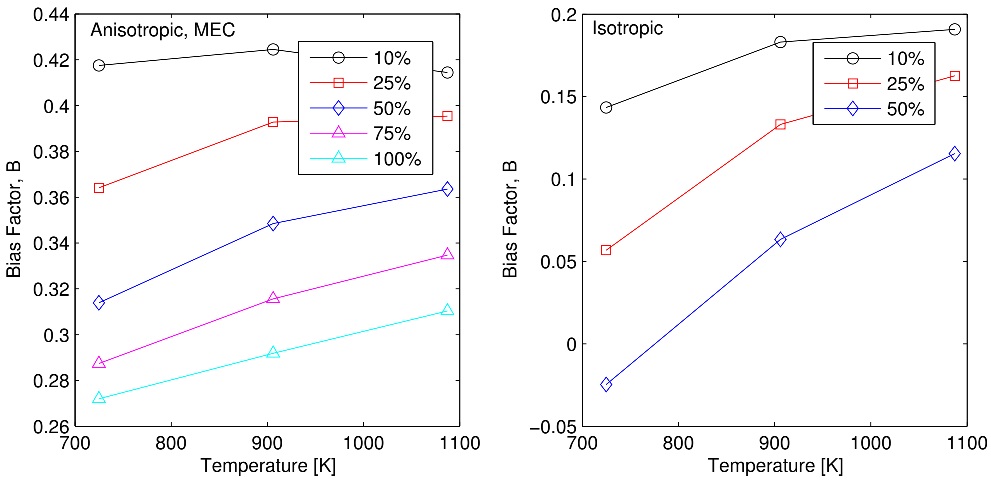

Figure 3.7: Bias factor vs. temperature in iron for the fully anisotropic case (with MECs) (left) and fully isotropic case (without MECs) (right), with varying percentages of one-dimensionally migrating SIAs.

In all cases studied, the largest effect on the bias we see in our calculations is due to the implementation of the MEC method. The effect of this method, versus modeling SIAs as single configurations (dipole tensors), is that at each location the dipole tensor that gives the lowest formation energy is chosen. In Figure 3.4 we see this decreases the repulsive interaction on the compressive side while increasing attraction on the tensile side. In Figure 3.4, the interaction energy surface is also shown around the dislocation core. Ridges and valleys can be seen in the radial directions, corresponding to the specific minimum energy SIA orientations. As interstitials are drawn toward the core they face barriers keeping them from changing their orientation. This effectively reduces their spatial distribution due to Brownian diffusion and enhances their migration to the dislocation, leading to larger bias factors.

Chapter 4

Spatially Resolved Rate Theory of Point Defect Clustering in Stress and Temperature Gradients

In fusion environments, plasma facing components are exposed to very high heat and particle fluxes resulting in extremely large temperature and stress gradients in materials, especially near the surface. Such gradients contribute additional driving forces in the nucleation, growth and diffusion of point defect clusters. Continuous exposure to such environments leads to the migration and coalescence of bubbles and severe surface degradation. Figure 4.1 shows a focused ion beam (FIB) produced cross-section of 16 keV helium-irradiated tungsten, illustrating this point.

In this chapter, we first describe the mathematical foundations of classical nucleation theory, including its extension to irradiated metals. We then review a past mean-field rate-theory model of bubble growth in irradiated metals. Applying our description of point-defect interaction energies in stress fields, we develop a finite element implementation to resolve the average bubble size profile from the exposed surface into the bulk, in plasma facing components under typical stress and temperature gradients. Results are interpreted from the perspective of point defect drift diffusion processes on the bubble size profile. The results are compared to the classical solutions of Nichols and Eshelby, where bubble drift diffusion is known to be orders of magnitude more sensitive to temperature gradients than those of stress.

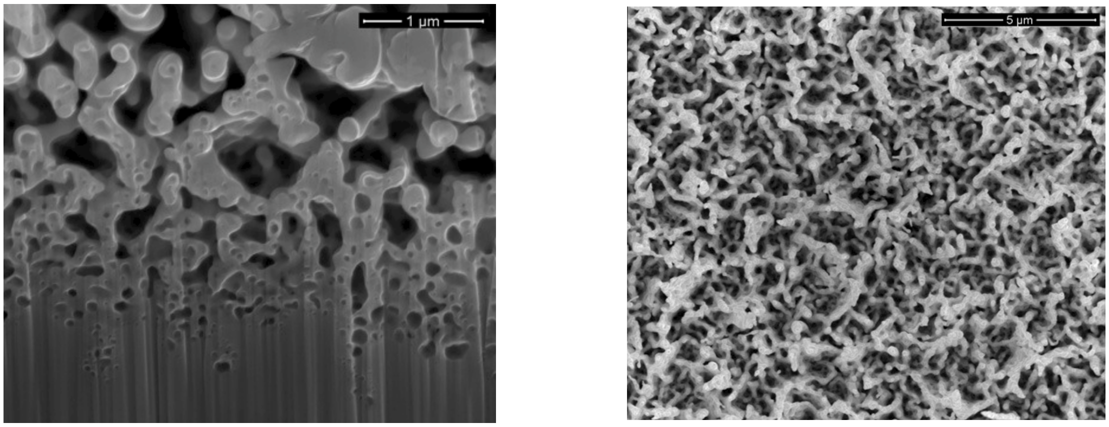

Figure 4.1: FIB cross section of a W sample irradiated by 700 27s long pulses of pure He at 16 keV (left), and SEM of corresponding surface. [4]

4.1 Review of Classical Nucleation Theory

Classical nucleation theory, as developed by Becker and Döring in 1935 [91], is a method to develop a set of equations to model phenomena such as condensation, evaporation and in general, any two-phase system (gas-liquid, crystalline-amorphous, etc). It is especially useful in computations of equilibrium size distributions of phases. In the case of vacancy clustering, assumptions of the theory are as follows:

1. Atomic clusters originate when two atoms come together;
2. Clusters can grow or shrink by the absorption or emission of single vacancies, respectively;
3. Small clusters may dissociate into monomers, however once a critical size is reached, the cluster will grow to a macroscopic size.

If we let $C(m,t)$ represent the number of clusters containing m vacancies at time t per volume, then we can express their rate of change as

$$\frac{\partial C}{\partial t} = \int_1^\infty \{C(m',t)R(m|m') - C(m,t)R(m'|m)\}\mathrm{d}m', \tag{4.1}$$

where $R(m|m')$ is the transition probability rate that a cluster of size m' will grow to size m. We can next define the impingement frequency $\beta_v(m)$ and emission frequency $\alpha_v(m)$ of single vacancies to clusters. These quantities are functions of the vacancy concentration and diffusion coefficient, as well as the cluster surface area, $A(m)$. Under the second assumption above, the transition probabilities can then be expressed in terms of Dirac delta functions, δ, as

$$\begin{aligned} R(m|m') &= \beta_v(m')\delta(m-(m'+1)) + \alpha_v(m'-1)\delta(m-(m'-1)) \\ R(m'|m) &= \beta_v(m)\delta(m'-(m+1)) + \alpha_v(m-1)\delta(m'-(m-1)) \end{aligned} \tag{4.2}$$

Substituting these into (4.1) and evaluating the integral, we obtain

$$\frac{\partial C}{\partial t} = \beta_v(m-1)C(m-1,t) + \alpha_v(m)C(m+1,t) - \beta_v(m)C(m,t) - \alpha_v(m-1)C(m,t). \tag{4.3}$$

At equilibrium, $\partial C/\partial t = 0$, we can invoke the principle of thermodynamic reversibility, i.e., that $R(m \pm 1|m) = R(m|m \pm 1)$. The corresponding concentration is called the *constrained equilibrium function*, C_0. This allows α_v to be solved for as

$$\alpha_v(m+1) = \beta_v(m)\frac{C_0(m)}{C_0(m+1)}, \tag{4.4}$$

which is assumed to be valid in non-equilibrium conditions as well. Plugging the expression for α_v into (4.3) gives

$$\begin{aligned} \frac{\partial C}{\partial t} = \beta_v(m)C_0(m)&\left[\frac{C(m+1,t)}{C_0(m+1)} - \frac{C(m,t)}{C_0(m)}\right] \\ &- \beta_v(m-1)C_0(m-1)\left[\frac{C(m,t)}{C_0(m)} - \frac{C(m-1,t)}{C_0(m-1)}\right]. \end{aligned} \tag{4.5}$$

This is known as the difference differential equation for nucleation. Expanding each of the terms in the brackets in Taylor series' about n, it can be shown that (4.5) can be written as

$$\frac{\partial C}{\partial t} = \frac{\partial}{\partial n}\left[\beta_v(m) C_0(m) \frac{\partial(\frac{C(m)}{C_0(m)})}{\partial n}\right]. \tag{4.6}$$

We note this expression has the form of Fick's second law in a force field with a variable diffusion coefficient. This is consistent with the view that nucleation is random walk process through cluster size phase space. Viewing $\beta_v(m)$ as an effective diffusion coefficient in size space and applying the continuity equation, the cluster nucleation current, $I(m)$ can be taken as

$$I(m) = -\beta_v(m) C_0(m) \frac{\partial(\frac{C(m)}{C_0(m)})}{\partial n}, \tag{4.7}$$

and the continuity equation in an m-dimensional size space can be given as

$$\frac{\partial C}{\partial t} + \vec{\nabla} \cdot \vec{I}(m) = 0. \tag{4.8}$$

Thus we have developed a rate equation for the concentration of m-sized voids.

4.1.1 Extension to Radiation Damage

Following the observations by Cawthorne and Fulton [69] that the formation of voids occurs in metals exposed to fast neutrons, interest in the application of classical nucleation theory to radiation damage grew rapidly in the early 1970s. The first such undertakings were done independently by Katz and Wiedersich [92] and Russell [93] in 1971. These studies extended the classical theory to irradiation cases, where in addition to vacancies, interstitials can also contribute to growth and shrinkage processes. Also, radiation-induced vacancies and interstitials are produced continuously, leading to the supersaturation of their concentrations beyond equilibrium, ultimately changing the size distribution evolution. The Gibb's free energy (GFE) of a system containing a concentration distribution, $N^{eq}(m)$, of clusters of sizes m, can be expressed as

$$G = G_0 + \sum_m N^{eq}(m) g_m - kT \sum_m \ln W_m, \tag{4.9}$$

where G_0 is the free energy of the perfect lattice, g_m is the GFE required to form a void of size m, and the last term is the absolute temperature multiplied by the configurational entropy. We note that g_m is typically estimated as the void formation energy (E_m^f) under the assumption of negligible volume and entropy changes in the formation process. Also, W_m represents the number of possible ways in which a void of size m can be distributed in the lattice, which can be shown to be

$$W_m = \frac{m^{N^{eq}(m)} (\frac{1}{\Omega m})!}{[\frac{1}{\Omega m} - N^{eq}(m)]! [N^{eq}(m)]!}. \tag{4.10}$$

The chemical potential of a void of size m can be defined as the partial derivative of G with respect to the equilibrium concentration of size m voids, or

$$\mu_m = \frac{\partial G}{\partial N^{eq}(m)} = E_m^f + kT \ln \left[\Omega N^{eq}(m) \right]. \tag{4.11}$$

The chemical potential of a single vacancy can therefore be taken as $\mu_v = E_v^f + kT\ln[\Omega C_v]$, where the vacancy formation energy can be substituted from the equilibrium vacancy concentration, given as $C_v^{eq} = \Omega^{-1} \exp(-\frac{E_v^f}{kT})$. The vacancy chemical potential can therefore be expressed as

$$\mu_v = kT \ln \left[\frac{1}{\Omega C_v^{eq}} \right] + kT \ln \left[\Omega C_v \right] = kT \ln S_v. \tag{4.12}$$

where $S_v = C_v / C_v^{eq}$ is the vacancy supersaturation in the lattice. For the vacancies and voids to be in chemical equilibrium, the chemical potential of voids of size m must be equal to m times the chemical potential of an individual vacancy. Therefore, the equilibrium void distribution function can be solved for from (4.11) and (4.12) as

$$N^{eq}(m) = \Omega^{-1}\exp(m\ln S_v - \frac{E_m^f}{kT}). \tag{4.13}$$

Under non-equilibrium conditions, we can define the nucleation current (in the phase space of cluster size) as the rate at which clusters of size m grow to $m+1$. This can be expressed as

$$I = \beta_v(m)N(m) - \alpha_v(m+1)N(m+1) - \beta_i(m+1)N(m+1). \tag{4.14}$$

Here, the emission of interstitials as a void growth process is neglected due to the large formation energy of interstitials. By the condition of thermodynamic reversibility, the rate of capture of vacancies to clusters of size m should equal the rate of emission of vacancies of clusters of size $m+1$, and therefore α_v can be solved for as (4.4), with $C_0(m)$ replaced with $N^{eq}(m)$. Plugging this back into (4.14), we obtain

$$I = -\beta_v(m)h(m)\left[\frac{N(m+1)}{h(m+1)} - \frac{N(m)}{h(m)}\right], \tag{4.15}$$

where the function $h(m)$ is defined in

$$\frac{h(m)}{h(m+1)} = \frac{N^{eq}(m)}{N^{eq}(m+1)} + \frac{\beta_i}{\beta_v}. \tag{4.16}$$

The ratio of impingement frequencies β_i/β_v is referred to as the arrival-rate ratio and plays a large role in determining the critical void size, m_c, which occurs at the minimum of $h(m)$. Figure 4.2 shows a plot of the constrained distribution function, h(m), versus cluster size for a range of arrival-rate ratios. This figure illustrates the fact that nucleation theory is heavily dependent on the parameters used. This is a major disadvantage since in most cases, many parameters are not known to a high degree of accuracy.

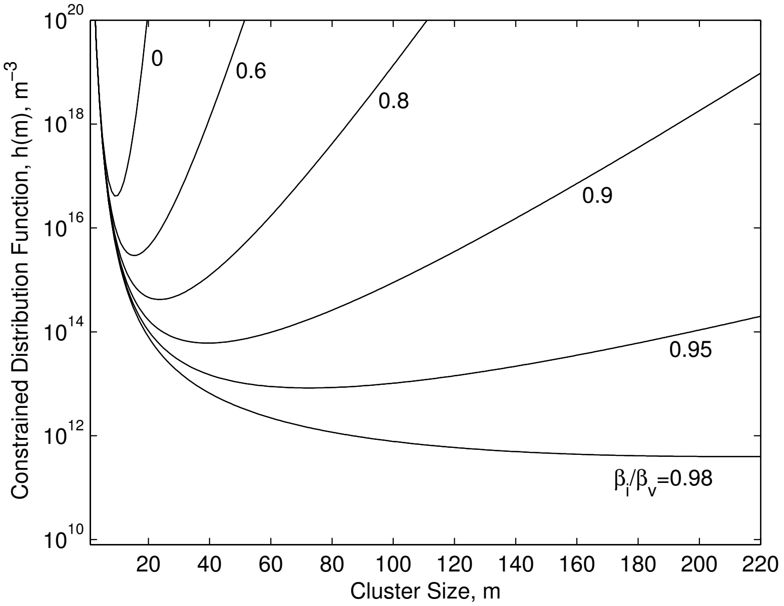

Figure 4.2: Constrained distribution function, h(m), versus cluster size, m.

Approximating the difference in the brackets of (4.15) as the differential $d(N/h)/dm$, the resulting differential equation can be solved under the boundary conditions that $N/h \rightarrow 1$ and 0 as m goes to 1 and ∞, respectively. The nucleation current can then be calculated as

$$I = \left[\frac{1}{2\pi}\left(\frac{\mathrm{d}^2\mathrm{ln}h}{\mathrm{dm}^2}\right)_{m_c}\right]^{1/2}\beta_v(m_c)h(m_c). \tag{4.17}$$

where the first term on the right hand side is called the Zeldovich factor, and corrects for the fact that some fraction of clusters which have grown past the critical size will still shrink to smaller sizes.

The extension of the theory to include the effects of gas atoms resulting from transmutation reactions was also accomplished by Katz and Wiedersich [94] and Russell [95]. The derivation of these heterogeneous nucleation models follows the same structure as the preceding model, under the assumption that gas atoms are static nucleation sites for voids. The number of clusters with j gas atoms per unit volume is taken as M_j, making the total concentration of gas atoms, M, equal to $\sum_{j=1} jM_j$. The Gibb's free energy expression takes the modified form:

$$G = G_0 + \sum_j \sum_m \left[N_j^{eq}(m) g_{mj} - kT \sum_m \ln W_{mj} \right], \tag{4.18}$$

where N_j^{eq} is the equilibrium distribution of gas-vacancy clusters per unit volume containing m vacancies and j gas atoms. The configurational term can be calculated as

$$W_{mj} = \frac{M_j!}{[M_j - N_j^{eq}(m)]![N_j^{eq}(m)]!}. \tag{4.19}$$

The presence of gas atoms in voids leads to an internal pressure that aids in stabilizing voids against dissociation. This has the effect of leading to smaller values of the critical size, as the pressure reduces the effect of surface tension against collapse. Thus, the reversible work of formation g_{mj} will contain a positive contribution due to surface tension and a negative contribution due to the gas pressure. Assuming the gas atoms in the matrix are at an effective pressure p^{eq}, corresponding to the temperature and their concentration, the reversible work of adding gas atoms to a cluster at pressure p is $jkT \ln(p^{eq}/p)$. Assuming the ideal gas law holds, the pressure can be determined from $pV = jkT$, where $V = m\Omega$. Estimates for p^{eq} can be obtained from statistical mechanics models. The reversible work of cluster formation can then be expressed as

$$g_{mj} = 4\pi R^2 \gamma - jkT \ln \left(\frac{p_{eq}}{p} \right), \tag{4.20}$$

where γ is the surface energy and the cluster radius R can be taken as $(3m\Omega/4\pi)^{1/3}$. For chemical equilibrium to be satisfied, the condition $m\mu_v = \mu_{mj}$ must be satisfied, where the chemical potential of gas-filled clusters can be taken as

$$\mu_{mj} = \frac{\partial G}{\partial N_j^{eq}(m)} = g_{mj} + kT\ln\left[\frac{N_j^{eq}(m)}{M_j}\right]. \tag{4.21}$$

Using equation (4.12) and assuming chemical equilibrium, the equilibrium distribution of gas atoms in voids, can be solved for as

$$N_j^{eq}(m) = M_j\exp(m\ln S_v - \xi m^{2/3} + j\ln(p^{eq}/p)). \tag{4.22}$$

where $\xi = (4\pi/kT)(3\Omega/4\pi)^{2/3}\gamma$. The exponential term represents the free energy of cluster formation. Whereas in the homogeneous void nucleation case this was a function of m alone, this term represents an energy surface dependent on both m and j. Solution of the nucleation current I_j follows (4.17), with the critical cluster size now a function of j. Following a similar procedure as the homogeneous case, it can be expressed as

$$I_j = \left[\frac{1}{2\pi}\left(\frac{\mathrm{d}^2\ln h_j}{\mathrm{d}m^2}\right)_{m_{cj}}\right]^{1/2}\beta_v(m_{cj})h_j(m_{cj}). \tag{4.23}$$

where the function h_j is defined in (4.16) with j subscripts added to $h(m)$ and $N^{eq}(m)$.

4.2 Development of a Reduced Set of Rate Equations for Radiation Damage Rate Theory

The nucleation of stable clusters is followed by a transient growth stage. Classical nucleation theory tends to be inadequate for the modeling of cluster growth due to its very high sensitivity to physical parameters which are typically not known to a high degree of accuracy and the very short timescales involved. In addition, nucleation theory provides knowledge on nucleation rates but does not resolve cluster densities in the material. In most cases cluster growth is modeled via rate theory. Here, a list of coupled rate-equations for the concentrations of species are developed. Each equation equates the concentration rates to the sum of all production and loss rates of the species, stemming from physical phenomena (trapping/de-trapping, recombination, etc). Under the mean-field approximation, where statistical variations in time and space are averaged, these equations are one-dimensional, varying only with time. For the case of radiation induced helium-vacancy (HV) clustering, rate theory models have in the past been developed. Following a study by Ghoniem [96], a reduced set of rate equations for the concentrations of vacancies (C_v), self-interstitials (C_i), helium interstitials (C_g), helium substitutionals (C_{gv}), di-helium interstitials (C_{2g}), di-helium mono-vacancy (C_{2gv}) and the critical nucleus (C^*) can be expressed as

$$dC_v/dt = fG + (\beta e_1 + \delta)C_{gv} - [\alpha C_i + \beta C_g + \gamma(C_s^v + C_{gv} + 2C_{2g} + 2C_{2gv} + 3C^*)]C_v, \tag{4.24}$$

$$dC_i/dt = fG - \alpha(C_v + C_{gv} + 2C_{2gv} + 3C^* - C_s^i)C_i, \tag{4.25}$$

$$\begin{aligned} dC_g/dt = {} & G_H + (\beta e_1 + \delta + \alpha C_i)C_{gv} + (\beta e_2 + 2\delta)C_{2gv} + 3(\delta + \alpha C_i)C^* + 4\delta C_{2g} \\ & + 4\alpha C_i C_{2gv} + m\delta_{tot} + \delta M_{GB} + \delta M_{ppt} - \beta[\epsilon C_B + C_v + 4C_g + C_{gv} \\ & + 2C_{2g} + 2C_{2gv} + C_{GB} + \varepsilon_{ppt}C_{ppt}]C_g, \end{aligned} \tag{4.26}$$

$$dC_{gv}/dt = \beta C_g C_v + (e_2 + 2\delta)C_{2gv} - [e_1 + \beta C_g + \delta(1 + C_v) + \alpha C_i]C_{gv}, \tag{4.27}$$

$$dC_{2g}/dt = 2\beta C_g^2 + 3\alpha C_i C^* - 2(\gamma C_v + \beta C_g + \delta)C_{2g}, \tag{4.28}$$

$$dC_{2gv}/dt = \beta C_g C_{gv} + 3\delta C^* + 2\gamma C_v C_{2g} - [2\beta C_g + 2\delta(1 + C_v) + \beta e_2 + 2\alpha C_i]C_{2gv}, \tag{4.29}$$

$$dC^*/dt = 2\beta(C_{2g} + C_{2gv})C_g - 3(\beta C_g + \gamma C_v + \alpha C_i + \delta)C^*, \tag{4.30}$$

$$\tag{4.31}$$

respectively. Here, the critical nucleus is taken as any cluster containing three helium atoms. For clusters beyond the critical nucleus size, an average bubble is defined, whose size is determined by the number of vacancies in the bubble. Rate equations for the concentration of average bubbles (C_b) and their radius (R) are defined as

$$dC_b/dt = \frac{12}{m_1}\beta C_g C^* + \frac{9}{m_1}\gamma C_v C^*, \tag{4.32}$$

$$dR/dt = \frac{a^2}{R}\left[\gamma C_v - \alpha C_i - \gamma(e_3 - e_4)\right], \tag{4.33}$$

The system sinks present are assumed to be dislocations, grain boundaries and precipitates. Expressions for the concentration of helium atoms in bubbles (m_1), at precipitates (M_{ppt}) and grain boundaries (M_{GB}) are given as

$$dm_1/dt = \epsilon\beta C_g - \delta m_1, \tag{4.34}$$

$$dM_{ppt}/dt = \varepsilon_{ppt}\beta C_{ppt}C_g - \delta M_{ppt}, \tag{4.35}$$

$$dM_{GB}/dt = \beta C_{GB}C_g - \delta M_{GB}. \tag{4.36}$$

The reaction frequencies of self-interstitials (α), helium (β) and vacancies (γ) and the thermal emission probabilities of vacancies (e_1, e_2, e_3, e_4) in the above equations are given as

$$\begin{aligned} \alpha &= 48\nu_i \exp(-E_i^m/kT), & e_1 &= \exp(-E_{v,g}^b/kT), \\ \beta &= 48\nu_g \exp(-E_g^m/kT), & e_2 &= \exp(-E_{v,2g}^b/kT), \\ \gamma &= 48\nu_v \exp(-E_v^m/kT), & e_3 &= \exp(-E_{v,b}^b(R,p)/kT), \\ \delta &= bG, & e_4 &= \exp(-E_v^f/kT), \end{aligned}$$

where the factor of 48 is the assumed combinatorial number, ν is the atomic jump frequency and E^m and E^b represent migration and binding energies, respectively. The factor δ is called the re-solution frequency and represents the probability per displacement for dissolving a helium atom back into the matrix (b) times the displacement damage rate (G). We note the binding energy of vacancies to bubbles, $E^b_{v,b}(R,p)$, is a function of both the bubble radius and internal pressure due to helium gas atoms, and will be described in more detail in the next chapter. Descriptions of the remaining symbols are given in the following nomenclature.

NOMENCLATURE

f	Fraction of surviving Frenkel pairs per displacement.
G	Displacement damage rate.
G_H	Helium production rate.
C_s^i	Equivalent matrix-distributed sink density for interstitials.
C_s^v	Equivalent matrix-distributed sink density for vacancies.
C_{GB}	Equivalent grain boundary sink concentration.
ε_{ppt}	Precipitate cavity combinatorial number.
C_{ppt}	Equivalent precipitate sink concentration.

Solving the above coupled rate equations in time gives insight into the roles of various mechanisms on cluster nucleation as well as growth rates in irradiated metals. During the initial stages of irradiation, helium atoms are generated as interstitials, but soon are trapped when vacancies become available. These types of calculations have in the past revealed that the primary available mechanism for reducing helium transport to grain boundaries is the growth of bubbles as available sinks. In the following section, a spatially resolved rate theory framework is developed to study the near surface growth of bubbles under stress and temperature gradients in materials under irradiation.

4.3 Spatially Resolved Rate Theory of Point Defect Clustering in Stress and Temperature Gradients

In the state we have presented them thus far, the reduced set of rate equations, equations (4.24) through (4.36), have no spatial variance and are used only in an average, homogeneous sense, assumed valid for all space. Under stress and temperature gradients, however, the spatial aspect becomes very important. In this section, we modify the reduced set to include spatially-dependent flux and drift terms. To do this, we will divide the reduced set into two groups: mobile and immobile. For the mobile species, we have chosen vacancies, self-interstitials, helium interstitials and bubbles. Rate equations for all other species remain spatially invariant due to their increased solubility. Modification of the rate equations for the mobile species is straightforward and we get

$$\begin{aligned} dC_v/dt &= fG + (\beta e_1 + \delta)C_{gv} - [\alpha C_i + \beta C_g + \gamma(C_s^v + C_{gv} + 2C_{2g} + 2C_{2gv} + 3C^*)]C_v \\ &\quad + D_v \nabla^2 C_v + \frac{D_v}{kT}\nabla \cdot [C_v \nabla E_{int}^v], \qquad (4.37) \\ dC_i/dt &= fG - \alpha(C_v + C_{gv} + 2C_{2gv} + 3C^* - C_s^i)C_i \\ &\quad + D_i \nabla^2 C_i + \frac{D_i}{kT}\nabla \cdot [C_i \nabla E_{int}^i], \qquad (4.38) \\ dC_g/dt &= G_H + (\beta e_1 + \delta + \alpha C_i)C_{gv} + (\beta e_2 + 2\delta)C_{2gv} + 3(\delta + \alpha C_i)C^* + 4\delta C_{2g} \\ &\quad + 4\alpha C_i C_{2gv} + m\delta_{tot} + \delta M_{GB} + \delta M_{ppt} - \beta[\epsilon C_B + C_v + 4C_g + C_{gv} \\ &\quad + 2C_{2g} + 2C_{2gv} + C_{GB} + \varepsilon_{ppt} C_{ppt}]C_g + D_h \nabla^2 C_g + \frac{D_h}{kT}\nabla \cdot [C_g \nabla E_{int}^g], \qquad (4.39) \\ dC_b/dt &= \frac{12}{m_1}\beta C_g C^* + \frac{9}{m_1}\gamma C_v C^* + D_b \nabla^2 C_b + \frac{D_b}{kT}\nabla \cdot (v_b C_b). \qquad (4.40) \end{aligned}$$

Here we have added terms stemming from the Brownian flux and drift terms. For the first three species, the drift is dependent on the interaction energy and under stress gradients can be calculated using equations (2.19) and (2.20). For bubbles, we will go into a more complete description.

4.3.1 Drift Diffusion of Bubbles in Stress and Temperature Gradients

The diffusion of bubbles is a classical problem addressed in the past by numerous authors. In metals, the diffusion of spherical voids is known to occur primarily by a surface diffusion mechanism where matrix atoms on the bubble surface migrate in one direction effectively moving the bubble's center of mass in the other direction. Under this description, the diffusion coefficient can be expressed as

$$D_b = \frac{3a_0\Omega}{2\pi R^4} D_s \tag{4.41}$$

where D_s is the surface diffusion coefficient of an adatom on the inner bubble surface [97]. When a bubble is residing in a drift field, the drift velocity, v_b is taken as the mobility, $B = D/kT$, times the force, F. For calculations of the force, the most notable theoretical contributions for bubbles migrating in stress and temperature gradients, were by Eshelby [98] and Nichols [97], respectively. Under a temperature field varying in the x direction, Nichols gives the expression

$$F_b = \left(\frac{4\pi R^3}{3\Omega}\right) \frac{3Q_s^*}{2T} \left(\frac{dT}{dx}\right), \tag{4.42}$$

where Q_s^* is the heat of transport characterizing the surface Soret effect and T is the local temperature. Under a stress field varying in x, the expression given by Eshelby [98] for the force on a bubble is

$$F_b = \frac{3}{2} \left(\frac{\pi R^3}{G}\right) \sigma_L \left(\frac{d\sigma}{dx}\right). \tag{4.43}$$

Under conditions typical of the environments of interest in this thesis ($\nabla\sigma \sim 0.1 -$ 10 GPa/μm,∇T $\sim$ 1-20 K/μm), quick hand calculations show that forces due to temperature gradients are at least several orders of magnitude greater than those due to associated stress gradients. However, in our problem there are two timescales at play; the short timescale for the rapidly diffusing point defects and the longer timescale of bubble diffusion. Thus at this point it remains unclear whether or not the stress gradients can be ignored from the point defect perspective, which is what we hope to clarify in our calculations.

4.3.2 Description of the Simulations and Results

For the simulations, a finite element method is developed to simultaneously solve equations (4.27)-(4.36) and (4.37)-(4.40). The geometry chosen is a rectangular tungsten cell 50 microns wide in the x direction by 10 microns high in y. The faces in the y direction are given periodic boundary conditions, while in the x direction, the left side represents the free plasma-facing surface and the right side is deep into the bulk. These sides are given zero flux boundary conditions. The first 20 microns into the sample are given negative constant temperature gradients ranging from 1-20 [K/μm] with the left surface held at constant temperature at 1300 K. A dose rate of 3x10-4 dpa/s for one hour is used with a helium generation rate of 5 appm/dpa. The rest of the parameters can be found in the W column of table 4.3.2. To compare the effects of stress gradients to temperature gradients, we first ran cases with only temperature gradients present, then ran separate cases where we allowed stress gradients. An example of such results can be found in figure 4.3.

The plot on the left shows the average bubble radius profile into the specimen after 1 hour of exposure to a temperature gradient of 20 K/μm with and without

	Fe	W	Units	Description
K	3×10^{-3}	3×10^{-3}	dpa/s	Displacement damage rate
E_i^m	0.2	0.102	eV	Interstitial migration energy
E_g^m	0.06	0.07	eV	Helium migration energy
E_v^m	0.67	1.66	eV	Vacancy migration energy
E_{vg}^b	2.4	4.05	eV	Substitutional binding energy
E_v^f	1.6	3.11	eV	Vacancy formation energy
E_{v2g}^b	3.5	3.14	eV	He to He_2V binding energy
E_{2g}^b	0.79	0.79	eV	He to He_2 binding energy
E_i^f	4.08	9.82	eV	Interstitial formation energy
ρ_N	3×10^{10}	3×10^{10}	cm^{-2}	Dislocation density
Z_i	1.2	1.2	-	Interstitial bias factor
H	5×10^{-6}	5×10^{-6}	dpa^{-1}	Helium to dpa ratio
a	2.866×10^{-8}	3.146×10^{-8}	cm	Lattice parameter
ν_i	5×10^{13}	5×10^{13}	s^{-1}	Interstitial vibration frequency
ν_g	5×10^{13}	5×10^{13}	s^{-1}	Helium vibration frequency
ν_v	5×10^{12}	5×10^{12}	s^{-1}	Vacancy vibration frequency
b	1	1	-	re-solution parameter

Table 4.1: Parameters for iron and tungsten used in the rate-theory calculations.

stress gradients. Our simulations have shown that the stress gradients have a very significant impact on the bubble size profile near the surface. In this case we find near-surface bubble sizes three times larger when stress gradients are applied as opposed to temperature gradients alone. When analyzing the plot to the right of figure 4.3 in conjunction with the bubble radius plot we see the experimentally observed phenomena similar to figure 4.1. Specifically, we find a small density of large bubbles near the surface with larger densities of smaller bubbles as we move into the material. This is found to occur by point-defect drift processes as follows. Increased compressive stresses near the free surface repel helium and self interstitial atoms while attracting vacancies. Naturally, this leads to fewer nucleation sites (reduced density) and increased growth rates (larger bubbles). The computational framework developed here allows for many scenarios and timescales to be simulated. The large degree of parameterization in the equations allows for much freedom with regard to irradiation conditions. Additionally, the FEM implementation allows for any geometry or component to be simulated. The computational expense is very minimal, and its

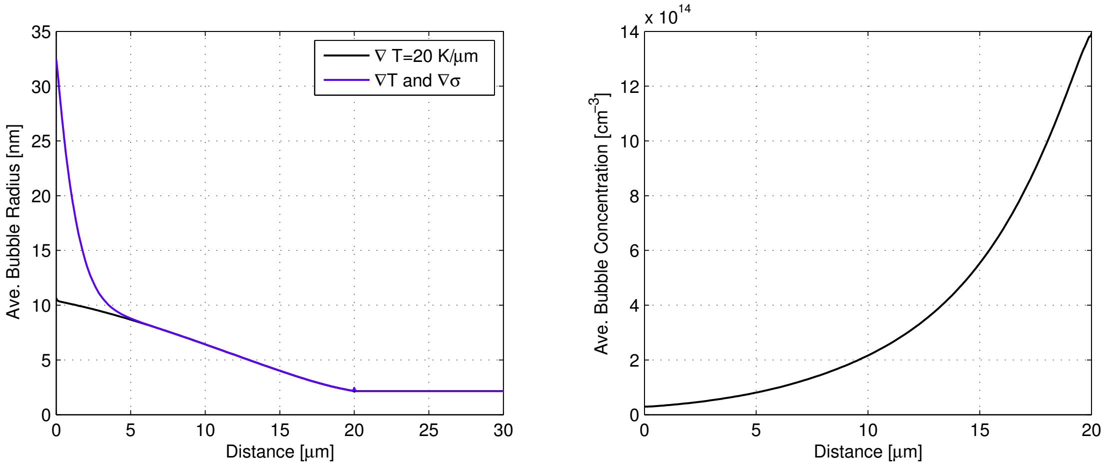

Figure 4.3: Average bubble radius (left) and average bubble concentration (right) versus distance from the free surface.

predictive capabilities can be easily tuned with knowledge of experimental results. As

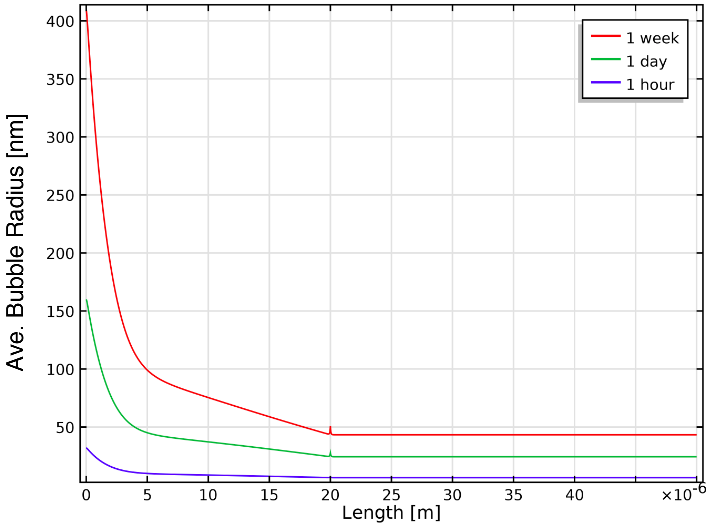

Figure 4.4: Average bubble radius versus distance from the free surface after three different exposure times. Stress and temperature gradients are applied to the first 20 μm into the material.

an example, in figure 4.4 we extend the irradiation exposure times beyond one hour to 24 hours and one week. With proper tuning of the parameters, this tool could be used as a computational microscope to determine the current state of a component's microstructure and estimate its remaining operating life.

CHAPTER 5

Stochastic Approach to the Size Distribution of Helium Bubbles in Metals

Due to stochastic fluctuations in the absorption of point defects by bubbles, there exists a spectrum of bubble sizes, each size with a spectrum of the number of helium contained within. For this reason, a simple "average bubble" approach is not suitable for a complete description of the microstructure. In this chapter, we expand on the work of the previous chapter to develop a method to accurately estimate the full helium-vacancy bubble size distribution as a function of time and space. Due to the stochastic nature of point defect diffusion, we develop an approach based on formulations from the field of stochastic differential equations.

5.1 Helium-Vacancy Cluster Size Distribution

Our objective is to describe the evolution of the helium-vacancy size distribution, $p(x_1, x_2, t)$, as a function of time, where helium atoms and vacancies, are represented by x_1 and x_2, respectively. In the previous chapter we presented two equations for the mean radius of and number of helium atoms in average sized bubbles, (4.33) and (4.34). The developed method is very general, and can be extended to a description of the size distribution as a function of space and time in any irradiated material. Under the approximation that the number of vacancies times the atomic volume equals the total bubble volume, we can express the rate equations for the species as

$$\frac{\partial x_1}{\partial t} = 4\pi R \Omega^{-1}(D_h C_h) - x_1 b \tag{5.1}$$

$$\frac{\partial x_2}{\partial t} = \frac{4\pi R}{\Omega}\left(D_v C_v - D_i C_i - D_v C_v^e \left\{\exp\left[\frac{\Omega}{kT}\left(\frac{2\gamma}{R} - p\right)\right] - 1\right\}\right) \tag{5.2}$$

Where the bubble radius and pressure are given as

$$R = \left(\frac{3\Omega}{4\pi}\right)^{\frac{1}{3}} x_2^{\frac{1}{3}} \qquad \text{and} \qquad p = \frac{x_1 kT}{(4/3)\pi R^3 - x_1 B}. \tag{5.3}$$

For equation (5.1), the first term on the right hand side represents the rate at which helium atoms impinge on bubbles of radius R, while the second represents their rate of re-solution into the matrix. In equation (5.2), the number of vacancies in bubbles is governed by three processes: (1) the capture of diffusing vacancies, (2) the capture of SIAs, and (3) the thermal emission of vacancies, as seen in the three terms in the equation. When used in conjunction with equations (4.24) through (4.36), these average values can be tracked in time. In this work, however, we wish to obtain the full size distribution and not simply the mean values. In our approach, we begin by stating one major approximation in our approach. That is, that the full distribution can be adequately modeled with a two-dimensional Gaussian distribution described entirely by five moments: the two first and second moments and a covariance moment term. The challenge we then face is obtaining equations for the second moments and covariance term. To obtain such expressions, we have found the use of nonlinear stochastic differential equations with Itô's rule to be a powerful tool. In what follows, we describe the method of differential equations for stochastic processes and describe the methodology for applying it to the cluster size distribution problem. With equations for the moments of the distribution known, a path integral approach is presented to reconstruct and evolve the distribution in time.

5.1.1 Stochastic Differential Form Representation of the Cluster Evolution Equations

When an otherwise deterministic variable, $x_i(t)$, is excited by a stochastic Brownian process, $dW(t)$, in general differential form, $x_i(t)$ can be expressed as

$$\mathrm{d}x_i(t) = f_i(x_i(t), t)\mathrm{d}t + g_i(x_i(t), t)\mathrm{d}W_i(t) \tag{5.4}$$

where $dW(t)$ is a time continuous Wiener process representing Brownian fluctuations in the variable. If we add these stochastic white noise fluctuations to (5.1) and (5.2), we can express them in stochastic differential form as

$$\mathrm{d}x_1 = [4\pi\Omega^{-1}(D_h C_h)R - x_1 b]\mathrm{d}t + g_{x_1}(x_1, x_2, t)\mathrm{d}W_{x_1}(t) \tag{5.5}$$

and

$$\mathrm{d}x_2 = \left[\frac{4\pi R}{\Omega}\left(D_v C_v - D_i C_i - D_v C_v^e \left\{\exp\left[\frac{\Omega}{kT}\left(\frac{2\gamma}{R} - p\right)\right] - 1\right\}\right)\right]\mathrm{d}t + g_{x_2}(x_1, x_2, t)\mathrm{d}W_{x_2}(t) \tag{5.6}$$

where the functions $g_i(x_1, x_2, t)$, $(i = x_1, x_2)$ have yet to be determined. For improved clarity, we can re-express (5.5) and (5.6) as

$$\mathrm{d}x_1 = \left(c_1 x_2^{1/3} - c_2 x_1\right)\mathrm{d}t + g_{x_1}(x_1, x_2, t)\mathrm{d}W_{x_1}(t) \tag{5.7}$$

and

$$\mathrm{d}x_2 = \left[c_3 x_2^{1/3} - c_4 x_2^{1/3} \exp\left(c_5 x_2^{-1/3} - \frac{c_6 x_1}{c_6 x_2 - c_7 x_1}\right)\right]\mathrm{d}t + g_{x_2}(x_1, x_2, t)\mathrm{d}W_{x_2}(t) \tag{5.8}$$

where

$$\begin{aligned}
c_1 &= \left(\frac{4\pi\sqrt{3}}{\Omega}\right)^{2/3} (D_h C_h) \\
c_2 &= b \\
c_3 &= \left(\frac{4\pi\sqrt{3}}{\Omega}\right)^{2/3} (C_v D_v - C_i D_i + C_v^e D_v) \\
c_4 &= \left(\frac{4\pi\sqrt{3}}{\Omega}\right)^{2/3} C_v^e D_v \\
c_5 &= \frac{4\gamma}{kT} \left(\frac{2\pi\Omega^2}{3}\right)^{1/3} \\
c_6 &= \Omega \\
c_7 &= B
\end{aligned} \tag{5.9}$$

We note here that the factors c_1 and c_3 are both spatially and temporally dependent.

5.2 Path Integral Solution Approach

The solution of a general one-dimensional stochastic differential equation, such as (5.4), at any point, x_i, may be approximately solved using a path integral approach. In a paper by Yu and co-workers [99], such a scheme was developed for calculating the probability density functions of one-dimensional variables under stochastic white noise processes. Here, we follow their procedure, extending it to two-dimensional, helium-vacancy phase space. For clarity, we distinguish between the independent variables constituting the phase space (here, x_1 and x_2, representing the number of helium atoms and vacancies in a cluster), and the independent Cartesian variables x, y, z that represent the coordinates of a material point.

Assuming the transition probability, $q(x(t), t)$, for our distribution is not directly known, over a very short time span it may be approximated as a Gaussian, or

$$q(x^{(k)}, t_k | x^{(k-1)}, t_{k-1}) = \frac{1}{\sqrt{2\pi}\sigma(t_k)} \exp\left(-\frac{[x^{(k)} - m_1(t_k)]^2}{2\sigma^2(t_k)}\right) \tag{5.10}$$

where $m_j(t_k)$ represents the j^{th} moment of $x_i(t)$ at the k^{th} timestep and $\sigma^2(t_k) = m_2(t_k) - [m_1(t_k)]^2$. Then, assuming the PDF at the previous timestep, $p(x^{(k-1)}, t_{k-1})$ is known, the value for $p(x_i(t), t)$ at the current timestep can be solved for as

$$p(x^{(k)}, t_k) = \int_{x_R} q(x^{(k)}, t_k | x^{(k-1)}, t_{k-1}) p(x^{(k-1)}, t_{k-1}) \mathrm{d}x^{(k-1)} \tag{5.11}$$

Using this method to evolve our PDF, we need only to derive expressions for the moments of our variable x_1 to obtain the transition probabilities from (5.10) and compute the current distribution.

To extend this method to two dimensional space in x as in our current problem, we can express the transition probability at a quadrature point i on our PDF at timestep k as

$$q((x_1, x_2)_k^{(i)}, t_k | (x_1, x_2)_{k-1}^{(i)}, t_{k-1}) = \frac{1}{2\pi\sqrt{1-\rho^2}\sigma_1\sigma_2} \exp\left[\frac{\frac{x_1^2}{\sigma_1^2} - 2\rho\frac{x_1 x_2}{\sigma_1\sigma_2} + \frac{x_2^2}{\sigma_2^2}}{2(1-\rho^2)}\right] \tag{5.12}$$

where σ_1, σ_2 and ρ are defined in terms of the moments of x_1 and x_2 as

$$\sigma_1^2 = m_{20} - m_{10}^2, \tag{5.13}$$

$$\sigma_2^2 = m_{02} - m_{01}^2, \tag{5.14}$$

$$\rho = \frac{m_{11}}{\sigma_1\sigma_2}. \tag{5.15}$$

Here, m_{ij} represents the coupled i^{th} moment of x_1 and j^{th} moment of x_2. For $i = 0$ or $j = 0$, the moment is fully decoupled. Next, we can discretize the PDF into a two dimensional grid and numerically solve using a Gauss-Legendre approximation as

$$p(x^{(i)}, t_i) = \sum_{m=1}^{M} \frac{\delta_m}{2} \sum_{n=1}^{N_m} w_{mn} \sum_{k=1}^{K} \frac{\delta_k}{2} \sum_{l=1}^{L_k} w_{kl} p(x_{mn,kl}^{(i-1)}, t_{i-1}) q(x^{(i)}, t_i | x_{mn,kl}^{i-1}, t_{i-1}) \tag{5.16}$$

where M and K are the number of segments in the x_1 and x_2 directions, respectively, N_m and L_k are the respective number of quadrature points in the m^{th} and k^{th} segments, and δ_m and δ_k are the lengths of segments m and k, respectively. This solution approach is useful particularly when the transition probabilities are not known as functions of time, but can be approximated over very short time intervals as Gaussian themselves, leading to a continuous solution.

5.3 Itô's Rule for Obtaining Moments of Stochastic Differential Equations

5.3.1 For One-Dimensional Processes

Given the differential equation for a stochastic variable $x_i(t)$, as in (5.4), we can compute any function of $x_i(t)$, such as $Y(t) = \phi(x_i(t), t)$, using Itô's rule [100]. Itô's rule provides a correction factor to the traditional chain rule of calculus, accounting for stochastic effects. Let $\phi(x_i(t), t)$ be an arbitrary function of time and $x_i(t)$. Then, according to Itô's rule

$$\mathrm{d}Y_i(t) = \tilde{f}_i(x_i(t), t)\mathrm{d}t + \tilde{g}_i(x_i(t), t)\mathrm{d}W_i(t) \tag{5.17}$$

where

$$\tilde{f}_i(x_i(t), t) = \frac{\partial}{\partial t}\phi(x_i(t), t) + \frac{\partial}{\partial x_i}[\phi(x_i(t), t)]f_i(x_i(t), t) + \frac{1}{2}\frac{\partial^2}{\partial x_i^2}[\phi(x_i(t), t)]g_i^2(x_i(t), t) \tag{5.18}$$

$$\tilde{g}_i(x_i(t), t) = \frac{\partial}{\partial x}[\phi(x_i(t), t)]g_i(x_i(t), t) \tag{5.19}$$

Using this approach, we can obtain the moments of $x_i(t)$ in a straightforward way. For example, if we choose $Y(x_1, x_2, t) = \phi(x_1(t), x_2(t), t) = x_1^2$, we can easily take the derivatives and calculate (5.18) and (5.19) and obtain the stochastic ODE (5.17). Then, taking ensemble averages of each term we can obtain the differential form equation for the second moment in x_1 as $\mathrm{E}[\mathrm{d}Y(t)]$=$\mathrm{dE}[Y(t)]$=$\mathrm{dE}[x_1^2] = dm_{20}$.

5.3.2 For Correlated Stochastic Processes

For multiple correlated stochastic processes, such as the helium and vacancy time evolution, Itô's rule takes a modified form. In this case, suppose we want to calculate an arbitrary function of time and x_1 and x_2, $Y(t) = \phi(x_1, x_2, t)$, where x_1 and x_2 are correlated stochastic processes. In this case (5.18) and (5.19) become

$$\tilde{f}(x_1, x_2, t) = \left[\phi,_t + \phi,_{x_1} f_{x_1} + \phi,_{x_2} f_{x_2} + \frac{1}{2}\phi,_{x_1x_1} g_{x_1}^2 + \frac{1}{2}\phi,_{x_2x_2} g_{x_2}^2 + \rho g_{x_1} g_{x_2} \phi,_{x_1x_2}\right] \tag{5.20}$$

$$\tilde{g}(x_1, x_2, t) = \phi,_{x_1} g_{x_1} \mathrm{d}W_{x_1}(t) + \phi,_{x_2} g_{x_2} \mathrm{d}W_{x_2}(t) \tag{5.21}$$

where commas denote derivatives 'with respect to' and W_{x_1} and W_{x_2} are correlated Brownian terms with correlation coefficient ρ, defined by $\mathrm{E}[\mathrm{d}W_{x_1}\mathrm{d}W_{x_2}] = \rho \mathrm{d}t$.

5.3.3 Helium Equation

First Moment, m_{10}=$E[x_1]$

The calculation of the first moment of equation (5.5) is straightforward:

$$\mathrm{dE}[x_1] = \left(c_1\mathrm{E}[x_2^{\frac{1}{3}}] - c_2\mathrm{E}[x_1]\right)\mathrm{d}t + \mathrm{dE}[g_{x_1}(x_1, x_2, t)W_{x_1}(t)] \tag{5.22}$$

$$\dot{m}_{10} = c_1\mathrm{E}[x_2^{\frac{1}{3}}] - c_2 m_{10} \tag{5.23}$$

Second Moment, m_{20}=$E[x_1^2]$

For the second moment, we follow Itô's rule, choosing $Y(t) = \phi(x_1, x_2, t) = x_1^2$. Then our non-vanishing terms from (5.20) and (5.21) are

$$\tilde{f}(x_1, x_2, t) = \frac{\partial}{\partial x_1}[\phi(x_1, x_2, t)]f_{x_1}(x_1, x_2, t) + \frac{1}{2}\frac{\partial^2}{\partial x_1^2}[\phi(x_1, x_2, t)]g_{x_1}^2(x_1, x_2, t) \tag{5.24}$$

$$= 2x_1\left(c_1 x_2^{1/3} - c_2 x_1\right) + \frac{1}{2}(2)g_{x_1}^2(x_1, x_2, t) \tag{5.25}$$

$$\tilde{g}(x_1, x_2, t) = \frac{\partial}{\partial x_1}[\phi(x_1, x_2, t)]g_{x_1}(x_1, x_2, t) \tag{5.26}$$

$$= 2x_1 g(x_i(t), t) \tag{5.27}$$

Now, according to (5.17), we have

$$\mathrm{d}Y(t) = \left[2x_1\left(c_1 x_2^{1/3} - c_2 x_1\right) + \frac{1}{2}(2)g_{x_1}^2(x_1, x_2, t)\right]\mathrm{d}t + 2x_1 g_{x_1}(x_1, x_2, t)\mathrm{d}W_{x_1}(t) \tag{5.28}$$

$$= \left[2c_1 x_1 x_2^{1/3} - 2c_2 x_1^2 + g_{x_1}^2(x_1, x_2, t)\right]\mathrm{d}t + 2x_1 g_{x_1}(x_1, x_2, t)\mathrm{d}W_{x_1}(t) \tag{5.29}$$

and taking expectation values, we get

$$\mathrm{dE}[Y(t)] = \left(2c_1\mathrm{E}[x_1 x_2^{1/3}] - 2c_2\mathrm{E}[x_1^2] + \mathrm{E}[g^2(x_1, x_2, t)]\right)dt + 2\mathrm{E}[x_1 g(x_1, x_2, t)] \tag{5.30}$$

$$\dot{m}_{20} = 2c_1\mathrm{E}[x_1 x_2^{1/3}] - 2c_2 m_{20} + \mathrm{E}[g^2(x_1, x_2, t)] \tag{5.31}$$

5.3.4 Vacancy Equation

First Moment, m_{01}=$E[x_2]$

The calculation of the first moment of equation (5.6) follows as

$$\mathrm{dE}[x_2] = \left\{c_3\mathrm{E}[x_2^{1/3}] - c_4\mathrm{E}\left[x_2^{1/3}\exp\left(c_5 x_2^{-1/3} - \frac{c_6 x_1}{c_6 x_2 - c_7 x_1}\right)\right]\right\}\mathrm{d}t$$
$$+\mathrm{E}[g_{x_2}(x_1, x_2, t)\mathrm{d}W_{x_2}(t)] \tag{5.32}$$

$$\dot{m}_{01} = c_3\mathrm{E}[x_2^{1/3}] - c_4\mathrm{E}\left[x_2^{1/3}\exp\left(c_5x_2^{-1/3} - \frac{c_6x_1}{c_6x_2 - c_7x_1}\right)\right] \tag{5.33}$$

Second Moment, $m_{02}{=}E[x_1^2]$

For the second moment, we follow Itô's rule, choosing $Y(t) = \phi(x_1, x_2, t) = x_2^2$. Then our non-vanishing terms from (5.20) and (5.21) are

$$\tilde{f}(x_1, x_2, t) = \frac{\partial}{\partial x_2}[\phi(x_1, x_2, t)]f(x_1, x_2, t) + \frac{1}{2}\frac{\partial^2}{\partial x_2^2}[\phi(x_1, x_2, t)]g^2(x_1, x_2, t) \tag{5.34}$$

$$= 2x_2\left[c_3x_2^{1/3} - c_4x_2^{1/3}\exp\left(c_5x_2^{-1/3} - \frac{c_6x_1}{c_6x_2 - c_7x_1}\right)\right] + \frac{1}{2}(2)g_{x_2}^2(x_1, x_2, t) \tag{5.35}$$

$$\tilde{g}(x_1, x_2, t) = \frac{\partial}{\partial x_2}[\phi(x_1, x_2, t)]g_{x_2}(x_1, x_2, t) \tag{5.36}$$

$$= 2x_2g(x_i(t), t) \tag{5.37}$$

Now, according to (5.17), we have

$$\mathrm{d}Y(t) = \left[2x_2\left(c_3x_2^{1/3} - c_4x_2^{1/3}\exp\left(c_5x_2^{-1/3} - \frac{c_6x_1}{c_6x_2 - c_7x_1}\right)\right) + g_{x_2}^2(x_1, x_2, t)\right]\mathrm{d}t$$
$$+ 2x_2g_{x_2}(x_1, x_2, t)\mathrm{d}W_{x_2}(t) \tag{5.38}$$

$$= \left[2c_3x_2^{4/3} - 2c_4x_2^{4/3}\exp\left(c_5x_2^{-1/3} - \frac{c_6x_1}{c_6x_2 - c_7x_1}\right) + g_{x_2}^2(x_1, x_2, t)\right]\mathrm{d}t$$
$$+ 2x_2g_{x_2}(x_1, x_2, t)\mathrm{d}W_{x_2}(t) \tag{5.39}$$

and taking expectation values, we get

$$\mathrm{dE}[Y(t)] =$$
$$\left[2c_3\mathrm{E}[x_2^{4/3}] - 2c_4\mathrm{E}[x_2^{4/3}\exp\left(c_5x_2^{-1/3} - \frac{c_6x_1}{c_6x_2 - c_7x_1}\right)] + \mathrm{E}[g_{x_2}^2(x_1, x_2, t)]\right]\mathrm{d}t$$
$$+ 2\mathrm{E}[x_2g_{x_2}(x_1, x_2, t)\mathrm{d}W_{x_2}(t)] \tag{5.40}$$

$$\dot{m}_{02} = 2c_3\mathrm{E}[x_2^{4/3}] - 2c_4\mathrm{E}[x_2^{4/3}\exp\left(c_5x_2^{-1/3} - \frac{c_6x_1}{c_6x_2 - c_7x_1}\right)] + \mathrm{E}[g_{x_2}^2(x_1, x_2, t)] \quad (5.41)$$

5.3.5 Coupled Moment, m_{11}=$E[x_1x_2]$

For the coupled moment, we choose $Y(t) = \phi(x_1, x_2, t) = x_1x_2$. Then following (5.20) and (5.21), we have

$$\tilde{f}(x_1, x_2, t) = x_2\left[c_1x_2^{1/3} - c_2x_1\right] + x_1\left[c_3x_2^{1/3} - c_4x_2^{1/3}\exp\left(c_5x_2^{-1/3} - \frac{c_6x_1}{c_6x_2 - c_7x_1}\right)\right] + \rho g_{x_1}g_{x_2} \quad (5.42)$$

$$\tilde{g}(x_1, x_2, t) = x_2g_{x_1}\mathrm{d}W_{x_1} + x_1g_{x_2}\mathrm{d}W_{x_2} \quad (5.43)$$

Now, using (5.17) and taking expectation values, we have

$$\mathrm{d}Y(t) = \left[c_1\mathrm{E}[x_2^{4/3}] - c_2\mathrm{E}[x_1x_2] + c_3\mathrm{E}[x_1x_2^{1/3}] - c_4\mathrm{E}[x_1x_2^{1/3}\exp(...)] + \mathrm{E}[\rho g_{x_1}g_{x_2}]\right]\mathrm{d}t + \mathrm{E}[x_2g_{x_1}\mathrm{d}W_{x_1}(t)] + \mathrm{E}[x_1g_{x_2}\mathrm{d}W_{x_2}(t)] \quad (5.44)$$

Assuming the last two terms in (5.44) vanish, we are left with

$$\dot{m}_{11} = c_1\mathrm{E}[x_2^{4/3}] - c_2m_{11} + c_3\mathrm{E}[x_1x_2^{1/3}] - c_4\mathrm{E}[x_1x_2^{1/3}\exp(...)] + \mathrm{E}[\rho g_{x_1}g_{x_2}] \quad (5.45)$$

5.4 Solution Approach to the Size Distribution Problem

Now, we have developed the following five couple differential equations for the first and second moments of the size distribution.

$$\dot{m}_{10} = c_1\mathrm{E}[x_2^{1/3}] - c_2m_{10} \quad (5.46)$$

$$\dot{m}_{01} = c_3\mathrm{E}[x_2^{1/3}] - c_4\mathrm{E}\left[x_2^{1/3}\exp\left(c_5 x_2^{-1/3} - \frac{c_6 x_1}{c_6 x_2 - c_7 x_1}\right)\right] \tag{5.47}$$

$$\dot{m}_{20} = 2c_1\mathrm{E}[x_1 x_2^{1/3}] - 2c_2 m_{20} + \mathrm{E}[g_{x_1}^2(x_1, x_2, t)] \tag{5.48}$$

$$\dot{m}_{02} = 2c_3\mathrm{E}[x_2^{4/3}] - 2c_4\mathrm{E}[x_2^{4/3}\exp\left(c_5 x_2^{-1/3} - \frac{c_6 x_1}{c_6 x_2 - c_7 x_1}\right)] + \mathrm{E}[g_{x_2}^2(x_1, x_2, t)] \tag{5.49}$$

$$\dot{m}_{11} = c_1\mathrm{E}[x_2^{4/3}] - c_2 m_{11} + c_3\mathrm{E}[x_1 x_2^{1/3}] - c_4\mathrm{E}\left[x_1 x_2^{1/3}\exp\left(c_5 x_2^{-1/3} - \frac{c_6 x_1}{c_6 x_2 - c_7 x_1}\right)\right] + \mathrm{E}[\rho g_{x_1} g_{x_2}] \tag{5.50}$$

Because of the high degree of nonlinearity in these equations, after the application of Itô's rule, we will be left with terms with which ensemble averages can not be easily computed directly. Thus, we propose two solutions for cases where we are left with $\mathrm{E}[r(x_1, x_2, t)]$, where $r(x_1, x_2, t)$ is not a simple polynomial expression of x_1, x_2 and t.

1. Linear Approximation: Here, linear approximations for $r(x_1, x_2, t)$ at the current quadrature point, from the previous timestep, (x_1^0, x_2^0), as:

   $$r(x_1, x_2) = r(x_1^0, x_2^0) + (x_1 - x_1^0)\frac{\partial r(x_1, x_2)}{\partial x_1}|_{x_1^0, x_2^0} + (x_2 - x_2^0)\frac{\partial r(x_1, x_2)}{\partial x_2}|_{x_1^0, x_2^0} \tag{5.51}$$

   where x_i^0 represents the value of x_i at the current quadrature point, at the previous step. We note here, the necessity for very small timesteps using this approach.

2. Expectation Value Definition: When the probability density function $p(x_1, x_2, t)$ is known, then the expectation value of any function, $r(x_1, x_2, t)$, can be computed as

   $$\mathrm{E}[r(x_1, x_2, t)] = \int\int_R r(x_1, x_2, t)p(x_1, x_2, t)\mathrm{d}x_2\mathrm{d}x_1 \tag{5.52}$$

   where the integrated region, R, may be chosen such that it encompasses the entire distribution within some chosen tolerance.

In our simulations we have found the latter method to be computationally efficient enough for our needs. However, for more demanding simulations with finer resolution, the former method would provide adequate approximation while remaining computationally efficient. The final missing piece to the problem setup is the estimation of our white noise coefficients, $g_i(x_1, x_2, t)$. These terms represent the magnitudes of fluctuations about the mean and in general can be functions of x_1, x_2 and time. In our case, we break these terms into two categories: (1) fluctuations in the point defect capture and emission from bubbles, and (2) fluctuations stemming from the collision cascades themselves. For the first category, we use the terms on the right hand side of equations (5.1) and (5.2) with one modification. Since interstitial and vacancy absorption by bubbles leads to a spreading of the size distribution surface, we let all terms have a positive contribution, by changing any minus signs to plus signs. For the second category, we define two parameters, G_{He}^{casc} and G_V^{casc}, to represent fluctuations in the absorption of point defects due to the effects of the varying collision cascade atmospheres. Thus, our white noise coefficients take the form

$$g_1^2(x_1, x_2, t) = (\frac{1}{2}c_1\bar{m}_{01}^{1/3} + \frac{1}{2}c_2\bar{m}_{10})^{1/2} + G_{He}^{casc}, \tag{5.53}$$

$$g_2^2(x_1, x_2, t) = \left(\frac{1}{2}c_2\bar{m}_{10}^{1/3} + \frac{1}{2}c_4\bar{m}_{10}^{1/3}\exp{(c_5\bar{m}_{01}^{-1/3} - \frac{c_6\bar{m}_{10}}{c_6\bar{m}_{01} - c_7\bar{m}_{10}})}\right)^{1/2} + G_V^{casc}, \tag{5.54}$$

where the $\bar{m}_{ij}$ terms represent moments from the previous timestep. Now that all terms are properly accounted for we proceed to the solution. The present task is to solve equations solve the coupled rate equations 5.46-5.50, for the moments of the distribution. To do this, we follow a modified version of the finite-element approach used for the bubble migration studies in the previous chapter. First, a rectangular geometry is chosen, then meshed. Since the cluster size distribution in general varies from point to point in the material, we choose a few points in the material to probe the physics and obtain the size distribution. Solution of the stochastic differential equations for the moments requires the variables, c_1-c_7 to be known. Choosing an operating temperature of 1800 K for our tungsten sample, all c_i's are known except for c_1 and c_3, which are time and space dependent. To obtain these, we first perform a rate theory study, solving equations (4.24) through (4.36). We note, that any combination of stress and temperature gradients may be applied as in the previous chapter. In this example, however, we choose zero stress and constant temperature field. Once this simulation is performed, we can obtain the values for c_1 and c_3 as functions of time at the material points we have chosen to probe. A log plot of these variables for a centrally located material point is found in figure 5.1, showing the rapid transient before steady behavior in c_1, which is governed by the helium concentration in the matrix. Now for each material point of interest we can solve the coupled stochastic rate equations for the moments. This must be performed numerically, with the variables c_i interpolated in time from the previous step. To begin the simulation, initial values for the first moments, variances, and covariance of the distribution were chosen and the initial (approximate) distribution was constructed. A grid of 40 by 40 points was used for its construction and for calculations involving integration over the distribution. As the means of the distribution changed in time, a remeshing of the grid was performed. To do this, at each timestep the rectangular grid reconstructed, with its center at (m_{10}, m_{01}) and with half-lengths of $3\sigma_1$ and $3\sigma_2$ in the x_1 and x_2 directions, respecitvely. Several tests showed this covered over 99.99% of the distribution as the distribution moved in He-V space. For very small bubble sizes (small x_2) with low helium content, a truncation of the distribution was made if at any time the tail of the distribution crossed into negative space, leading to complex values for the moments.

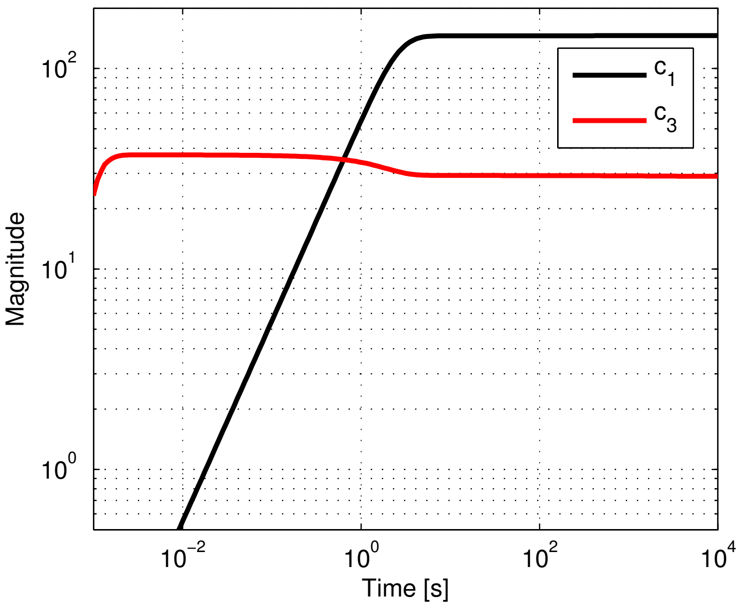

Figure 5.1: Time evolution of the variables c_1 and c_3 for the first few hours of continuous irradiation at the chosen material point

An example run is shown in figure 5.2, showing the evolution of the distribution in the first minute of irradiation time. The initial distribution was chosen to have a mean located at approximately (60,140) with small standard deviations and a covariance factor of ρ =0.5. Upon running the simulation, we almost instantaneously see a rapid spreading of the distribution in the vacancy direction which continues to grow, stabilizing after about 30 seconds of irradiation. This stems from the increased effect of the stochastic fluctuations on smaller sized bubbles. In the helium direction the observed dispersion is also present, though not quite as significant, primarily due to the chosen helium production rate (5 appm/dpa). This was followed by a stable period where the dimensions of the distribution surface (governed by the second moments) remained approximately constant as the mean moved through the He-V phase space. After some time, when the mean bubble sizes become larger, the width of the distribution in the vacancy direction begins to shrink. Physically, this signifies a preference for a single size for all bubbles, which is not physically observed, especially under continuous irradiation. The cause for this stems from the decreased effect of point defect fluctuations on bubbles of larger size. To properly treat this, the model should be extended to include fluctuations that contribute to the spreading of the distribution even when bubble sizes are very large. An important example would be the inclusion of the contributions of bubble coalescence in the white noise terms.

The developed method is very general, and can be extended to a description of the size distribution as a function of space and time in any irradiated material. The large degree of parameterization allows for excellent flexibility and increased accuracy, particularly when experimental data is available.

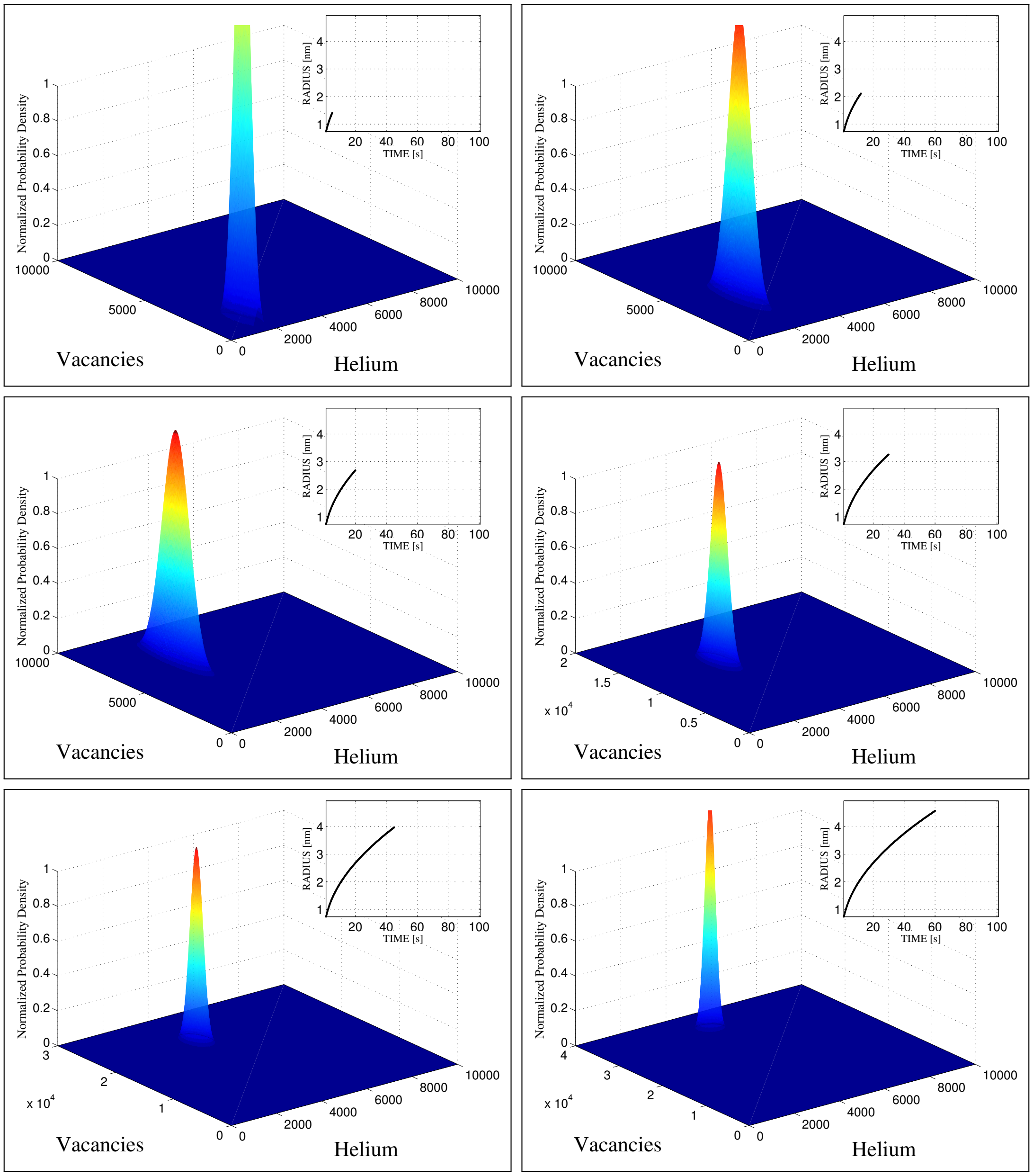

Figure 5.2: Evolution of the helium-vacancy size distribution spanning one minute of irradiation time. The plot is normalized to a value chosen such that the distribution is clearly visible in the plot window. The mean bubble radius is plotted in the inset.

Chapter 6

Ultra-High Strain Rate Deformation of Nano-Structured Metals

In this chapter, we use molecular dynamics simulations to attempt to uncover the atomic mechanisms by which materials respond to ultra-high strain rates. Using copper as a model face-centered cubic metal, our simulations take on three schemes in the three sections that follow. In the first, we explore the response of bulk nanofilms to shock loading, focusing on the characteristics of propagation of the plastic front, as well as internal stresses and temperatures. In the second, recent experimental results motivate our simulations of shock-loading in finite sized nanopillars. Here, we focus on the effects of free surfaces on defect nucleation and deformation characteristics and compare the results with the nanofilms. In the third scheme, we perform simulations of shock-induced void nucleation and spallation in bulk nanostructures.

6.0.1 Description of the Simulations

All of the MD simulations in this chapter were performed with LAMMPS software [101], with the Mishin EAM interatomic potential for copper [80]. The software and potential have been used extensively in past simulations similar in nature. For the nanofilms, the geometry used was a rectangular block of dimensions of roughly 25x25x100 nm^3 amounting to approximately 5.5 million atoms. Periodic boundary conditions were applied to the x and y directions and free surfaces were prescribed in the z direction. Because of these boundary conditions, the geometry effectively resembles a nano thin-film, infinite in area but finite in thickness. Thus, we refer to it as a nanofilm and categorize its response as that of bulk single-crystal copper. The geometry of the nanopillars on the other hand is cylindrical and with free surfaces in all directions. In addition, a hemispherical tip is carved at the free surface to better replicate synthesized copper nanopillars [5]. All simulations began with a ramped thermal equilibration scheme using an NPT ensemble, bringing the atoms to 300 K. Once this temperature is achieved, an NVE ensemble is then used and the shock loading is applied. To do this, we designate the first few x-y atomic planes from the left free surface as a rigid piston. To produce the shock loading, atoms belonging to the piston are given a prescribed constant velocity into the material for all time. Typical simulation times were 30-60 picoseconds, with timesteps of 1 femtosecond. Two different crystal orientations were simulated to analyze the effects of orientation. In the first, the loading direction was the [100] direction with x and y being the [010] and [001] directions, respectively. In the second, the loading direction was the [111] with x and y being the $[1\bar{1}0]$ and $[11\bar{2}]$ directions, respectively. After running the simulations, a post-processing program was written to extract information on the profiles of stress, temperature and velocity seen in the simulations. The software Atomeye [102] was used for the atomic visualizations.

6.1 Shock-Loading of Copper Nanofilms

With the crystal oriented with its loading axis along the [100] direction, we observe the nucleation of partial dislocations on the four available 111 slip planes. As the elastic wave propagates through the crystal, the partials simultaneously propagate on the shock front. Due to the periodic boundary conditions, the dislocations are nucleated homogeneously at the shock front. The upper image in Figure 6.1 shows a [100] oriented crystal shocked at 1.2 km/s. Once the compressive shock wave reaches the free surface, it reflects back into the crystal as a tension wave. In all of our cases, we have observed the tensile wave to reverse the plasticity, leaving the crystal in its initial, perfect state. We find the transition from elastic to plastic response occurs between shock impact velocities of 0.8-0.9 km/s, corresponding to loading stresses of ∼35 GPa. While quite large, these values are in agreement with similar previous atomisitic calculations of shocked copper [35],[36]. For the [111] oriented crystals, the (111) plane lies normal to the impact direction and is no longer in play for slip, and the resulting behavior is quite different. Qualitatively, we observe a much more disordered partial dislocation microstructure made up of very short segments with a much higher density of intersections. In addition, we find that the plastic wave no longer travels simulataneously with the elastic wave, but in fact trails it. This phenomenon plays an important role because when the elastic wave reflects back into the crystal, it must penetrate the plastic wave which has yet to reach the surface. This weakening of the plastic wave prevents the reversibility we observed in the [100] cases as the shock wave reflected back into the crystal, and a small percentage of partial dislocations are left unrecovered. On the other hand, the [111] crystals show a greater resilience to impact velocities. Because of lower Schmid factors for partials compared to the [100] crystal (e.g. 0.31427 versus 0.4714), higher stresses, and therefore larger shock impact velocities are required to initiate plasticity in the [111] crystals. We find the transition from elastic to plastic response to occur between shock impact velocities of 1.0-1.1 km/s, corresponding to loading stresses of ∼40-50 GPa.

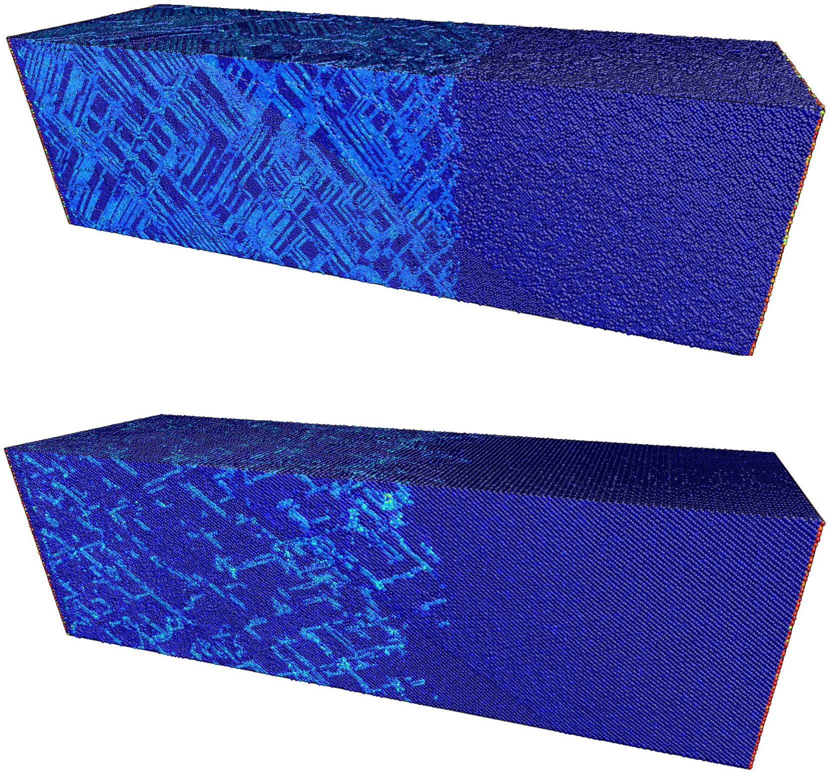

Figure 6.1: Propagation of the shock wave through single-crystal copper samples impacted at the left end by a rigid piston traveling at 1200 m/s. The samples are oriented with loading axes in the [100] (top) and [111] (bottom) orientations. The simulations impose periodic boundary conditions in the directions transverse to loading. Atoms are colored according to their centro-symmetry parameter, with lighter colored atoms representing those belonging primarily to partial dislocation stacking faults, but also to twin boundaries.

6.2 Shock-Loading of Copper Nanopillars

6.2.1 Experimental Observations

In a recent paper, we reported on the fabrication and laser-induced shock-loading of [100]-oriented, single-crystal copper nanopillars, with pillar axes aligned with the wave propagation (compression) direction [5]. An apparatus and related test procedures were developed for the compression of these nanopillars at pressures and strain rates of roughly 1 GPa and 10^7 s^{-1}, respectively, using nanosecond pulse laser-generated stress waves. Figure 6.2 (f) shows the formation of microplatelets growing from the pillar surface; evidence of surface activation due to surface step creation by dislocation-driven processes. As we showed in the previous section, however, impact stresses greater than 35 GPa are required to nucleate and propagate dislocations in bulk nanofilms, much greater than the stresses produced in the laser experiments. Thus, the surface activation seen in the experiments was not to be expected. However, surface phenomena can not be described in the nanofilm simulations due to the periodic boundary conditions. To investigate the reasons for the discrepancy as well as to characterize the response of nano-geometries with free surfaces, we conducted MD simulations with pillar geometries more closely representative of the experimental geometries. The results of these simulations are presented in what follows.

6.2.2 Results of the Simulations

With the availability of free surfaces to play a role in the material response, we find altogether different behavior under shock impact in these simulations. In fact, we find the pillar to undergo two temporal regimes: (1) fully elastic and (2) plastic release. Initially, as the pillar is impacted, an elastic compression wave is generated and begins

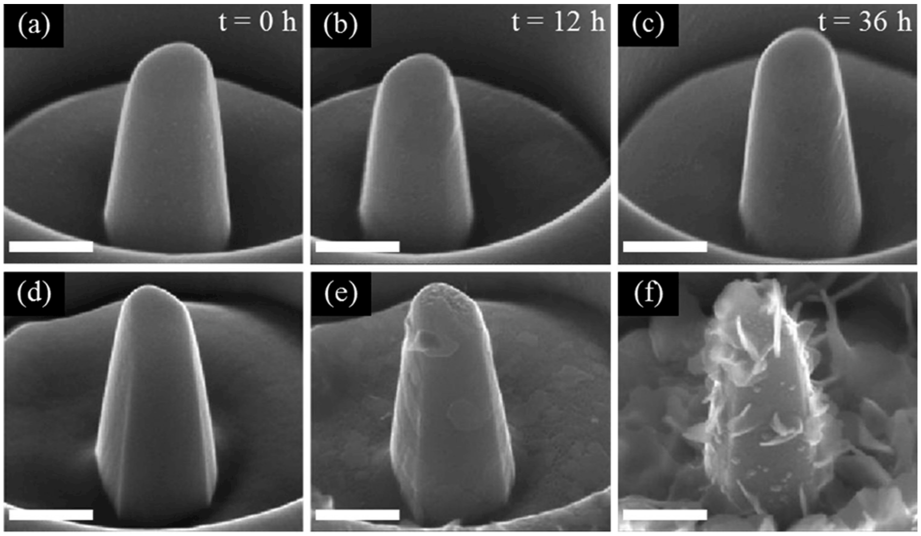

Figure 6.2: SEM images of Cu pillars on a Cu(001) substrate ((a), (d)) prepared via FIB milling prior to testing. ((b), (e)) and ((c), (f)) are obtained 12 and 36 hours after an isopropyl alcohol cleaning, respectively . The images in the top and bottom rows show two different pillars tested at laser fluences of 0 and 39.5 kJ/m^2, respectively. The scale bar in all the images is 400 nm. [5]

its travel through the crystal. Depending on the impact strength, for some period of time we observe full elasticity prior to the nucleation of dislocations. This delay occurs because the free boundaries allow for volume relaxations as a means of impact energy absorption. Thus, in the fully elastic regime we have the elastic wave propagating through the crystal and observe bulging of the pillar near the piston. Once the bulging reaches a maximum for the material the second regime of plastic release begins. This occurs through the generation of dislocations near the piston interface. Unlike the nanofilms, however, we note this nucleation does not occur at the shock front and does not occur homogeneously in the pillar cross-section. With the maximum radial displacements occurring at the surface due to the volumetric bulging, naturally we find the dislocations to nucleate from the surfaces at the piston interface. We also note that when shocked with the same impact velocities as the respective nanofilm cases, the pillars instantaneously melt as the piston passes through the crystal. Thus, the impact velocities and stresses are much lower to generate dislocations in these cases. Specifically, for the [100] oriented pillar we have found that reducing the impact velocity to ∼0.1 km/s, the nucleation of dislocations just occurs. This corresponds to an axial stress of ∼1.0-1.5 GPa, on the order of the stresses produced in the experiments. Figure 6.3 shows the results of the impact of an 80 nm diameter copper nanopillar with [100] orientation by a rigid piston traveling at 250 m/s (∼5 GPa). The top three images show the dislocation nucleation and evolution phases as the shock wave proceeds, and the last image shows the resulting surface damage. We note in these images the dominance of partial dislocations with stacking faults of very large surface area. As the partials travel on the four active 111 planes, they meet creating a pyramid shape. Slip continues to occur until the partials reach the surface, leaving damage at the free surfaces in the form of surface steps. Experimentally, such regions of surface damage can act as effective zones for the production of oxides when exposed to various chemicals and atmospheres. For the [111] oriented crystals, the nucleation of dislocations occurs in a much more scattered way compared to the [100] pillars. At the piston interface and in a statistically symmetric way around the circumference of the pillar, very short dislocation segments are nucleated. Figure 6.4 shows the results of the impact of an 80 nm diameter copper nanopillar with [111] orientation along its axis by a rigid piston traveling at 300 m/s. The top three images show the dislocation nucleation and evolution phases as the shock wave proceeds, and the last image shows the resulting surface damage. We note the decreased presence of highly ordered and planar stacking faults as compared to the [111] orientation, in favor of a tangled network of very short perfect and partial dislocations. We

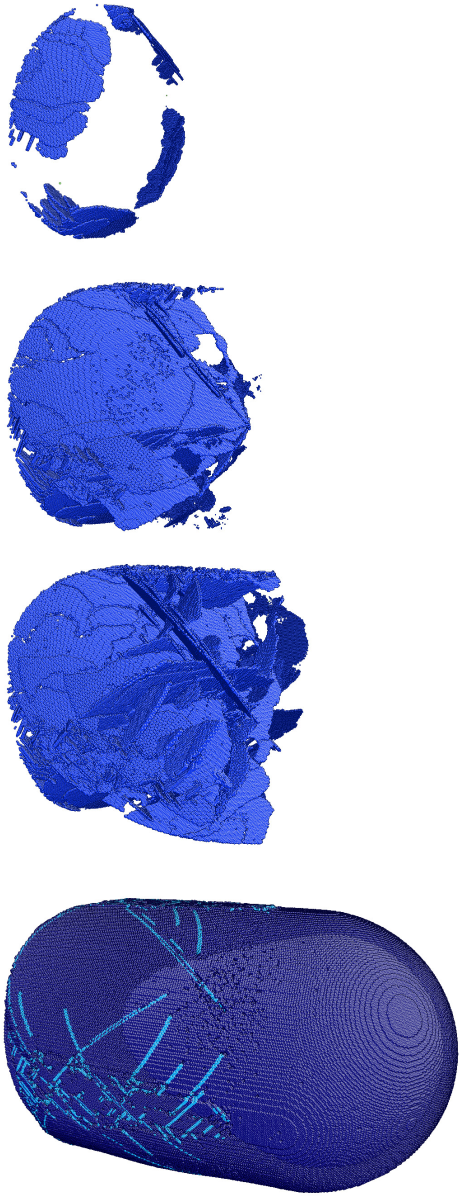

Figure 6.3: Impact of an 80 nm diameter copper nanopillar with [100] orientation along its axis by a rigid piston traveling at 250 m/s (∼5 GPa). The top three images show the dislocation nucleation and evolution phases as the shock wave proceeds, and the last image shows the resulting surface damage. We note the nucleation of dislocations is not homogeneous, but occurs at the free surfaces and at much lower stresses, as compared the simulations of the bulk nanofilms.

find again that the [111] orientation is more resilient to shock due to Schmid factor considerations, and also that the resulting surface damage is less pronounced than the [100] cases. Thus, we have shown here the importance of size in the material response to shock loading. In bulk materials with very low surface to volume ratios, such as the nanofilms, shock stresses greater than 35 GPa must be reached to induce plasticity. In nanostructures with large surface to volume ratios, such as the nanopillars, much lower impact stresses are capable of generating dislocations and lead to permanent surface damage in materials.

6.3 Shock-Induced Void Nucleation and Spallation in Bulk Nanofilms

6.3.1 Description of the Simulations

In these simulations, the nanofilm geometry with periodicity transverse to loading was used. The film was split into two regions separated by an imaginary impact plane roughly one-third the length from the left free surface. Following the thermal equilibration phase, the z component of the velocities of all atoms in the region to the left of the impact plane were given an initial value of $2/3v$, while all atoms in the region to its right were given initial z velocity components of -$1/3v$, where v is the desired impact velocity. Figure 6.5 describes the four subsequent stages leading to spallation following impact. Upon impact, two compression waves travel away from the impact plane. Next a tension wave is reflected back into the crystal at the left surface and also at the right surface. When the two tension waves meet, the material is pulled in opposite directions at the spall plane. The method is designed to minimize rigid body translation of the nanofilm and provide a spall plane at z=$2/3L$, and has been used with success in the past [103] for simulations in aluminum.

6.3.2 Results of the Simulations

Our results show stark differences between nanofilms oriented in the [100] direction versus the [111] direction. Specifically, the [100] nanofilms are found to be significantly more resilient to spall than their counterparts. This seems counter-intuitive, since we previously established that shocked nanofilms with [111] orientations require significantly larger stresses to initiate plasticity, and would therefore be viewed as stronger. However, in these results we find that the relative ease with which [100] nanofilms can reduce stresses by slip is their main advantage in countering spallation as compared to the [111] nanofilms.

For the [100] pillars, the transition from elastic to plastic response occurs at a relative impact velocity of approximately 1.0 km/s. For the [111] pillars, this transition occurs at approximately 0.8 km/s. At this transition, the initial compression and reflected tension waves are fully elastic. However, when the tension waves meet at the spall plane and pass through each other, a large number of intersecting stacking faults are generated. Once the available slip systems have been exhausted, the continued tension causes a small number of voids to form at stacking fault intersections. These intersections represent weak areas the material. Near the elastic-plastic transition, the voids are found to reach a critical size before the compression waves return to squeeze the material back together, leaving a few permanent voids in the material. At larger impact velocities, however, a transition to full spallation occurs. In figure 6.6 we show the impact of a [100] nanofilm with relative impact velocity 1.8 km/s. The top image shows the initial impact stage. Here, the impact is large enough to generate a plastic wave. Once the tensile fronts of plastic waves meet at the spall plane, the homogeneous nucleation of voids is seen to occur in the center image. The continued growth of these voids can be seen in the bottom image. When the void concentrations and radii are large enough, void coalescence occurs and the material will separate.

In figure 6.7, we show the impact of a [111] nanofilm with relative impact velocity 0.9 km/s. One difference we find for the [111] nanofilms is that even under extremely high impact velocities, the initial compression and tension waves remain elastic, though even under extremely high stresses. As we showed under normal shock compression in section 6.1, [111] geometries produce high densities of small intersecting dislocation segments. This behavior leads to a higher concentration of small voids to form at the small plane and for the material to separate in a much more planar way as seen in the figure.

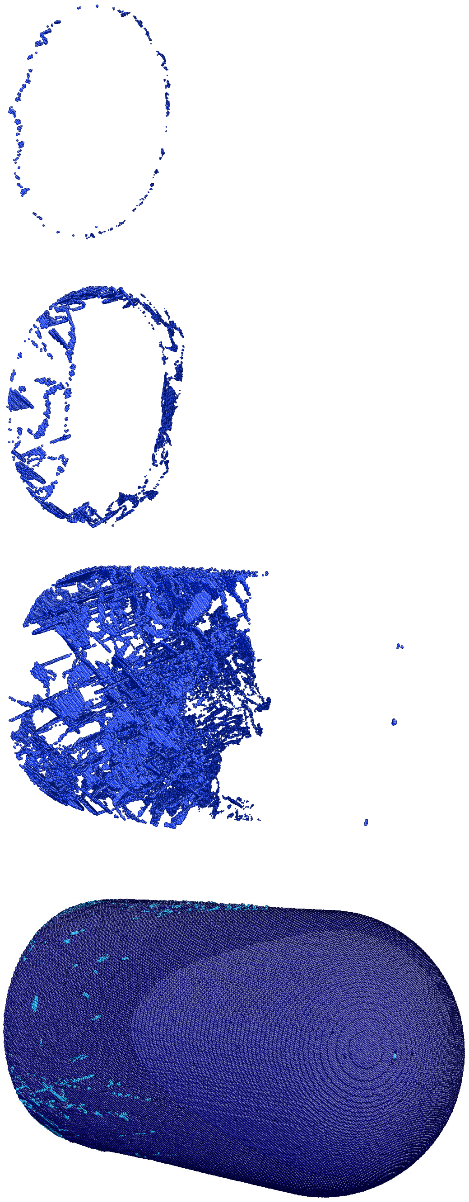

Figure 6.4: Impact of an 80 nm diameter copper nanopillar with [111] orientation along its axis by a rigid piston traveling at 300 m/s. The top three images show the dislocation nucleation and evolution phases as the shock wave proceeds, and the last image shows the resulting surface damage. We note the decreased presence of highly ordered and planar stacking faults as compared to the [111] orientation, in favor of a tangled network of very short perfect and partial dislocations.

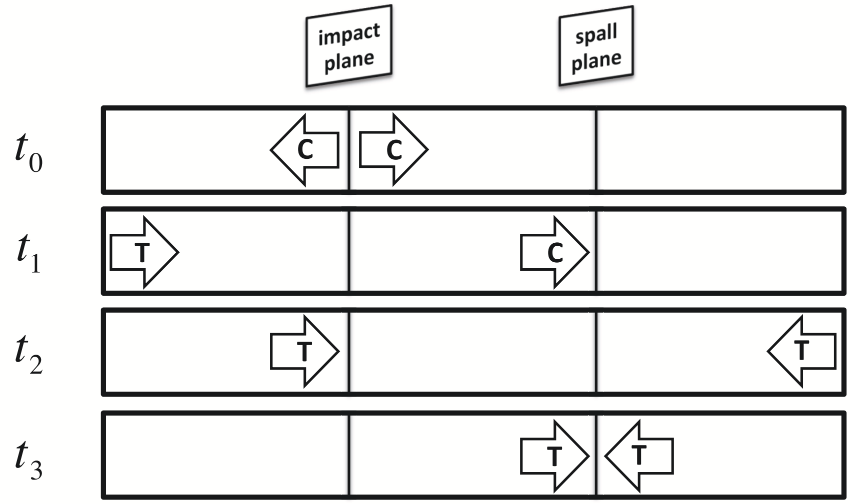

Figure 6.5: Four stages of compression (C) and tension (T) wave propagation leading to spallation. (t_0) Following impact, two compression waves travel away from the impact plane; (t_1) a tension wave is reflected back into the crystal at the left surface; (t_2) a tension wave is reflected back into the crystal at the right surface; (t_3) the two tension waves meet, initiating spallation at the spall plane

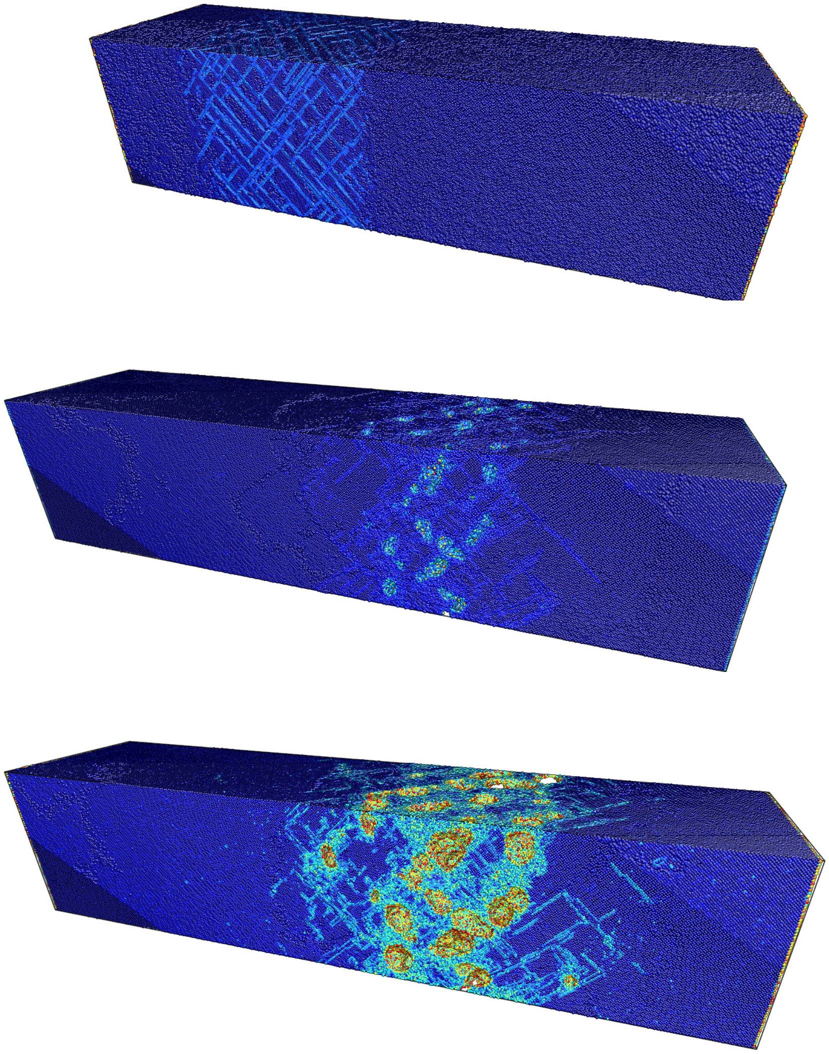

Figure 6.6: Void nucleation and growth in a [100] oriented copper nanofilm with relative impact velocity of 1800 km/s at three different times. Just after impact, two plastic wave fronts move away from the impact plane (top). When the two tensile wave fronts meet, small voids are homogeneously nucleated at the intersections of stacking faults (middle), and subsequent void growth occurs (bottom). This [100] orientation has been found to be more stable against spallation than the [111].

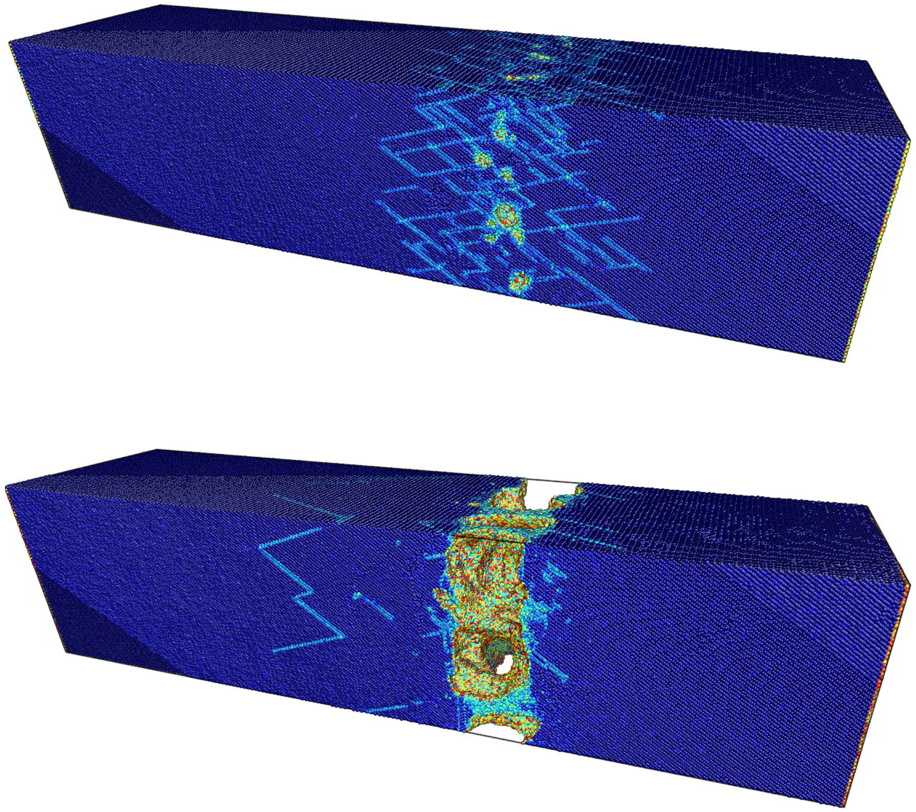

Figure 6.7: Void nucleation and spallation in a [111] oriented copper nanofilm with relative impact velocity of 900 km/s at two different times.

Chapter 7

Conclusions

In this dissertation, major advances were made in the modeling of materials in extreme environments. In the second chapter, a hybrid method was developed coupling the results of molecular statics calculations with classical isotropic elasticity theory to extract a continuum representation of various point defects through the use of elastic force-multipoles. The calculations provided a means to account for the changes in defect energetics due to local strain environment effects. For the force-multipole representation of defects, we emphasized the use of higher-order multipole tensors to even more accurately represent the predicted lattice response of many defects from the atomistic calculations. These include interstitial and substitutional defects, which have been typically only modeled with the dipole moment. In these cases we found specific importance of the octopole moment ($P^{(3)}$), in enhancing the complexity of the lattice response to match the MS calculations, and overcome the dipole moment's predicted $1/r$ monotonic decay near the defect core. This was illustrated in detail for the case of substitutional He. While in most cases atomistic calculations of defect displacements show anisotropies and discrete lattice phenomena, we find the isotropic elastic Green's function to provide very accurate material response, provided higher-order moments describing the defect are implemented.

In the third chapter, a method was developed to calculate dislocation bias factors in several bcc and fcc metals using a finite-element rate-theory technique. Using the developed method for the elastic representation of point defects, a more rigorous formulation of the interaction energy was used to describe the anisotropic diffusion in the vicinity of the dislocation than previous studies. First using isotropic elasticity theory, the bias factors were compared directly to numerically and analytically obtained values from previous studies and the discrepancies elucidated. The dependence of the bias factors on damage dose rate, dislocation density, and temperature were each examined. We found very strong dependence on temperature and dislocation density for all of the materials considered. Increasing the temperature was confirmed to lead to lower bias factors while increasing dislocation density increased the bias. Under typical conditions, very good agreement was found with several studies for fcc copper and nickel.

Next, a systematic examination of the effects of anisotropy, SIA orientation and migration mechanisms on dislocation bias calculations was undertaken. Our findings can be summarized as follows:

1. In iron, dipole tensors obtained using anisotropic elasticity decreased the bias by 45% compared to those obtained using the isotropic formulation. In copper, the opposite effect is seen and the bias is increased by ∼6-9%.

2. Anisotropic dislocation strain fields give larger interaction energy gradients, leading to increased drift diffusion and larger bias (12% and 6% increase in Fe and Cu, respectively).

3. Effects of preferred SIA orientations should not be ignored near the dislocation core. Implementing minimum energy SIA configurations in iron decreases repulsive interactions and increases absorption, ultimately leading to much larger bias factors.

4. One-dimensional migration in iron plays a significant role in decreasing the bias,

but its effect is greatly diminished when anisotropy and SIA orientations are accounted for.

From this study, it was concluded that the discrepancy between past theoretical studies and empirically obtained dislocation bias factors is not due only to the absence of anisotropy and preferred SIA orientations in the former. To achieve bias factors closer to the empirical values, the most important mechanisms by which the migrating SIA population is decreased must be identified. A closer examination, for example, at the formation and growth of sessile SIA clusters should be undertaken and implemented in future models.

In the fourth chapter, a spatially-resolved rate theory approach was developed to simulate the evolution of average sized helium-vacancy bubbles near the surface of an irradiated tungsten component under the associated stress and temperature gradients. The problem of bubble migration in stress and temperature gradients has been explored by many authors, with the common conclusion that temperature gradients have a much larger effect on driving bubbles themselves. While this remains true, we have found that near surfaces, point defect drift is driven more strongly by stress gradients, leading to larger bubble sizes near the surface, in agreement with experiments. The effects of stress gradients, however, become negligible for even very short distances away from the surface, in agreement with the literature.

In the fifth chapter, a novel approach was developed to describe the full size distribution of bubbles in helium-vacancy phase space and time. Due to fluctuations in point defect absorption rates with bubbles, because of the stochastic nature of the irradiation environment itself (collision cascades, Brownian diffusion, etc.), it becomes necessary to account for the spreading of the helium-vacancy cluster size distribution beyond its estimated average. Thus, we developed a method based on a stochastic differential equations formulation and a reconstruction of the distribution by its first and second moments. The approach requires the use of Ito's rule for the derivation of the moment differential equations of the (in bubble) helium and vacancy concentrations. A numerical procedure was outlined, detailing the derivations and implementation of the method. Results showed the immediate spreading of distribution, more pronounced in the vacancy direction, in the first few seconds of exposure. This was followed by a stable period where the dimensions of the distribution surface (second moments) remained approximately constant as the mean moved through the He-V phase space. After some time, when the mean bubble sizes are larger, the width of the distribution in the vacancy direction begins to shrink. This is due to the decreased effect of point defect fluctuations on bubbles of larger size. For this reason, an extension of this work should include the contributions of bubble coalescence in the white noise terms. The developed method is very general, and can be extended to a description of the size distribution as a function of space and time in any irradiated material. The large degree of parameterization allows for excellent flexibility and increased accuracy, particularly when experimental data is available.

In the last chapter, extensive non-equilibrium molecular dynamics simulations were performed on copper nanostructures under shock loading. These simulations provided insight into the collective atomic mechanisms that govern material deformation at high strain rates. The study was motivated by recent experimental evidence showing surface damage in nanopillars shocked with stresses known to be considerably smaller than those required to induce plasticity in bulk materials. Thus we performed simulations on both nanofilms, which represent the response of the bulk samples, and also of nanopillars, representative of the experimental geometries. In nanofilms, we found the presence of periodic boundary conditions require much larger impact stresses to induce plasticity (> 35 GPa) compared to nanopillars, where free surfaces play an important role. In nanopillars, comparison to the experiments explained the observed surface activation at lower than expected stresses (~ 1 GPa), due to dislocation nucleation and termination at the free surfaces. Additional simulations of spallation were also performed. Results showed the formation of voids occurrs at the intersections of stacking faults at the spall plane. The growth and coalescence of these voids leads to the full spallation of the material. In these cases the [100] oriented crystals showed increased resilience to spallation compared to the [111] crystals.

Bibliography

[1] L. K. Mansur. Theory and experimental background on dimensional changes in irradiated alloys. *J. Nuc. Mat.*, 216:97–123, 1994. xi, 2, 3, 5, 11

[2] B. N. Singh, A. J. E. Foreman, and H. Trinkaus. Radiation hardening revisited: role of intracascade clustering. *J. Nuc. Mat.*, 249:103–115, 1997. xi, 3, 4, 11

[3] L.L. Hsiung. Shock-induced phase transformation in tantalum. *J. Phys.: Condens. Matter*, 22:385702, 2010. xi, 10

[4] H. Greuner, H. Maier, M. Balden, B. Boeswirth, and Ch. Linsmeier. Investigation of w components exposed to high thermal and high h/he fluxes. *J. Nucl. Mater.*, 417:495–498, 2011. xii, 59

[5] G. Youssef, R. Crum, S. V. Prikhodko, D. Seif, G. Po, N. Ghoniem, S. Kodambaka, and V. Gupta. The influence of laser-induced nanosecond rise-time stress waves on the microstructure and surface chemical activity of single crystal cu nanopillars. *J. Appl. Phys.*, 113(8):084309, 2013. xiii, 9, 93, 96, 97

[6] C.C. Fu and F. Willaime. First principles calculations in iron: structure and mobility of defect clusters and defect complexes for kinetic modelling. *C.R. Physique*, 9:335–342, 2008. 7, 43, 44, 50

[7] M. J. Caturla, C. J. Ortiz, and C. C. Fu. Helium and point defect accumulation: (ii) kinetic modelling. *C. R. Physique*, 9:401–408, 2008. 7, 25, 27

[8] C.C. Fu and F. Willaime. Ab initio study of helium in alpha-iron: Dissolution, migration and clustering with vacancies. *Phys. Rev. B*, 72(064117), 2005. 7

[9] P.M. Derlet, D. Nguyen-Manh, and S.L. Dudarev. Multiscale modeling of crowdion and vacancy defects in body-centered-cubic transition metals. *Phys. Rev B*, 76(054107), 2007. 7

[10] C.S. Becquart and C. Domain. *Nuc. Instr. and Meth. in Phys. Res. B*, 255:23–26, 2007. 7

[11] L. Yang, H. Liu, and X. Zu. First-principles study of the migration of helium in tungsten. *Intl. J. of Mod. Phys. B*, 23(8), 2009. 7

[12] M.J. Caturla, N. Soneda, E. Alonso, B.D. Wirth, T.D. de la Rubia, and J.M. Perlado. Comparative study of radiation damage accumulation in copper and iron. *J. of Nuc. Mat.*, 276:13–21, 2000. 7, 8

[13] R.W. Balluffi. Vacancy defect mobilities and binding energies obtained from annealing studies. *J. of Nuc. Mat.*, 69-70:240–263, 1978. 7, 8

[14] G.J. Ackland, M.I. Mendelev, D.J. Srolovitz, S. Han, and A.V. Barashev. Development of an interatomic potential for phosphorus impurities in alpha-iron. *J. Phys.: Condens. Matter*, 15:S2629–S2642, 2004. 7

[15] S.P. Mhaskar and P.K. Naik. Helium desorption from a tungsten single crystal. *Phys. Stat. Sol. (b)*, 14:84–90, 1981. 7

[16] R.A. Johnson. Point-defect calculations for tungsten. *Phys. Rev. B*, 27(4), 1983. 7

[17] Z. Z. Chen, N. Kioussis, N. M. Ghoniem, and D. Seif. Strain-field effects on the formation and migration energies of self interstitials in α-iron from first principles. *Phys. Rev. B*, 81(094102), 2010. 7, 22, 24

[18] H. Schultz. *in: Atomic Defects in Metals*. Landolt-Bornstein, 1991. 7

[19] J. Marian, B.D. Wirth, A. Caro, B. Sadigh, G.R. Odette, J. M. Perlado, and T. Diaz de la Rubia. Dynamics of self-interstitial cluster migration in pure iron and iron-copper alloys. *Phys. Rev. B*, 65:144102, 2002. 7

[20] T. Seletskaia, Y. Osetsky, R.E. Stoller, and G.M. Stocks. Magnetic interactions influence the properties of helium defects in iron. *Phys. Rev. Lett.*, 94, 2005. 7

[21] S.M. Foiles, M.I. Baskes, and M.S. Daw. Embedded-atom-method functions for the fcc metals Cu, Ag, Au, Ni, Pd, Pt, and their alloys. *Phys. Rev. B*, 33(12):7983–7991, 1986. 8

[22] J.B. Adams and W.G. Wolfer. Formation energies of helium-void complexes in nickel. *J. of Nuc. Mat.*, 166:235–242, 1989. 8

[23] W. Wycisk and M. Feller Kniepmeier. Quenching experiments in high purity Ni. *J. of Nuc. Mat.*, 69-70:616, 1978. 8

[24] Y. Mishin, D. Farkas, M.J. Mehl, and D.A. Papaconstantopoulos. Interatomic potentials for aluminum and nickel from experimental data and ab initio calculations. *Mult. Mod.of Mat. Symposium*, pages 535–540, 1999. 8, 44

[25] G. Dublek et al. *J. Appl. Phys.*, 13:67–70, 1977. 8

[26] E.H. Megchiche, C. Mijoule, and M. Amarouche. First principles calculations of vacancy-vacancy interactions in nickel: thermal expansion effects. *J. Phys.: Condens. Matter*, 22:485502, 2010. 8

[27] P. Zhao and Y. Shimomura. Molecular dynamics calculations of properties of the self-interstitials in copper and nickel. *Comp. Mat. Sci.*, 14:84–90, 1999. 8

[28] K. Morishita, T. Diaz de la Rubia, E. Alonso, N. Sekimura, and N. Yosida. A molecular dynamics simulation study of small cluster formation and migration in metals. *J. of Nuc. Mat.*, 283-287:753–757, 2000. 8

[29] W.D. Wilson, M.I. Baskes, and C.L. Bisson. Atomistics of helium bubble formation in a face-centered-cubic metal. *Phys. Rev. B*, 13(6), 1976. 8

[30] J. Yang, B. Ao, W. Hu, and X. Wang. The formation energies and binding energies of helium vacancy cluster: comparative study in Ni and Pd. *J. of Phys.: Conf. Series*, 29:190–193, 2006. 8

[31] J. Kuhalainan. *J. Phys.: Condens. Matt.*, 8:10317, 1996. 8

[32] R.E. Stoller, A.S. Kumar, and D.S. Gelles. *Eff. of Rad. on Mat.:15th Int'l Symp.* 1992. 8

[33] V. Phillips, K. Sonnenberg, and J.M. Williams. Diffusion of helium in nickel. *J. of Nuc. Mat*, 107:271–279, 1982. 8

[34] X.T. Zu, L. Yang, F. Gao, S.M. Peng, H.L. Heinisch, X.G. Long, and R.J. Kurtz. Properties of helium defects in BCC and FCC metals investigated with density functional theory. *Phys. Rev. B*, 80:054104, 2009. 8

[35] E.M. Bringa, A. Caro, Y.M. Wang, M. Victoria, J.M. McNaney, B.A. Remington, R.F. Smith, B.R. Torralva, and H. van Swygenhoven. Ultrahigh strength in nanocrystalline materials under shock loading. *Science*, 309(5742):1838–1841, January 2005. 8, 9, 94

[36] B.L. Holian and P.S. Lomdahl. Plasticity Induced by Shock Waves in Nonequilibrium Molecular-Dynamics Simulations. *Science*, 280(5372):2085–2088, June 1998. 9, 94

[37] M. Bringa, K. Rosolankova, R.E. Rudd, B.A. Remington, J.S. Wark, M. Duchaineau, H. Kalantar, J. Hawreliak, and J. Belak. Shock deformation of face-centred-cubic metals on subnanosecond timescales. *Nature Materials*, 5(10):805–809, January 2006. 9

[38] B.A. Remington, P. Allen, E.M. Bringa, J. Hawreliak, D. Ho, K.T. Lorenz, H. Lorenzana, J.M. McNaney, M.A. Meyers, S.W. Pollaine, K. Rosolankova, B. Sadik, M.S. Schneider, D. Swift, J. Wark, and B. Yaakobi. Material dynamics under extreme conditions of pressure and strain rate. *Mat. Sci. And Tech.*, 22(4):474–488, January 2006. 9

[39] E.M. Bringa, B.D. Wirth, M.J. Caturla, J. Stolken, and D. Kalantar. Metals far from equilibrium: From shocks to radiation damage. *Nuc. Instr.and Meth. In Phys. Res. B-Beam Inter. With Mat. And Atoms*, 202:56–63, April 2003. 9

[40] L.P. Davila, P. Erhart, E.M. Bringa, M.A. Meyers, V.A. Lubarda, M.S. Schneider, R. Becker, and M. Kumar. Atomistic modeling of shock-induced void collapse in copper. *App. Phys. Lett.*, 86(16):161902, January 2005. 9

[41] E.M. Bringa, A. Caro, M. Victoria, and N. Park. The atomistic modeling of wave propagation in nanocrystals. *Jom*, 57(9):67–70, January 2005. 9

[42] E.M. Bringa, J.U. Cazamias, P. Erhart, J. Stolken, N. Tanushev, B.D. Wirth, R.E. Rudd, and M.J. Caturla. Atomistic shock Hugoniot simulation of single-crystal copper. *J. Appl. Phys.*, 96(7):3793–3799, January 2004. 9

[43] C. Domain, C. S. Becquart, and L. Malerba. Simulation of radiation damage in iron alloys: an object kinetic monte carlo approach. *J. Nuc. Mat.*, 335:121–145, 2004. 11

[44] K. Morishita and R. Sugano. Modeling of he-bubble migration in bcc iron. *Nuc. Inst. and Meth. in Phys. Re. B*, 255:52–56, 2007. 11

[45] B. D. Wirth and E. M. Bringa. A kinetic monte carlo model for helium diffusion and clustering in fusion environments. *Phys. Scr.*, T108:80–84, 2004. 11

[46] J. S. Koehler. Diffusion of lattice defects in a stress field. *Phys. Rev.*, 181(3):1015–1019, 1969. 11

[47] P. H. Dederichs and K. Schroeder. Anisotropic diffusion in stress fields. *Phys. Rev. B*, 17:2524, 1978. 12

[48] J. D. Eshelby. Distortion of a crystal by point imperfections. *J. Appl. Phys.*, 25:255, 1954. 14

[49] H. Kanzaki. Point defects in face-centred cubic lattice-i distortion around defects. *J. Phys. and Chem. Sol.*, 2:24–36, 1957. 15

[50] R. Bullough and J. Hardy. The strain field interaction between vacancies in copper and aluminum. *Phil. Mag.*, 17:833, 1968. 15

[51] C. S. Hartley and R. Bullough. On the description of crystal defects by point-force arrays. *J. Appl. Phys.*, 48:4557–4564, 1977. 15

[52] R. Siems. Mechanical interactions of point defects. *Phys. Stat. Sol.*, 80:645, 1968. 15

[53] C. Teodosiu. *Elastic Models of Crystal Defects*. Springer-Verlag, New York, 1982. 15

[54] K. Garikipati, M. Falk, M. Bouville, B. Puchala, and H. Narayanan. The continuum elastic and atomistic viewpoints on the formation volume and strain energy of a point defect. *J. Mech. and Phys. Sol.*, 54:1929, 2006. 17

[55] A.B. Sivak, V.A. Romanov, and V.M. Chernov. Influence of stress fields of dislocations on formation and spatial stability of point defects (elastic dipoles) in vanadium and iron crystals. *J. Nuc. Mat.*, 323:380–387, 2003. 17, 23

[56] X. Zhang, K. Jiao, P. Sharma, and B. I. Yakobson. An atomistic and non-classical continuum field theoretic perspective of elastic interactions between defects (force dipoles) of various symmetries and application to graphene. *J. Mec. and Phys. Sol.*, 54:2304–2329, 2006. 18

[57] M.J. Aziz. Thermodynamics of diffusion under pressure and stress: Relation to point defect mechanisms. *App. Phys. Lett.*, 70(21):2810, 1997. 18

[58] G. J. Ackland, M. I. Mendelev, D. J. Srolovitz, S. Han, and A. V. Barashev. Development of an interatomic potential for phosphorus impurities in α-iron. *J. Phys.: Condens. Matter*, 16:2629–2642, 2004. 20

[59] N. Juslin and K. Nordlund. Pair potential for iron-helium. *J. Nuc. Mat.*, 382:143–146, 2008. 20

[60] J. E. Lennard-Jones. On the determination of molecular fields. ii. from the equation of state of a gas. *Proc. Royal Soc. London A*, 106:463, 1924. 20

[61] P. Ehrhart, K. H. Robrock, and H. R. Schober. *Physics of Radiation Effects in Crystals*. Elsevier, Amsterdam, 1986. 22

[62] C. Domain and C. S. Becquart. Ab-initio calculations of defects in iron and dilute iron-copper alloys. *Phys. Rev. B*, 65(024103), 2002. 22

[63] C. C. Fu, F. Willaime, and P. Ordejón. Stability and mobility of mono- and di-interstitials in alpha-iron. *Phys. Rev. Lett.*, 92(175503), 2004. 22

[64] D. A. Terentyev, L. Malerba, and M. Hou. Dimensionality of interstitial cluster motion in bcc-iron. *Phys. Rev. B*, 75(104108), 2007. 22

[65] B. J. Lee and M. I. Baskes. Second nearest-neighbor modified embedded-atom-method potential. *Phys. Rev. B*, 62:8564, 2000. 24

[66] C. C. Fu and F. Willaime. Ab initio study of helium in α-iron: Dissolution, migration, and clustering with vacancies. *Phys. Rev. B*, 72(064117), 2005. 26

[67] K. Morishita, R. Sugano, B. D. Wirth, and T. Diaz de la Rubia. Thermal stability of heliumvacancy clusters in iron. *Nuc. Instr. and Meth. in Phys. Res. B*, 202:76–81, 2003. 27

[68] J.P. Hirth and J. Lothe. *Theory of Dislocations*. John Wiley & Sons, 2 edition, 1982. 29, 43

[69] C.C. Cawthorne and E.J. Fulton. Voids in irradiated stainless steel. *Nature*, 216:575, 1967. 35, 61

[70] F.S. Ham. Stress-assisted precipitation on dislocations. *J. of Appl. Phys.*, 30(6), 1959. 36, 45

[71] W.G. Wolfer. The dislocation bias. *J. Comp.-Aid Mat. Des.*, 14:403–417, 2007. 36, 43, 45, 47, 54

[72] W.G. Wolfer and M. Ashkin. Diffusion of vacancies and interstitials to edge dislocations. *J. of Appl. Phys.*, 47(3), 1976. 36

[73] C.H. Woo and B.N. Singh. Production bias due to clustering of point defects in irradiation-induced cascades. *Phil. Mag. A*, 65:889–912, 1992. 36

[74] P.H. Dederichs and K. Schroeder. Anisotropic diffusion in stress fields. *Phys. Rev. B*, 17:2524, 1978. 39

[75] B.C. Skinner and C.H. Woo. Shape effect in the drift diffusion of point defects into straight dislocations. *Phys. Rev. B*, 30(6), 1984. 39, 47, 48

[76] W.A. Coghlan. *in: Proc. of the Comp. Sim. for Mat. Appl.*, page 166, 1976. 39

[77] D. Seif and N.M. Ghoniem. Dislocation bias calculations in metals using a combined finite-element rate-theory approach. *Effects of Radiation on Nuclear Materials on June 15, 2011 in Anaheim, CA*, STP 1547:1–12, 2012. 42

[78] N.M. Ghoniem and D.D. Walgraef. *Instabilities and Self-Organization in Materials, Volume I*, Oxford University Press, 2008. 42, 50

[79] G.J. Ackland, M.I. Mendelev, D.J. Srolovitz, S. Han, and A.V. Barashev. Development of an interatomic potential for phosphorus impurities in alpha-iron. *J. Phys.: Condens. Matter*, 15:S2629–S2642, 2004. 42

[80] Y. Mishin, M.J. Mehl, D.A. Papaconstantopoulos, A.F. Voter, and J.D. Kress. Structural stability and lattice defects in copper: Ab initio, tight-binding, and embedded-atom calculations. *Phys. Rev. B*, 63:224106, 2001. 42, 92

[81] K. Morishita, T.D. de la Rubia, and E. Alonso. A molecular dynamics simulation study of small cluster formation and migration in metals. *J. of Nuc. Mat.*, 283-287:753–757, 2000. 43, 44

[82] R.W. Balluffi. Vacancy defect mobilities and binding-energies obtained from annealing studies. *J. of Nuc. Mat.*, 69-70:240–263, 1978. 43, 44

[83] H.R. Schober. Polarizabilities of point defects in metals. *J. of Nuc. Mat.*, 126:220–225, 1984. 43

[84] P. Zhao and Y. Shimomura. Molecular dynamics calculations of properties of the self-interstitials in copper and nickel. *Comp. Mat. Sci.*, 14:84–90, 1999. 44

[85] S.L. Dudarev. The non-arrhenius migration of interstitial defects in bcc transition metals. *UKAEA Fusion Report*, 545, 2007. 44

[86] P.M. Derlet, D. Nguyen-Manh, and S.L. Dudarev. Multiscale modeling of crowdion and vacancy defects in body-centered-cubic transition metals. *Phys. Rev B*, 76(5), 2007. 44

[87] K.M. Miller. Dislocation bias and point-defect relaxation volumes. *J. of Nuc. Mat.*, 84:167–172, 1979. 47

[88] A.B. Sivak, V.M. Chernov, N.A. Dubasova, and V.A. Romanov. Anisotropy migration of self-point defects in dislocation stress fields in bcc iron and fcc copper. *J. of Nuc. Mat.*, 367-370:316–321, 2007. 48

[89] Yu. N. Osetsky, D.J. Bacon, A. Serra, B.N. Singh, and S.I. Golubov. One-dimensional atomic transport by clusters of self-interstitial atoms in iron and copper. *Phil. Mag.*, 83(1):61–91, 2003. 52

[90] H. Kamiyama, H Rafii-Tabar, Y. Kawazoe, and H. Matsui. An md simulation of interactions between self-interstitial atoms an edge dislocation in bcc transition metals. *J. of Nuc. Mat.*, 212-215:231, 1994. 52

[91] R. Becker and W. Doring. Kinetische behandlung der keimbildung in ubersattigten dampfern. *Annalen der Physik*, 24:719–752, 1935. 59

[92] J.L. Katz and H. Wiedersich. Nucleation of Voids in Materials Supersaturated with Vacancies and Interstitials. *J. Chem. Phys.*, 55(3):1414–1425, 1971. 61

[93] K.C. Russell. Nucleation of Voids in Irradiated Metals. *Acta Met.*, 19(8):753–758, 1971. 61

[94] J.L. Katz and H. Wiedersich. Effect of Insoluble Gas Molecules on Nucleation of Voids in Materials Supersaturated with Both Vacancies and Interstitials. *J. Nuc. Mat.*, 46(1):41–45, 1973. 64

[95] K.C. Russell. Thermodynamics of Gas-Containing Voids in Metals. *Acta Met.*, 20(7):899–907, 1972. 64

[96] N.M. Ghoniem, J.N. Alhajji, and D. Kaletta. The effect of helium clustering on its transport to grain boundaries. *J. Nuc. Mat.*, 136:192–206, 1985. 67

[97] F.A. Nichols. Kinetics of diffusional motion of pores in solids: A review. *J. Nucl. Mater.*, 30:143, 1969. 71

[98] J.D. Eshelby. The force on an elastic singularity. *Phil. Trans. Roy. Soc. (London)*, 244:87, 1951. 71

[99] J.S. Yu, G.Q. Cai, and Y.K. Lin. A new path integration procedure based on gauss-legendre scheme. *Int. J. Non-Linear Mechanics*, 32:759–768, 1997. 79

[100] K. Ito. Stochastic integral. *Proc. Imp. Acad.*, 20:519–524, 1944. 81

[101] Steve Plimpton. Fast parallel algorithms for short-range molecular dynamics. *J. Comp. Phys.*, 117:1–19, 1995. 92

[102] J. Li. Atomeye: an efficient atomistic configuration viewer. *Modelling Simul. Mater. Sci. Eng.*, 11:173–177, 2003. 93

[103] S.G. Srinivasan, M.I. Baskes, and G.J. Wagner. Atomistic simulations of shock induced microstructural evolution and spallation in single crystal nickel. *J. App. Phys.*, 101(4):043504, February 2007. 101